

**Queen Mary University of London**  
**School of Engineering and Material Science**

---

Technical Report

**Design and Manufacture of  
an I-Class Rocket**

180002076	Ardrit Ramadani
190078274	Ruben Pena Lopes
200182197	Paula M. Fernandez Garrigues

Supervisors: Fariborz Motallebi & Sergey Karabasov

---

**MAT7400 – Research and Design Team project**

April 2024

## DECLARATION

### *Design and Manufacture of an I-Class Rocket*

was composed by *Ardrit Ramadani, Ruben Pena Lopes* and *Paula Maxima Fernandez Garrigues*, and is based on our own work. Where the work of the others has been used, it is fully acknowledged in the text and in captions to table illustrations. This report has not been submitted for any other qualification.

**Name:** Ardrit Ramadani, Ruben Pena Lopes and Paula Maxima Fernandez Garrigues

**Signed:**



**Date:** 25th April 2024

## **Acknowledgements**

We would like to express our gratitude to our supervisors Fariborz Motallebi and Sergey Karabasov, for their invaluable guidance and expert advice throughout this project. Their feedback and encouragement helped in shaping our research and ensuring its completion.

We would also like to extend our most sincere gratitude to Brandon Paice, Queen Mary's skilled technician whose expertise and love of the art were essential to the manufacturing of the rocket's components including: the aluminium low-speed nose cone and smaller scaled high-speed nose cone, as well as the manufacturing and assembling of the two different fin configurations used in all experimental testing described on this report. Brandon's craftsmanship and attention to detail was crucial for the execution of the experimental tests and therefore, to the completion of this report. Aswell as Dr Hussain Ali Abid for extensive guidance in the LES CFD case as well as aid in running the simulations and processing data.

Finally, we are grateful for our colleagues, friends, and partners for their unwavering encouragement and patience through this experience. Their support has been a constant source of motivation and inspiration.

## **Contributions**

Individual section contributions by each team ember are labelled along with the section title. In addition to providing contributions to the discussion, conclusion, future work and results for their given section. Report was compiled and finalized by Paula.

# Abstract

This report presents a study of the design and manufacture of a reusable high-powered rocket aimed at achieving a 3km apogee. The project presents a comprehensive literature review to determine the best components and flight parameters, including nose cone geometry, fin design, engine class, recovery system, and flight path. Based on the extensive literature review, the final rocket design chosen included a Von Karman nose cone, swept-back fins with NACA0008 airfoil, a TeleMetrum flight computer, and a CO2 ejection system. To validate the chosen design, a comparative study was performed within a low-speed wind tunnel between a 3-fin configuration and a 4-fin configuration, by analysing the aerodynamic forces and stability at 4 different yaw angles at increasing speeds. Additionally, high speed wind tunnel testing was performed on a smaller scaled Von Karman nose cone to identify the pressure distribution of the airflow surrounding it and assess its aerodynamic properties. Furthermore, CFD simulations for subsonic and supersonic speeds were performed to analyse airflow around the full rocket to validate the obtained experimental results. Through a combination of experimental testing and computational analysis, the report provides insight into the design and optimisation of model rockets for 3km apogee with sustainability in mind.

# Table of Contents

<b>1. Introduction (Group)</b> .....	<b>11</b>
1.1 Rationale (motivation).....	11
1.2 Aims & Objectives .....	12
<b>2. Background Theory</b> .....	<b>13</b>
2.1 Rockets (Paula).....	13
2.1.1 Rocket anatomy (Ruben).....	13
2.1.2 Nose cones (Paula).....	15
2.1.3 Fins (Paula).....	15
2.2 Restoring Moments (Paula).....	16
2.3 Drag (Paula).....	17
2.4 Compressibility Effects/ Fluid dynamics (Ardrit).....	20
2.5 Shock & Expansion waves (Ardrit).....	21
2.6 Turbulence & Viscosity (Ardrit).....	24
2.7 Engine Class (Ruben).....	27
2.8 CFD (Ardrit).....	28
<b>3. Literature Review</b> .....	<b>31</b>
3.1 Rocket Nose Cones (Paula).....	31
3.2 Rocket Fins (Ruben).....	33
3.3 Rocket Engines (Ruben).....	34
3.4 Recovery Systems (Ruben).....	35
3.4.1 Single Parachute recovery .....	35
3.4.2 Multiple parachute (cluster) recovery .....	35
3.4.3 Glided recovery .....	35
3.4.5 Streamer recovery.....	36
3.4.6 Helicopter recovery .....	36
3.4.7 Net recovery .....	36
3.5 Expected Flight Envelope & OpenRocket (Ruben).....	36
3.5.1 Drag equations from OpenRocket.....	37
3.5.2 OpenRocket Validation.....	38
3.5.3 OpenRocket flight simulations for proposed model.....	38
<b>4. Research and Design</b> .....	<b>40</b>
4.1 Nose Cone (Paula).....	40
3.1.1 SolidWorks Nose Cone model.....	40
4.2 Fins (Paula).....	42
3.2.1 SolidWorks fin mounts designs .....	43
4.3 Proposed final Rocket Design (Ruben).....	46

4.4	<i>Proposed final components (Ruben)</i> .....	46
4.4.1	Material comparison.....	46
4.4.2	Avionics.....	47
4.4.3	Recovery.....	48
4.4.4	List of components.....	49
4.5	<i>Propulsion specifications (Ruben)</i> .....	50
4.5.1	Regulations.....	50
4.5.2	Suppliers & Proposition.....	50
<b>5.</b>	<b><i>Experimental Testing (Ardrit &amp; Paula)</i></b> .....	<b>51</b>
5.1	<i>Introduction</i> .....	51
5.2	<i>Low Speed Experimental testing (Paula)</i> .....	51
5.2.1	Apparatus.....	51
5.2.2	Six-component balance.....	52
5.2.3	Procedure.....	53
5.2.4	Relevant Calculations.....	55
5.2.5	Results.....	60
5.2.6	Limitations and Improvements.....	65
5.3	<i>High Speed Experimental Testing (Ardrit)</i> .....	65
	Equipment and Method.....	65
5.3.1	Pressure distribution.....	69
5.3.2	Schlieren Photograph.....	70
5.4	<i>CFD (Ardrit)</i> .....	71
5.4.1	Methodology.....	71
5.4.2	Axisymmetric.....	71
5.4.3	Validation.....	75
5.4.4	3D.....	79
<b>6.</b>	<b><i>Discussion</i></b> .....	<b>89</b>
<b>7.</b>	<b><i>Conclusion</i></b> .....	<b>92</b>
<b>8.</b>	<b><i>Suggestions for future work</i></b> .....	<b>93</b>
	<b><i>References</i></b> .....	<b>94</b>
	<b><i>Appendix A</i></b> .....	<b>97</b>
	<b><i>Appendix B</i></b> .....	<b>100</b>
	<b><i>Appendix C</i></b> .....	<b>101</b>

## List of Figures

Figure 1 - Rocket anatomy (Benson, n.d.).....	14
Figure 2 - Depiction of the difference in airflow around straight and swept fins .....	16
Figure 3 - Diagram depicting stable and unstable rockets (Finio, 2024; Newton M. , s.f.) .....	17
Figure 4 - Transonic flow over an aerofoil (Gatski & J.P., 2008) .....	21
Figure 5 - Left (T.B Gatski, J.P. Bonnet, 2008), Right QM lab expansion light, shock dark.....	22
Figure 6 - (Marciniak, 2016) .....	25
Figure 7 - (Marciniak, 2016) Turbulent vs Laminar boundary layer.....	26
Figure 8 – $U^+$ vs $Y^+$ (starccm user manual) .....	29
Figure 9: Drag coefficients against varying fineness ratios at Mach=1.55 (Hart & Katz, 1949) During the same period, notable researchers introduced innovative nose cone designs. Wolfgang Haack and William Sears developed the Sears-Haack conical body, later inspiring the Von Karman geometry....	31
Figure 10 - Comparison of Drag characteristics on various nose cone shapes (Gary & Crowell, 1996) .....	32
Figure 11 - Labelled tail fin (STAR, 2021) .....	33
Figure 12 - Altitude against time until apogee (Pro38 I350-16A engine) .....	39
Figure 13 - Mach number against time until apogee (Pro38 I350-16A engine).....	39
Figure 14 - Von Karman geometry for fineness ratio 5:1 for a needed diameter of 0.043m.....	41
Figure 15 - SolidWorks nose cone sketch.....	42
Figure 16 - Final SolidWorks nose cone component.....	42
Figure 17 - SolidWorks initial sketch of the fins' planform area.....	44
Figure 18 - Airfoil sketch of the NACA0008 with a chord of 19.1mm (fin tip) .....	44
Figure 19 - Airfoil sketch of the NACA0008 with a chord of 45.1mm (fin base) .....	44
Figure 20 - Final design for the 3-fin configuration - later used in wind tunnel testing - with an aerofoil close up.....	45
Figure 21 - Final design for the 4-fin configuration also used later in wind tunnel testing. ....	45
Figure 22 - <i>OpenRocket schematic of proposed 3 fins design</i> .....	46
Figure 23 - <i>OpenRocket schematic of proposed 4 fins design</i> .....	46
Figure 24 - Peregrine co2 system (tinderocketry, n.d.) .....	49
Figure 25 - Six-component balance for the measurement components and three moment components by means of strain gauges (Nouri, Mostafapour, Kamran, & Bohadori, 2014) where (a) is the setup for the pitching sensor, (b) is the sensor for the rolling sensor, (c) is the sensor for the drag, and (d) is the sensor for the yaw motion. The 'Data Recording' icon represents the ATI program. ....	53
Figure 26 -Reference frame used in the experiment (Cruchet-Pasos, 2023).....	54
Figure 27 - Low speed model rocket mounted on the 6-component balance within the wind tunnel with side view, back view, and top view presented from left to right. ....	55
Figure 28 - Plotted graph of the drag coefficient against the tested yaw angles for the 3-fin configuration.....	61
Figure 29 - Plotted graph of the drag coefficient against the tested yaw angles for the 4-fin configuration.....	61
Figure 30 - Plotted graph of the drag coefficient against the tested yaw angles for the 3-fin and 4-fin configuration.....	62
Figure 31 - Plotted graph of the lift coefficient against the tested yaw angles for the 3-fin configuration.....	62
Figure 32 - Plotted graph of the lift coefficient against the tested yaw angles for the 4-fin configuration.....	63
Figure 33 - Plotted graph of the lift coefficient against the tested yaw angles for the 3-fin and 4-fin configuration.....	63
Figure 34 - Plotted graph of the drag against the tested yaw angles for the 3-fin and 4-fin configuration.....	64

Figure 35 - Plotted graph of the lift against the tested yaw angles for the 3-fin and 4-fin configuration	64
Figure 36 – Tapping extraction holes	66
Figure 37 – Model dimensions	67
Figure 38 – The model	67
Figure 39 – Wind tunnel setup	68
Figure 40 – Pressure over time	69
Figure 41 – Schlieren Photo	70
Figure 42 – Axisymmetric mesh Far (top left) near (bottom right)	72
Figure 45 - Figure 46 – Y+ value against x/L	74
Figure 43 - Figure 44 – Drag against number of iterations	74
Figure 47 – Residuals graph for CFD	74
Figure 48 – Pstat/Psatg against x/L	75
Figure 49 – Cd against Mach number	76
Figure 50 – Shockwave angles vs Mach number(left), Shockwave location vs Mach number (right)	76
Figure 51 – Static pressure against x/L	77
Figure 52: Turbulent viscosity ratio contours for M = 2.0	78
Figure 53: Pressure contours for free stream M= 2.0	78
Figure 54: Mach contours for freestream M =2.0	78
Figure 55 – Leading edge mesh	80
Figure 56 – Trailing edge mesh	81
Figure 57 – experimental (experimental data contributed by Paula) vs cfd Drag	81
Figure 58 – Cd vs Mach	82
Figure 59: Cd vs Mach by computational methods as compared to OpenROcket (Open rocket data contribution by Ruben)	82
Figure 60: 3D CFD Pstat/Stag compared to previous data	83
Figure 61: Wall Y+ for 3D rocket	84
Figure 62 Mach and Pressure coefficient contours for M =0.8	85
Figure 63: Mach and pressure coefficient plots for M = 0.2	86
Figure 64: snappyHexMesh of rocket nose cone	87
Figure 65 – Turbulent velocity field (RMS)	88
Figure 66 – Time averaged velocity field	88
Figure 67 - Plotted data of the torque X experienced by the rocket	98
Figure 68 - Plotted data of the torque Y experienced by the rocket	99
Figure 69 - Plotted data of the torque Z experienced by the rocket	99

## List of Tables

Table 1 : Engine class impulse (UKRA)	27
Table 2: Simulation parameters	38
Table 3 - Material comparison (MatWeb, 2024)	46
Table 4 - Avionics comparison	47
Table 5 - Components cost and supplier table	49
Table 6 - Uncertainties of the apparatus	52
Table 7 - Resolutions for each component of the six-component balance	52
Table 8 - Atmospheric parameters of the experiment	57
Table 9 - General wind tunnel calculated values	58
Table 10 - Processed data for low wind tunnel experimenting	60
Table 11 – Model parameters	66
Table 12 – Tapping locations	66

Table 13 – Average pressure ratio with tapping.....	70
Table 14 – Schlieren measurements .....	70
Table 15 – Mesh parameters .....	72
Table 16 – Table with values for CFD parameters .....	73
Table 17 -CFD attained values .....	75
Table 18 - CFD attained values .....	75
Table 19 – Mesh properties .....	79
Table 20 – Mesh properties .....	80
Table 21 – Cp vs Mach .....	83
Table 22 – Open rocket vs CFD .....	83
Table 23 – Mesh properties .....	87
Table 24 - Averaged raw data collected with the ATI program for the 3-fin configuration .....	97
Table 25 - Averaged raw data collected with the ATI program for the 4-fin configuration .....	97

## List of Abbreviations

<b>UKRA</b>	United Kingdom Rocket Association
<b>CFD</b>	Computational Fluid Dynamics
<b>LES</b>	Large Eddy Simulation
<b>RANS</b>	Reynolds Averaged Navier-Stokes

## List of Symbols

<b><math>A_{ref}</math></b>	Reference area
<b><math>A_{wet,body}</math></b>	Wetted area of body
<b><math>A_{wet,fins}</math></b>	Wetted area of fins
<b><math>C_d</math></b>	Drag coefficient
<b><math>C_f</math></b>	Coefficient of friction
<b><math>C_{fc}</math></b>	Coefficient of friction after compressible correction
<b><math>f_b</math></b>	fineness ratio of body tube
<b><math>f_n</math></b>	fineness ratio of nose cone
<b><math>\theta_{LE}</math></b>	Leading edge angle = 90 – sweep angle
<b><math>M</math></b>	Mach number
<b><math>k</math></b>	lift dependent component of drag coefficient

$t$	Thickness of rocket body
$\bar{c}$	Mean aerodynamic chord length of fins
$D$	Drag
$L$	Lift
$C_L$	Lift coefficient
$L/D$	Length to diameter ratio
$C_{D_N}$	Drag coefficient of the nose cone
$C_{D_{BT}}$	Drag coefficient of the body tube
$C_{D_F}$	Drag coefficient of the fins
$S_{BT}$	Cross-sectional area of the body tube
$S_w$	Wetted area of the rocket
$S_F$	Planform area of the fins
$C_R$	Root chord of the fins
$C_p$	Centre of Pressure
$Re$	Reynolds number
$x/L$	Position over reference length ratio

# 1. Introduction (Group)

This report presents the research and development efforts to design and manufacture a high performance I class model rocket. This project aims to overachieve by establishing a new UK altitude record in the I class. With the aid, expertise and facilities of the Queen Mary SEMS department, this project aims to contribute to the advancement of high-performance rocketry through the development of a more efficient I class rocket design.

## 1.1 Rationale (motivation)

Rockets are vehicles that use jet propulsion to travel through space or the atmosphere. Unlike airplanes or jets, they don't rely on air intake for combustion. Model rocketry is a branch of rocketry that focuses on building and launching miniature rockets for recreational and educational purposes. High-powered rocketry is a branch of rocketry that builds and launches rockets with significantly more power compared to traditional model rockets.

The past decade has witnessed a remarkable surge in space activity, with a staggering number of 2478 objects launched in 2022 alone (Stasko, 2022). Multiple satellites now circle Earth, providing essential services like GPS navigation and telecommunications. They also support scientific missions that unlock the mysteries of the universe. Furthermore, rockets enable crucial applications like weather forecasting, environmental monitoring, and disaster relief efforts, directly impacting human safety and well-being. Rockets have become the workhorses of space exploration and connectivity. This upward trend in launches underscores the growing importance of rocketry. However, it also necessitates advancements in reusability and efficiency to minimize waste and costs. Rocketry competitions serve as a valuable platform for engineers to showcase their skills in this critical area. These competitions often incorporate waste and cost reduction considerations into their rules, providing engineers with the opportunity to develop and demonstrate solutions for a more sustainable future in space exploration.

The European Rocketry Challenge (EuRoC) is an annual competition designed for student teams across Europe to showcase their skills in designing, building, and launching their own model rockets. The European Rocketry Challenge directly aligns with Portugal Space's strategic objectives, particularly those focused on fostering the growth of the Portuguese space sector (Lopes, 2021). The competition involves various challenges related to rocket design and performance. Such as, achieving a specific target altitude, Optimizing rocket design for maximum efficiency. EuRoC competition states several important rules. No toxic propellants can be used. A notable list stated by EuRoC includes Ammonium perchlorate composite propellant (APCP), 'rocket candy' and kerosene. Another rule stated is the rocket must be recovered in a safe manner, this is achieved by having a descent rate less than 9 m/s. This

project will use the rules and regulation of the EuRoc competition as a guide to ensure that the rocket design is safe and adequate for launch.

## 1.2 Aims & Objectives

The main aim of this project was to successfully design and manufacture a reusable I-class rocket that could reach a 3km apogee. This aim had to be achieved by completing a set of objectives. The main objective was to carefully design a rocket that could fulfil the requirements of its mission whilst remaining functional and efficient. To achieve this goal, theoretical research and real-world practical experimentation was used.

The first objective was to do thorough research of prior existing knowledge through an extensive literature review to create a starting point for the design of the rocket. Through an examination of relevant academic literature, the objective was to develop a deep understanding of the fundamental concepts around rocketry and the long process of choosing its components. It was important to conduct this review to help shape the later design choices and to guarantee that state-of-the-art innovations were incorporated into the rocket.

The next objective was to build a smaller scale prototype rocket by building the design on the groundwork established by the literature review. This initial stage had two objectives in itself: to help with iterative design changes and to validate the application of the chosen components found in the literature review. The objective was to carry out low-speed and high-speed wind tunnel testing with the prototype: to assess the aerodynamic performance of the rocket's fin configuration and to assess the dynamic behaviour of the Von Karman nose cone respectively. The objective of the low-speed tunnel experimental testing was to assess whether the 3-fin configuration or the 4-fin configuration provided the best combination of drag, lift and torque, ultimately aiming to attain the best flight trajectory. Additionally, the objective of the high-speed wind tunnel testing was to validate the reasoning behind the Von Karman nose cone choice and how it would positively affect the mission's ability to accomplish its goals in supersonic flight.

The report will additionally set out to experimentally test the performance of the Von Karman nose cone for supersonic flight. In order to do this a small-scale model will be built to for testing within a supersonic wind tunnel at a flow speed of Mach 2.0. Pressure distribution around the nose cone is to be measured along with the shockwave angle in order to supply a validation data set for CFD calculations.

In conjunction, several CFD calculations will be conducted for the subsonic regime up to Mach 0.8 and trans-supersonic regime from  $0.8 < \text{Mach} < 1.4$  to encapsulate the entire flight envelope. Coefficients of drag will be computed numerically, and approximations will be made regarding the centre of pressure and stability of the rocket. Calculations will progress from Axisymmetric RANS  $\rightarrow$  3D RANS  $\rightarrow$  LES.

## **2. Background Theory**

### **2.1 Rockets (Paula)**

Rockets have been and still are an essential part in the development of our understanding beyond the confines of Earth's atmosphere since the 1950s. At their core, rockets follow Newton's third law principle: for every action, there is an equal and opposite reaction (Newton's Principia: the mathematical principles of natural philosophy, 1846); in this case, ejecting exhaust gases at enormous speeds to create thrust, which allows them to accelerate vertically against drag and gravity. Rockets were initially invented exclusively for space exploration, sparking a sudden fascination and awe across the world's population. They transitioned from being expensive and exclusive for government use, to finding applications at a smaller scale known as model rockets. Also called miniature astronautics, these rockets are essentially miniature versions of aerospace vehicles that vary from being scientific experimentation to recreational technologies. The first model rockets were created and flown in the USA in 1957 by the late shoe store owner Orville H. Carlisle (Stine & Stine, 2004).

The efficient and more capable rockets we know now are a result of advancements in the industry dating back only two decades. While truly fascinating, the engineering principles behind such invention need to be studied and understood in order to successfully design and manufacture even the smallest of these models, and hence pave the way for future developments in space exploration.

#### **2.1.1 Rocket anatomy (Ruben)**

A high-powered rocket consists of multiple components that sinuously work with one another to achieve peak performance. Most Rockets include a payload that is to be deployed during flight. A payload can be used for numerous reasons such as satellite deployment and experimental testing. In this report we will not be designing a rocket with a payload. This is because we are mainly focussing on the performance aspect of a rocket.

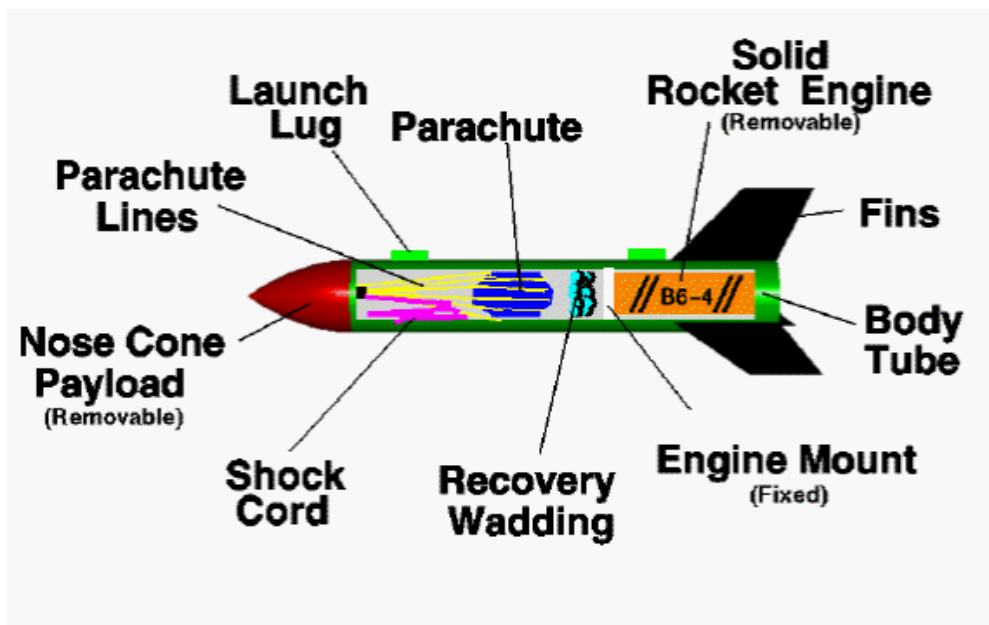


Figure 1 - Rocket anatomy (Benson, n.d.)

The airframe (Body tube) forms the core structure of the rocket, housing the propulsion system, recovery system and the avionics that supports the nose cone and the fins. The airframe is a tube, constructed from lightweight yet high-strength materials like carbon fibre or reinforced fibre glass.

The fins are pieces attached at the rear of the rocket. These external appendages provide crucial stability during flight. Fin design is critical, as they counteract torque generated by the motor and maintain the rocket's desired trajectory (Pektaş, 2019). Factors like fin size, placement, and material selection are meticulously considered to ensure optimal performance and this will be discussed in more detail further into the report.

The front of the rocket houses the nose cone. The nose cone plays a critical role in minimizing aerodynamic drag during flight as it's the part of the rocket incident to the airflow. Ogive, conical, and von Karman shapes are commonly employed, each offering distinct performance advantages at different velocity ranges.

Another important component is the recovery system. The recovery system consists of a parachute and launch lug that is attached to the nose cone via the shock cord. This system ensures the safe return of the rocket the most common method requiring a deployment mechanism triggered by an electronic timer or an altimeter-activated system. For higher performance rockets, drogue parachutes might be deployed first to slow the descent before the main parachute deploys (Newton M. , n.d.).

The avionics bay is a crucial component in a rocket's anatomy. The avionics bay is typically located in either the nose cone or the body tube or optimal signal reception or the body tube for efficient packaging.

The avionics bay consists of a flight computers and other electronic components connected to a battery. These systems can track flight data, trigger recovery deployments, and provide valuable telemetry for post-flight analysis.

### **2.1.2 Nose cones (Paula)**

The nose cone is a streamlined, normally conical component that is placed at a rocket's leading end. Its main purpose is to reshape the incoming airflow and therefore, reduce aerodynamic drag, and improve the rocket's speed and stability during ascent. For each rocket and its specific mission requirement, a nose shape must be carefully chosen according to what the aim of the flight is. Various nose cones such as the Von Karman geometry, are employed for subsonic and transonic mission flights because they generally meet the requirements and desired flight characteristics of model rockets. Moreover, nose cones are designed to provide stability during flight by reducing pitch and yaw deviations. At lower speeds, there is less risk of aerodynamic forces affecting the flight trajectory and explains why model rockets don't necessarily require sharp nose cones - unlike real rockets. For a supersonic rocket, a highly pointed nose might be chosen as these are better at cutting through incoming shockwaves. However, for a recreational rocket, a blunter nose might be chosen because it travels at lower speeds which do not create the aforementioned shockwaves and therefore, does not need to break through these. Factors such as the length, diameter and curvature of the geometry must be considered during the design process in order to optimise its aerodynamic performance while still meeting mission requirements – such as carrying payload – should they have one. Understanding all the aerodynamic forces surrounding a rocket during flight is crucial in choosing an appropriate nose cone geometry during the development of the design, ultimately contributing to the aim of the mission.

### **2.1.3 Fins (Paula)**

Fins are crucial components in rockets, serving as a means to stabilise and control the rocket's flight path. They are almost always positioned at the rear end of the rocket and take up approximately 15% of its total length, providing stability during flight. Whilst the nose cone serves as means to reduce the yaw and pitching moments, the fins exist to counteract the forces that cause these deviations to take place, and it is why both these components create such a good combination for rockets. The shape and configuration of the fins, once again, need to be chosen to ensure the precise flight control required for their specific mission. By creating a combination of lift and drag, the fins help the rocket maintain its orientation and prevent undesired oscillation by creating restoring moments. Various fin shapes, including rectangular, straight tapered, swept-tapered, clipped-delta, and elliptical geometries, are consistently evaluated during the design process determine which one would fit the mission requirement

best. Moreover, the number and configuration of the fins must be tailored to create as little drag as possible to avoid the loss of too much thrust.

Swept shaped fins, as proven by their use on almost all aircrafts, are used for supersonic flight conditions because they cut through shockwaves more efficiently. More specifically, swept fins will reduce the effective flow speed and therefore will help mitigate the effects of shockwaves more efficiently compared to straight fins. To go into more depth: at supersonic speeds, the compression of air in front of the fins will cause shockwaves to form and will create high-pressure zones in this region which may lead to drag and instability. Swept fins are slanted away from the airflow direction, which – as mentioned previously – can assist in lowering the fins' effective flow speed; therefore, minimising the strength of the shockwaves the fins experience. This flow speed reduction is what will decrease drag and enhance overall aerodynamic performance.

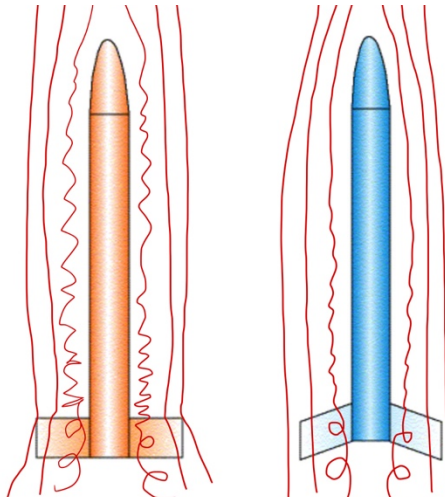


*Figure 2 - Depiction of the difference in airflow around straight and swept fins*

Wind tunnel testing along with computational fluid dynamics (CFD) simulations are commonly used to analyse airflow patterns and design fin geometries for optimal flight trajectories. Fins are normally made with sturdy yet lightweight materials – normally composite materials or aluminium – in order to withstand aerodynamic forces without adding unnecessary weight to the rocket. Overall, fins greatly contribute to the success of a rocket's mission by ensuring they stay stable from lift-off to recovery system deployment.

## **2.2 Restoring Moments (Paula)**

Restoring moments are the forces that act on rockets to return them to its stable position when it deviates from its mission path due to external aerodynamic forces or control surfaces (Anderson, 2016). These are the forces that counteract the disturbances that affect the rocket, and they are essential for achieving

stable flight trajectories and controlling its orientation. These forces are generally created due to the fins which are the ones interacting with the surrounding airflow to produce stabilising forces.

Stability is the ability of a rocket to return to its equilibrium position or its intended flight path. A stable rocket will have the ability to autocorrect detours from its original path. Factors affecting the stability of a rocket include the location of the centre of gravity, mass distribution and the aerodynamic surfaces. A stable rocket will naturally return to a straight flight path after being disturbed if the centre of gravity is ahead of the centre of pressure (Sutton & Biblarz, 2001). These factors always need to be considered for the design and testing in order to provide optimal stability.

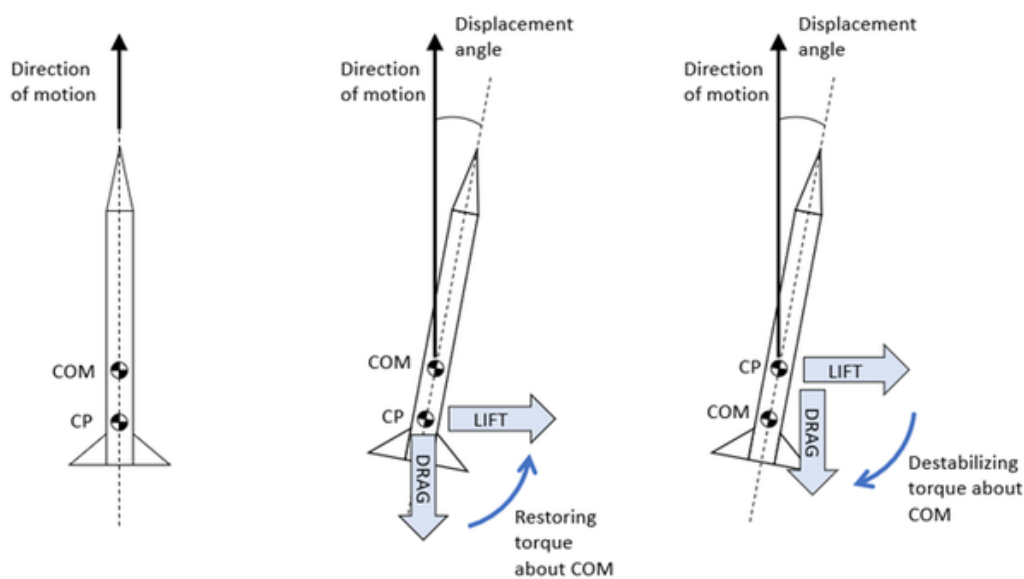


Figure 3 - Diagram depicting stable and unstable rockets (Finio, 2024; Newton M. , s.f.).

To analyse the restoring moments and stability, the aerodynamic forces and moments acting on the rocket have to be assessed. This can be done through wind tunnel testing or CFD simulations to evaluate these factors and optimise design.

## 2.3 Drag (Paula)

Technically speaking, drag is the resistance that arises when bodies move through liquids such as water or air. For example, the water in a swimming pool will oppose attempts to move through it. This is called hydrodynamic drag which means the drag that results from the water's movement around a body. Another example is the force of air that can be felt on the hand and arm when stuck out the window of a moving car; the air can be felt pushing at different angles: up, down and sometimes just back.

The drag of a rocket is essentially the sum of the drag of all its components: the nose cone, the body tube, and the fins, and it is calculated with *Equation 1*.

$$D = \frac{1}{2}\rho V^2 AC_D \quad (Eq. 1)$$

where  $\rho$  is the density of the air inside the tunnel,  $V$  is the velocity of the airflow, and  $A$  is the reference area (in this case the cross-sectional area of the body tube).

The drag on the nose cone is composed of skin friction and pressure drag, but mainly of the latter. It is widely acknowledged that a blunt nose cone will experience more drag than one with a sharper geometry, however this only holds true up to a certain point. Only real rockets that fly at supersonic speeds, will fully benefit from very pointed nose cones because these can cut through the shockwaves that are created at such high speeds. More rounded nose cones are better for model rockets that travel at subsonic and transonic speeds because they don't build up shockwaves. A good value of coefficient of drag for the nose cone exclusively is ideal if  $C_{DN} \approx 0.004N$  (Gregorek, 1970).

The drag on the body tube on the other hand, is almost exclusively skin friction. It is directly affected by the length to diameter ratio ( $L/D$ ) and as this increases, friction drag becomes more of a concern; therefore, it is easy to anticipate a large amount of skin friction on model rockets. The level of the drag force will depend on the type of boundary layer that covers the model; showing the lowest drag where the boundary layer is laminar. The coefficient of drag of the nose cone and body tube are normally calculated using *Equation 2* (Gregorek, 1970).

$$C_{DN} + C_{DBT} = 1.02C_f \left[ 1 + \frac{1.5}{\left(\frac{L}{D}\right)^{\frac{3}{2}}} \right] \frac{S_w}{S_{BT}} \quad (Eq. 2)$$

Where  $C_{DN}$  is the drag coefficient of the nose cone,  $C_{DBT}$  is the drag coefficient of the body tube,  $C_f$  is the skin friction coefficient of the rocket,  $S_{BT}$  is the cross-sectional area of the body tube, and  $S_w$  is the wetted area of the whole rocket. The wetted area essentially being the surface of the rocket that would get wet if it were dipped in water.

For rocket bodies, the cross-sectional area of the body tube is used as the reference area to measure drag, however, for fins – because of their normally small thickness – the planform area, denoted at  $S_F$  is used. As well as the body tube, the drag of the fins is primarily composed of skin friction. The ideal choice for a model rocket out of the common shapes is the clipped-data - as proven by Garance (2023) - as it presented the best aerodynamic efficiency for a model rocket's pre-determined objectives.

In terms of drag, the tip of the fins is the most efficient part; where the airflow is nice and smooth because it is outside the turbulent region caused by air flowing over the nose of the rocket. The drag coefficient of the fins can be calculated with *Equation 3* and can vary in model rockets from 0.009N to 0.05N at 0° yaw angle (Gregorek, 1970).

$$C_{D_F} = 12C_f \left[ 1 + \frac{t}{c} \right] \frac{S_F}{S_{BT}} \quad (Eq. 3)$$

Where  $C_{D_F}$  is the drag coefficient of the fins,  $S_F$  is the planform area of the fins, and  $t/c$  is the taper ratio of the fins; where  $t$  is the thickness and  $c$  is the chord of the aerofoil.

$$S_F = \frac{C_R}{2} [b - d] \times n^{\circ} \text{ of fins} \quad (Eq. 4)$$

Where  $C_R$  is the chord length at the root of the fin,  $d$  is the diameter of the body tube, and  $b$  is the distance from one tip of one fin to the tip of the opposite fin across the rocket. In other words,  $[b-d]$  is twice the span of one fin. *Equation 4* shows that the drag coefficient of the fins is dependent on the number of fins, meaning that if this number were to be increased from 3 to 4, the configuration featuring 4 fins would attain an increase of 33% in  $C_{D_F}$  in comparison to that of the 3-fin.

Much like the drag, the total drag coefficient of the rocket can be described as the sum of the drag coefficients of all its components (see *Equation 5*) where  $C_{D_N}$ ,  $C_{D_{BT}}$  and  $C_{D_F}$  are the drag coefficients the nose cone, the body tube and the fins respectively.

$$C_D = C_{D_N} + C_{D_{BT}} + C_{D_F} \quad (Eq. 5)$$

## 2.4 Compressibility Effects/ Fluid dynamics (Ardrit)

While many problems allow for the assumption of air as an incompressible fluid, for high-speed flows such as those experienced during the flight of a model rocket, compressibility effects of air must be taken into account. The Mach number of a flow can be described as the ratio of the flow velocity to the speed of sound in that medium (*Equation 6*), where a Mach number over 1.0 denotes a Supersonic flow, and below 1.0 denotes a subsonic flow. Within this there are several sub regimes in which a fluid may act differently including  $M < 0.3$  where the change in density with velocity is negligible and air can be assumed to be incompressible,  $0.7 < M < 1.0$  where the flow can be assumed to be transonic with regions being either below or above the speed of sound, and  $M > 5.0$  where a flow can be considered hypersonic and thermal effects are significantly larger (Urzay, 2020). The Mach number of a flow can be found by velocity  $v$  and speed of sound  $c$ :

$$M = \frac{v}{c} \quad (\text{Eq. 6})$$

In which for a flow with a constant ratio of specific heat ( $\gamma$ ), as for isentropic flows below the hypersonic region, the speed of sound can be found as a function of specific heat ratio, gas constant ( $R$ ) and absolute temperature ( $T$ ).

$$c = \sqrt{\gamma RT} \quad (\text{Eq. 7})$$

While the behavior of a compressible flow differs to that of an incompressible, there are still three key laws in which subsonic and supersonic flows must obey. Since mass and energy cannot be created or destroyed, this leads to the three laws in: conservation of mass, conservation of momentum, and conservation of energy. The conservation of mass first presented by Antoine Lavoisier, stating that the total mass before and after a process must remain constant, within the field of fluid dynamics is represented in the continuity equation (*Equation 8*), governing the transport of any particular conserved quantity of the fluid.

The conservation of momentum is most famously known by Newton's second law as "F=ma", stating that the rate of change of momentum of a body is equal to the force applied onto the body. While this is conceptually simple for a solid body, in the realm of fluid dynamics with shear, viscous and pressure forces, leads to a more complex set of equations in the form of the Navier-Stokes Equations including convective, pressure, body force and diffusion terms. The Navier-Stokes momentum equation (*Equation 9*) is given in terms of velocity  $v$ , pressure  $p$ , free stream density  $\rho$ , and dynamic viscosity  $\mu$ , commonly used in conjunction with the continuity equation (*Equation 8*).

$$\frac{Dp}{Dt} + \rho(\nabla \cdot \vec{V}) = 0 \quad (\text{Eq. 8})$$

$$\rho \left( \frac{\partial V}{\partial t} + V \cdot \nabla V \right) = -\nabla p + \mu \nabla^2 \vec{V} + \rho \vec{g} \quad (\text{Eq. 9})$$

Where  $\nabla$  is the gradient operator referring to the partial derivative in all relevant axis.

Finally, the conservation of energy is governed by the first law of thermodynamics in which energy transfer is classified in two main forms, heat and thermal work, and must remain constant throughout an enclosed system. Additionally, the momentum equation together with the ideal gas law and properties of isentropic flow can be formed to give the relation between the flow Mach number and change in density in *Equation 10*. This shows that the change in density is directly proportional to the square of the Mach number, meaning that for low Mach numbers the change in density is deemed negligible with a Mach number of 0.3 leading to a 5% change in density, and for high-speed aerodynamic flows the density is much more sensitive to changes in Mach number.

$$-M^2 \frac{dV}{V} = \frac{d\rho}{\rho} \quad (\text{Eq. 10})$$

## 2.5 Shock & Expansion waves (Ardrit)

By its inherent definition, the speed of sound is that in which particles within a field are able to communicate and transfer energy, therefore it is the speed at which perturbations within a flow field are transported. Again, for conventional flow problems this is not an issue however as the flow velocity begins approaching the speed of sound additional behaviors begin to occur. As a body is rarely ever completely uniform this means that the local velocity over different surfaces will be of different magnitudes meaning that while the flow over the global body may be below the sonic threshold, regions around the body will experience supersonic flow, this is known as the transonic region.

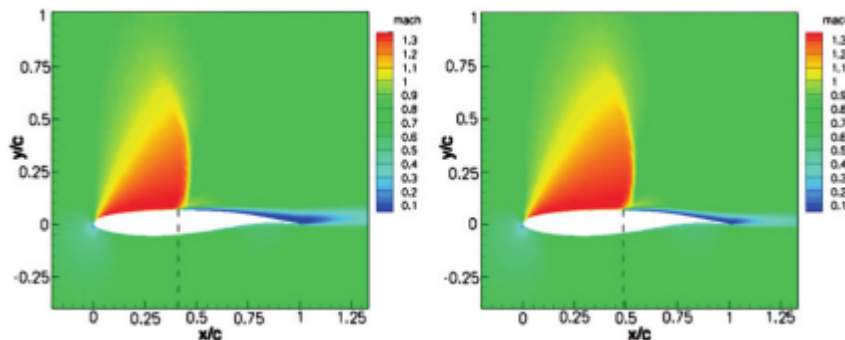


Figure 4 - Transonic flow over an aerofoil (Gatski & J.P., 2008)

A prime example of a transonic flow is one as can be seen in *Figure 4*. The flow over the suction side of an airfoil accelerates reaching the speed of sound, at which point a shockwave is formed and

an almost step change occurs in the velocity. The critical Mach number can be defined as the Mach number at which shockwaves can first be observed over a body, and those that happen in the transonic region are known as Normal shockwaves as they act perpendicular to the flow direction. Normal shockwaves have several implications on a body including an increase in drag, disturbance in flow, reduction in effects of control surfaces, and transonic buffeting. Alterations in controls include phenomena such as Mach tuck where the shockwave alters the center of pressure causing the pitch down moment of an aircraft, and flow separation leading to a reversal in desired control inputs. As for buffeting, flow separation over the top surface of an airfoil can cause significant structural vibrations and aeroelastic effects, in the best case increasing cyclic loading and in the worst case causing a loss of control of said surface.

As model rockets rely on rear fins to stabilize flight, these surfaces are susceptible to the aforementioned transonic effects. The rocket dynamics in section demonstrate this as the fins angle of attack is increased with rocket perturbations and crosswinds, meaning that normal shockwaves are likely to occur. The transonic performance of the fins will be a design parameter discussed further in /.

Once a body has passed the transonic regime it will experience shockwaves on its leading and trailing edges due to the turning angle of the flow, the nature of which is dependent on the aerodynamic shape of the body. For a sharp leading edge in a transonic flow an oblique shockwave will occur attached to the leading edge of the surface causing a discontinuity in the flow near the body. For blunt bodies a detached bow shockwave will occur a distance in front of the body where the air in front of the body has been compressed. As the shockwaves are a result of the compressive turning angle, a supersonic and subsonic solution exists for the flow past the shockwave, nevertheless, a shockwave is always an instantaneous change in flow field in which the pressure is increased and the velocity is decreased. In contrary to shockwaves, a flow experiencing a negative turning angle is subject to a gradual fan of expansion waves in which the flow is expanded, pressure reduced and velocity increased.

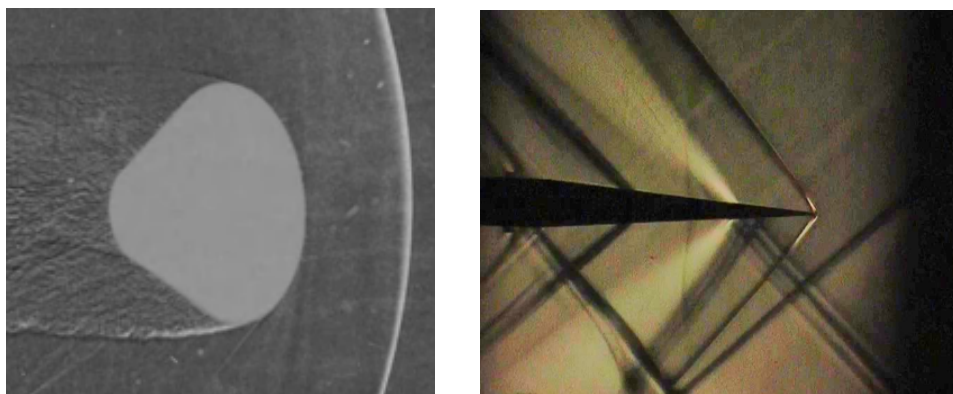


Figure 5 - Left (T.B Gatski, J.P. Bonnet, 2008), Right QM lab expansion light, shock dark

For compressible effects where changes in condition are gradual, such as those in subsonic conditions, convergent nozzles, and supersonic angles which produce an expansion fan, the flow can be assumed to have no change in the enthalpy of the system, is theoretically reversible, and is said to be Isentropic. Where Enthalpy is defined as the sum of internal energy and product of pressure and volume, in which the enthalpy of a system remains constant in a system when no work is done to or by the system such as a heat transfer discontinuity. For these isentropic flows, the total condition of a variable remains constant throughout, therefore a relation between the local and total condition for any stage in the isentropic flow is governed by the Isentropic Flow equations (Hall, 2021) as well as the Prandtl-Meyer Angle equations (Hall). For flows in which shockwaves occur, there is a discontinuity in the flow field and a change in enthalpy across the shockwave, this no longer satisfies the isentropic equations and the equations for normal shock and oblique shock must be considered.

The general drag for a subsonic rocket in terms of base, induced and friction drag has been mentioned in 2.2, however when considering the trans-supersonic regime a factor of wave drag is also present. In this an initial and gradual increase in drag is noticed at the onset of shockwaves during transonic flight up to the drag divergence Mach number at which point a large gradient in the drag is present (Grumman, Roman, & Rajkovic, 1997). This is due to both the shear presence of shockwaves inducing drag as well as the disruption of the boundary layer which in turn may cause a significant increase in flow separation or a large increase in thickness due to the increased pressure. For a constant coefficient of lift, (Lynch,2012), defined the Drag Divergence Mach number  $M_{DD}$  as the point at which;

$$\frac{dC_D}{dM} = 0.1 \quad (Eq. 11)$$

Wave drag can be a particular issue for a rocket as it classed as a zero lift drag, meaning that it is present no matter the lift being produced, where as lift due to the restoring moment is not applicable during steady flight with no perturbations, therefore an effect to reduce the induction of shockwaves should be sought after.

Whats more is that shockwaves are not largely dissipative and can span a great length from their origin, this combined with their characteristic discontinuity in flows and disruption of boundary layers could lead to possible disturbances on nearby surfaces, such as the fins and body tube of a rocket. An additional characteristic of a shockwave is that in which they are reflected, both with each other and nearby surfaces, as also outlined by (Wang, 2021), greatly increasing the complexity of a trans-supersonic flow field particularly in regions with several nearby surfaces, e.g. fin section of a rocket. Similarly, expansion waves are also reflected off surfaces as well as have the ability to form a contact surface at non aerodynamically shaped trailing edges of a body, where the flow from the top and

bottom surface coincide and deflect. These effects combined can potentially cause significant, unpredictable effects on the flow separation and boundary layer towards the trailing edge.

## 2.6 Turbulence & Viscosity (Ardrit)

Fluid flows can largely be separated into two categories, laminar and turbulent, of which laminar flows are mainly a theoretical phenomena and rarely present in the real world. A laminar flow can be seen as one where the velocity magnitude along a given streamline is constant and non fluctuatory, where as a turbulent flow will possess a mean velocity magnitude about which there are random fluctuations. The velocity at any point in time within the flow can be depicted with the statistical representation of a mean velocity  $\bar{u}$  and a fluctuation  $u'$  about that mean velocity as;

$$u = \bar{u} + u' \quad (Eq. 12)$$

Where  $u' = 0$  in the case of a laminar flow. The velocity fluctuation can be determined in several ways, most commonly in the Temporal (time) averaged solution where an average fluctuation is taken over time. Alternative methods include a space averaged approach as well as an ensemble approach, where an experiment is conducted and repeated to find the fluctuations over several runs.

A non dimensional value is used to represent the relative turbulence of a given flow as the ratio of inertial to viscous forces experienced, this value being the Reynolds number (Re). The inertial forces within a flow are a function of the density of the fluid, free stream velocity and a reference length. The reference length can vary depending on the type of flow and is generally taken as the diameter of a pipe for an internal flow, or a streamwise length such as the chord length of an aerofoil for that of an external flow. The viscous shear forces then being represented by the dynamic viscosity ( $\mu$ ) gives the non dimensional Reynolds number to be;

$$Re = \frac{\rho u L}{\mu} \quad (Eq. 13)$$

Where the density over dynamics viscosity term can also be represented as the kinematic viscosity of the fluid giving;

$$Re = \frac{uL}{\nu}, \quad \nu = \frac{\mu}{\rho} \quad (Eq. 14)$$

As a reference, (Davidson, 2022) states that a flow begins to transition into turbulence for a pipe flow at  $Re \sim 2300$ , and at  $Re \sim 500,000$  for an external boundary layer flow. While turbulence is irregular and unpredictable, it must still adhere to the conservation equations previously mentioned in Equation 8-9, Where however complex it may be, a solution to the Navier-Stokes equations must exist. Turbulence within a flow field represents as a swirling effect known as an eddy. These eddies

can be seen in a flow at various scales with the largest eddies being created generally by disturbances in a field and high velocities, these eddies are dissipative in nature and will decompose, transferring their energy to a smaller eddy up until the smallest time scale, at which the turbulent kinetic energy is entirely dissipated into the fluid in the form of heat. As the conservation equations must be maintained, energy can not be created or destroyed meaning that for turbulent eddies, the total energy to create the eddy at the largest scale must be fully transferred along the scale and dissipated back into the fluid at the smallest scale. Eddies are created at the size of the relative flow scale, such as a nozzle exit diameter, and are dependent on the function of flow velocity, length scale and kinematic viscosity, having a large Reynolds number as described in *Equation 13*, meaning they are largely dominated by the viscous regime. Kolmogorov's eddy cascade hypothesis, as discussed by (Aliabadi, 2022), defines this cascade of energy from the larger Integral length scale, to the smallest eddies at the Kolmogorov length scale, where eddies fully break down due to the large viscous effects. Where the Kolmogorov length scale is given in terms of the kinematic viscosity and turbulent dissipation rate  $\epsilon$  by;

$$\eta = \left( \frac{\nu^3}{\epsilon} \right)^{\frac{1}{4}} \quad (\text{Eq. 15})$$

In the realm of fluid dynamics, the fluid in question is usually one which exhibits Newtonian behaviour, in that they follow Newton's Law of Viscosity, stating that the shear stress of a given small volume is a factor of the dynamic viscosity and gradient of velocity over the perpendicular distance.

$$\tau = \mu \frac{du}{dy} \quad (\text{Eq. 17})$$

In which applying a small angle approximation results in;

$$\tau = \mu \dot{\gamma} \quad (\text{Eq. 18})$$

For flows near a frictional wall, this shear stress results in a velocity gradient perpendicular to the wall, where the magnitude of velocity at the wall is zero. This results in a boundary layer flow near the wall in which the total boundary layer thickness is that in which the velocity reaches 99% of the free stream velocity. Boundary layers also exhibit the same laminar and turbulent tendencies and therefore a shear dominated laminar boundary layer will have a steeper gradient whereas a viscous dominated turbulent layer will be less affected. Whereas the laminar boundary layer is one consistent region, the turbulent boundary consists of three sub regions; a laminar sublayer in which viscous forces dominate and a low velocity gradient is present, a buffer layer where both viscous

Figure 6 - (Marciniak, 2016)

and inertial effects occur, and a turbulent layer where the flow is purely dominated by inertial forces. A good representation of this can be seen from (Marciniak, 2016)

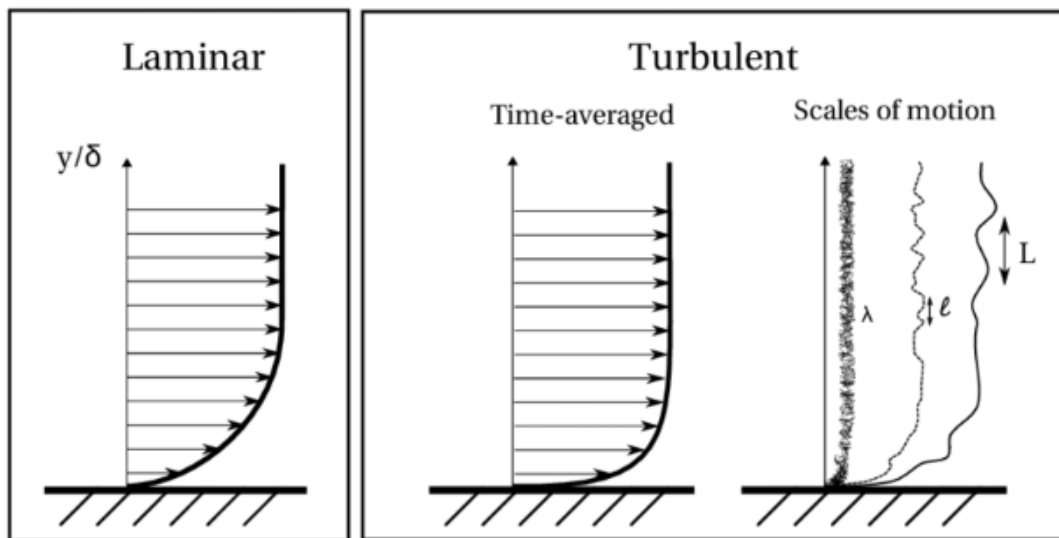


Figure 7 - (Marciniak, 2016) Turbulent vs Laminar boundary layer

For the flow over a flat surface two main approximations exist, being the Blasius solution for laminar flow and the turbulent solution, as laid out by (Kundu & Cohen, 2004);

Laminar

$$\delta_{99} = \frac{4.9}{\sqrt{Re_x}} \quad (Eq. 19)$$

Turbulent

$$\delta_{99} = 0.37 \frac{x}{Re_x^{1/5}} \quad (Eq. 20)$$

## 2.7 Engine Class (Ruben)

Model rocket engines are categorized by engine classes, which reflect their overall power. These classes are based on the total impulse, which is a measure of the total thrust produced by the engine over its burning time. Engine classes are designated by letters, ranging from A to O. As the letter progresses alphabetically, the engine's total impulse increases. Each letter class corresponds to a specific range of total impulse measured in Newton-seconds. These ranges are typically doubled with each step up the alphabet.

*Table 1 : Engine class impulse (UKRA)*

Engine class	Total Impulse (Ns)
A	1.26-2.50
B	2.51-5.00
C	5.01-10.00
D	10.01-20.00
E	20.01-40.00
F	40.01-80.00
G	80.01-160.00
H	161.01-320.00
I	320.01-640.00
J	640.01-1280
K	1280.01-25060
L	2560.01-5120
M	5120.01-10240
N	10240.01-20480
O	20480.01-40960

Model rocket engines are classified using a system of letters and numbers to categorize their performance characteristics, for example I350-16. The first number represents the average thrust in newtons. The second number signifies the delay time in seconds. The delay time represents the interval between engine burnout and the activation of the ejection charge.

Based on the engine class, rockets are put into a category. Model Rockets are categorized from A to G with 2 sup categories in this range. Rockets using Engines from range A to D fall into the subcategory

of low power whilst rockets in the range of E to G fall into the subcategory of Mid power. Rockets using engines from H to O are called High powered Rockets. In this range, there are 3 subcategories; level 1 which is H to I, level 2 which is J to L and level 3 which is M to O.

## 2.8 CFD (Ardrit)

Computational Fluid Dynamics is a method in which an iterative scheme is used to solve the Navier-Stokes equations for a given fluid dynamics problem. A typical CFD calculation incorporates a spatial discretization of the fluid domain and a set of methods and solves for the governing equations. The domain can be split into cells, or faces for a 2D/ axisymmetric case, and can be point wise in methods such as finite difference, predicting point values within the flow, or volume wise within the cell, in which cell faces interface with eachother to transport properties and maintain the conservation laws.

As the Navier-Stokes equations are a complex set of equations and can require large computational resources to calculate for large domains, several simplifications and methods exist. These stem from geometrical simplification methods in which flow in a cartesian direction can be ignored from the gradient operator as in the case of a two dimensional flow case, or by identifying points in which a flow is uniform in either direction such as over a symmetrical body with no incidence angle. The axisymmetric method is another manner in which the flow in the tangential direction of a body is uniform and the domain can be simplified as a infinitely thin sector around the axis of symmetry. Additionally methods such as the Euler simplification for adiabatic and inviscid flows can be used to neglect the density based terms in the navier stokes equations, thus removing the high order terms from the equation.

The turbulent fluctuations in a flow are also a major contributor to the overall computational cost of a calculation which can again be ignored for an inviscid case, adding some compensatory artificial viscosity in order to maintain stability, or modelled around a calculated mean flow based off predetermined data sets. This gives rise to three main sections within computational fluid dynamics, Direct Numerical Simulation (DNS) in which a fine grid is used and all scales of turbulence are directly resolved. Large Eddy Simulation, in which large length scales of eddies resolved and smaller scales are modelled or handled by a sub grid method. And finally the least computationally effective Reynolds Averaged Navier-Stokes method in which only the mean quantities are calculated and no turbulence is resolved, requiring the use a turbulence model to simulate the presence of turbulence.

Various turbulence models exist with specific benefits for different regimes including;

k-ε :

The k-ε model, solving for the turbulent kinetic energy and its dissipation rate, is a robust model developed on the mixing-length model and is predominantly used for external and aerodynamic flows, capable of being applied to problems including high Reynolds numbers. Being a two equation model it accounts for the dissipation of turbulence in addition to just the transport of turbulence, with good options for wall models making it suitable for wall bounded and shear flows but lacking in flows with adverse pressure gradients or large flow separation.

k-ω:

The k-ω model is another two equation model substituting the turbulent dissipation rate with the specific rate of dissipation of turbulence into heat. The k-ω model therefore has the advantages of better modelling of free inertial flows such as those with large flow separation or jets.

Spalart Allmaras:

The Spalart Allmaras model is another popular model however being a single equation model it is unable to account for the dissipation of turbulent energy and is only a transportive model. This does however come with the benefit of decreased computation and easier convergence.

Wall modelling:

In combination with a turbulence model, a wall model can also be applied to aid with the resolution of the shear flow within a surface boundary layer. Two main methods exist in wall modelling relating to the non dimensional height of the first cell from the wall.

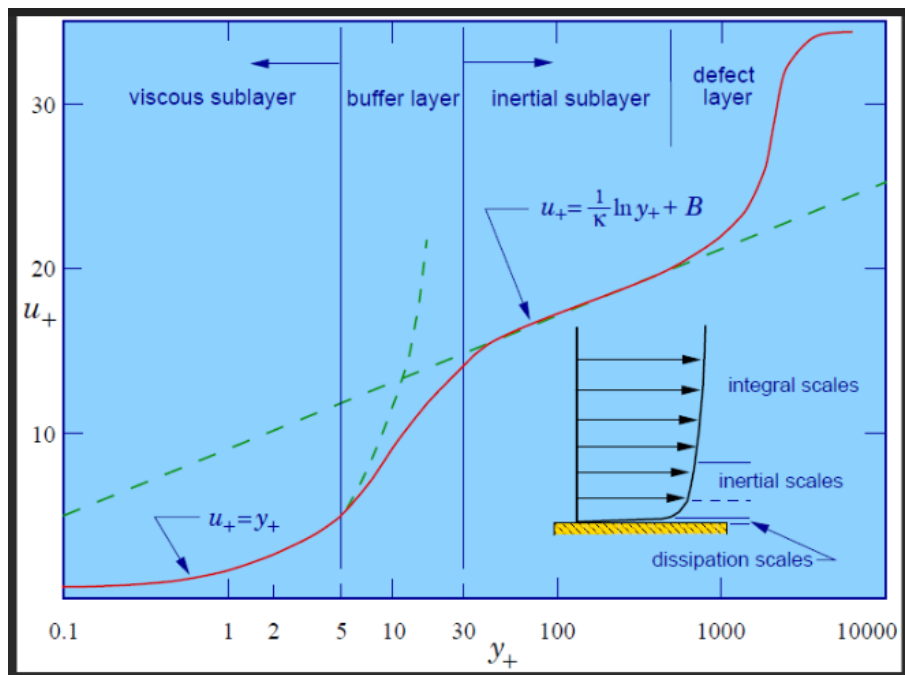


Figure 8 –  $U^+$  vs  $Y^+$  (starccm user manual)

*Figure 8*, shows the distribution of a turbulent boundary layer, in which the buffer viscous sublayer can be represented as a viscous sublayer and logarithmic inertial layer. The  $Y^+$  parameter represents the non dimensional distance perpendicular from the wall with the  $u^+$  non dimensional velocity of the layers. A high or low wall  $Y^+$  treatment can be chosen depending on if the shear layers perpendicular to the wall intend to be resolved or modelled. Placing a prismatic type layer mesher along the surface with the first cell within the viscous layer, maintaining a  $Y^+$  sub 5, ideally around 1, will lead to the velocity gradient perpendicular to the wall being resolved which brings a higher accuracy. Placing the first cell in the logarithmic layer, approximately  $30 < Y^+ < 300$ , will lead to the viscous layer being modelled by standard wall functions representing the distribution, which is a more computationally effective method. The wall distance for a desired  $Y^+$  can be calculated from the kinematic viscosity and friction velocity  $u_\tau$  by;

$$\Delta Y = \frac{Y^+ \nu}{u_\tau} \quad (\text{Eq. 21})$$

Where  $u_\tau$  is given in terms of the wall shear stress  $\tau_w$  and density;

$$u_\tau = \sqrt{\frac{\tau_w}{\rho}} \quad (\text{Eq. 22})$$

And the wall shear stress can be calculated from the free stream velocity and a coefficient of friction from methods suggested by (White, 2021);

$$\tau_w = \frac{1}{2} C_f \rho U^2, \quad C_f = 0.0577 Re^{-\frac{1}{5}} \quad (\text{Eq. 23})$$

# 3. Literature Review

## 3.1 Rocket Nose Cones (Paula)

Aerospace industry research on nose cones has shown to be one of the most important aspects of optimizing rocket aerodynamics. Three distinct types of drag are experienced by nose cones are: pressure drag, wave drag, and skin-friction. Skin drag, so named because it resembles the friction that occurs when two rubbing objects or substances come into contact with one another, is the outcome of air particles making contact with the surface of a moving body. Maintaining a smooth and clean body surface helps minimize drag, but it does not prevent the creation of a boundary layer there. Pressure drag is frequently referred to as form drag because it is a direct result of the body's shape and form as it creates turbulence that results high and low pressure leaving a wake behind the body (Braeunig, 2020). Wave drag, which arises from the formation of a shock wave, is the primary cause of total drag only at supersonic speeds. Like the pressure drag previously mentioned, this causes a rapid change in pressure, leaving high pressure pushing at the front of the body and creating a lot of pressure drag at the back.

During the 1950s, NASA conducted many physical experiments involving wind tunnels on nose-cylinder configurations to study wing-body drag at supersonic speeds. It was concluded that streamlined shapes reduced pressure drag at subsonic speeds but couldn't eliminate drag at supersonic speeds because there a large cancellation of drag existed when presented with a high fineness ratio, and to an extent, affected by the maximum diameter's position (Jones, 1956). The National Advisory Committee for Aerodynamics (NACA) confirmed this in 1949, concluding that higher fineness ratios were more efficient in reducing drag, particularly a 12.5:1 ratio (Hart & Katz, 1949).

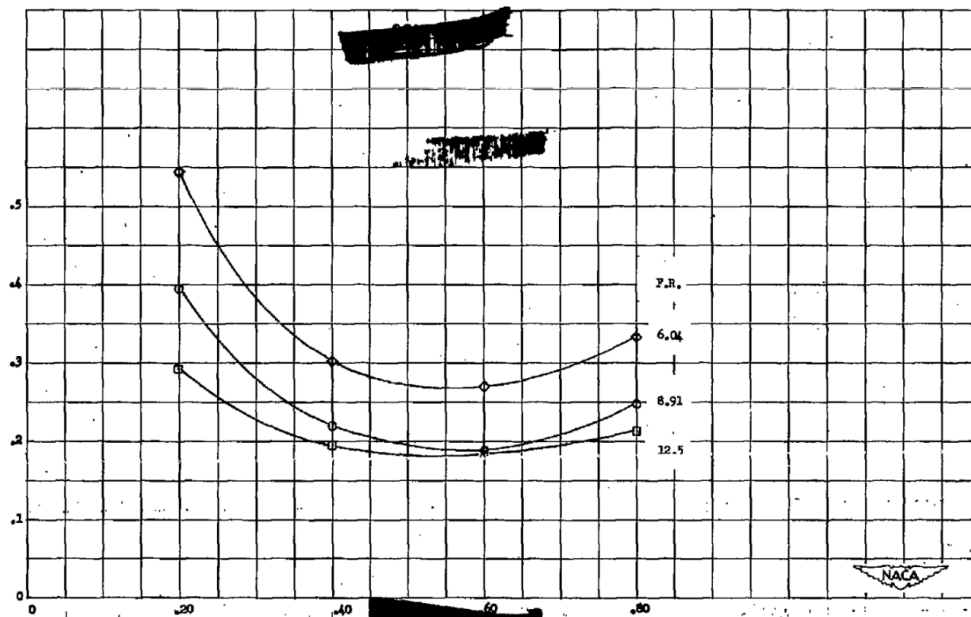


Figure 9: Drag coefficients against varying fineness ratios at Mach=1.55 (Hart & Katz, 1949)  
During the same period, notable researchers introduced innovative nose cone designs. Wolfgang Haack and William Sears developed the Sears-Haack conical body, later inspiring the Von Karman geometry.

NACA's 1949 experiments showed the influence of fins on drag. Nine years later, NACA compared fineness ratios of parabolic nose cones at various Mach numbers (see Figure 8). The Von Karman geometry correlated with the 1949 results, indicating lower drag for higher fineness ratios. However, it was found that ratios above 5 or 6 weren't significantly more efficient (Perkins, Jorgensen, & Sommer, 1958). Larger ratios would limit payload space unless the vehicle's size increased substantially. Thus, a 5:1 fineness ratio was deemed optimal for reducing aerodynamic drag while accommodating the necessary engine diameter.

In 1984, NACA conducted another study on the effect of bluntness in nosecone and its aerodynamic impact during flight, concluding that increased bluntness led to higher pressure at the tip (Nowak, Albertson, & Hunt, 1984). This conclusion was by another study by The National Advisory Committee further solidified the previous conclusion with their study that studied nose bluntness against different Mach numbers, maintaining a fixed 3:1 fineness ratio. Results showed that more blunt noses, like the power series  $\frac{1}{2}$  nose cone, performed the worst due to their high drag coefficients (Perkins, Jorgensen, & Sommer, 1958). The drag properties for different nose cone designs are compared on Figure 9, with the gaps representing the lack of research and information. The Von Karman and Power series  $\frac{1}{2}$  are thought to provide the best performance among the Mach numbers the I-class rocket will withstand, based on the data shown in the figure.

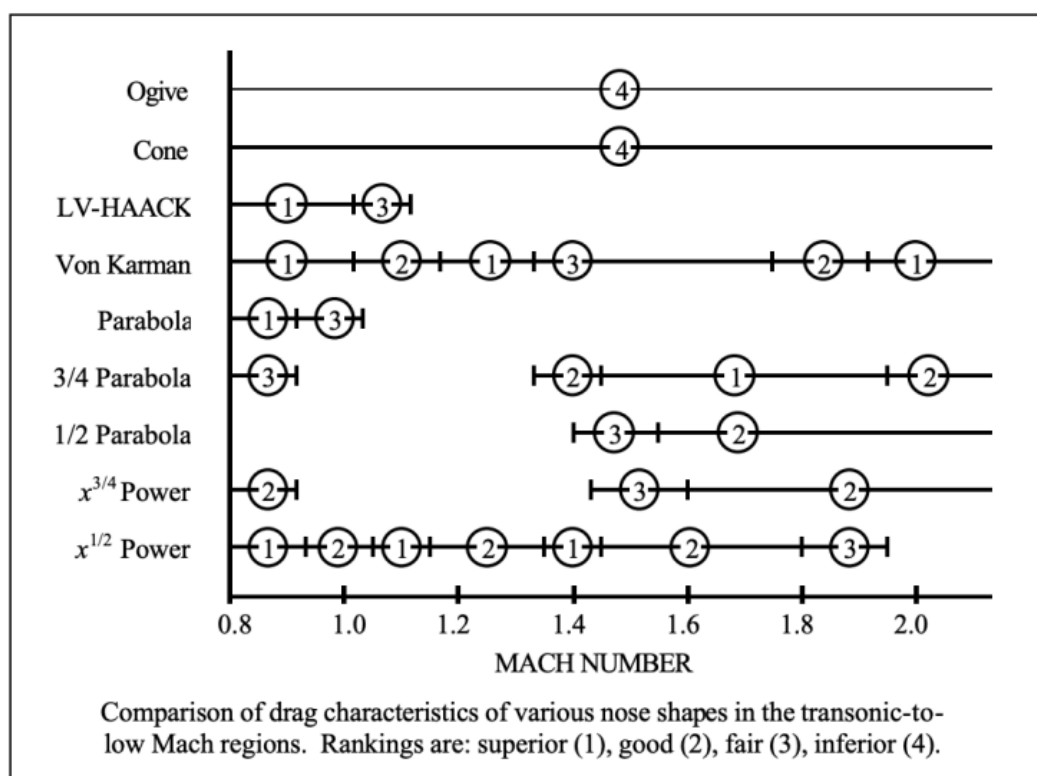


Figure 10 - Comparison of Drag characteristics on various nose cone shapes (Gary & Crowell, 1996)

## 3.2 Rocket Fins (Ruben)

Fins are critical for a rocket's stability and performance (Bunkling, 2022). They function as control surfaces, guiding the rocket in the desired direction and preventing uncontrolled spinning. Additionally, fins generate lift, similar to an airplane wing, allowing the rocket to reach higher altitudes.

There are six primary fin planforms: elliptical, clipped delta, swept, rectangular, tapered swept, and trapezoidal (Bunkling, 2022). Rectangular fins, as the name suggests, have a flat, rectangular surface. While both rectangular and swept fins share a similar shape, swept fins have a larger leading-edge sweep angle (Bunkling, 2022). This angled design improves aerodynamics by shifting the centre of pressure (CP) towards the aft of the rocket, away from the nose cone (J, 2014). The swept angle also reduces drag by minimizing the amount of air that flows around the fin without contacting it (Lucas, 2014).

In terms of stability, a model rocket is considered stable when its centre of gravity (CG) is positioned ahead of the centre of pressure (CP) (Milligan T. V., Model Rocket Stability, 2018). The greater the distance between these two points, the more stable the rocket. Ideally, this stability margin should fall between 1 and 2 calibres (fin lengths) (Milligan T. V., Model Rocket Stability, 2018). A stability margin less than 1 indicates an overly sensitive rocket, prone to wobbling. Conversely, a stability margin exceeding 2 can lead to an over stable rocket, making it difficult to control due to excessive course corrections.

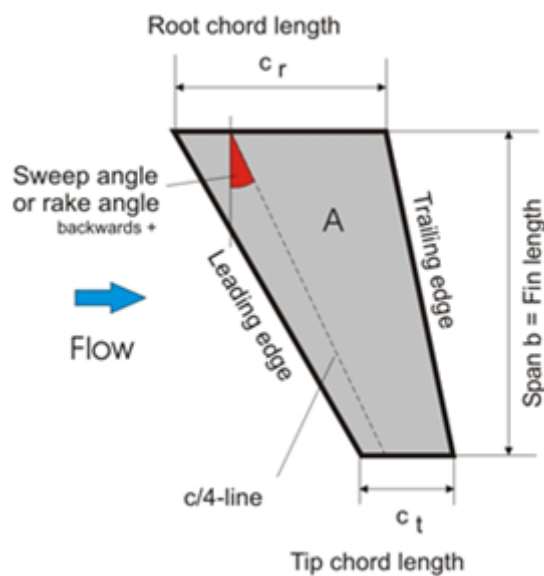


Figure II - Labelled tail fin (STAR, 2021)

The root chord length, which refers to the distance between the leading and trailing edges at the fin's base, significantly impacts the center of pressure (CP). Increasing the root chord length moves the CP forward, enhancing stability but also increasing drag. This drag can lead to reduced altitude and velocity. Similar effects are observed with fin span. Both root chord and span influence the overall fin area, consequently affecting the rocket's weight and center of mass.

On the other hand, the tip chord length, measured at the fin's tip, has an opposite effect. Decreasing the tip chord length also moves the CP forward, improving stability. However, it benefits performance by reducing drag, allowing the rocket to achieve greater altitude and velocity.

Finally, sweep angle, the angle at which the fins are positioned relative to the rocket body. A positive sweep angle, where the fins lean back, improves stability by concentrating aerodynamic forces on the leading edge and shifting the CP forward. However, similar to a larger root chord, a positive sweep angle can also increase drag, potentially hindering performance. The optimal sweep angle for a swept fin is shown between 20° and 45° (Minnesota & Stroick, 2011).

### **3.3 Rocket Engines (Ruben)**

The foundations of modern rocket propulsion were laid around World War II, with Germany pioneering its integration into long-range rockets (Heister S. D., Anderson, Pourpoint, Cassady, & Cassad, 2019). Propulsion is the mechanism that generates the thrust necessary for a rocket to overcome Earth's gravity. This thrust is achieved through a controlled combustion process. Rocket engines burn propellant and expel the hot gases at high velocity through a narrow nozzle at the base of the rocket. This rapid ejection of mass creates a forward thrust force, propelling the rocket skyward.

Rockets primarily use two distinct kinds of propulsion, solid propellant, and liquid fuel. Solid propellant contains a pre-mixed fuel and oxidizer that burns rapidly upon ignition. This burning generates hot gases that expel out of the engine nozzle at high speed, creating thrust. While easy to use, they offer less control over the engine's thrust and cannot be restarted once ignited. Liquid propellant engine store fuel and oxidizer separately and use pumps to inject them into a combustion chamber. There, they ignite and create hot exhaust that propels the rocket. This design allows for greater control over the engine's thrust. Unlike solid engines, liquids can be throttled making them ideal for larger, more intricate rockets. Since liquid engines can be complicated, this project will solely focus on solid propellant rockets.

A standard rocket is composed of distinct parts. The motor casing acts as a strong and secure container for the rocket propellant and other critical elements. It needs to withstand the high pressure and hot gases generated during engine combustion. A common motor casing will be made out of steel or wound glass fibre (Summerfield, 2013).

The propellant used in high powered rockets is a mixture of oxidizer like ammonium perchlorate that provides oxygen and a fuel like a high-performance polymer for combustion. Further additives are also used to influence burn rate and performance. In a high-powered rocket engine, the igniter is a crucial component responsible for initiating the combustion process of the solid propellant. The igniter generates an intense burst of flame that ignites the main propellant within the motor casing. This initiates the controlled burn that generates the thrust necessary for rocket flight. High-powered rocket igniters are typically electronically initiated. This offers greater control and reliability compared to simpler methods used in some model rockets. One of the electric components is a squib, this is a small pyrotechnic device that converts electrical energy into a high burst of heat which sets off the black powder charge in the igniter.

### **3.4 Recovery Systems (Ruben)**

A recovery system ensures that the rocket safely lands on the ground without the damage of any components. A well-designed recovery system facilitates the reuse of the rocket body and potentially some internal components after a successful launch. This reusability significantly reduces the operational cost of high-powered rockets as well as promotes environmental conscious practices. Over the years many recovery systems have been developed with the parachute being the most popular choice in High powered model rockets.

#### **3.4.1 Single Parachute recovery**

Parachute recovery is the most widely used system. It works by deploying a parachute after the rocket reaches apogee and therefore slowing the rocket's descent rate. It uses the force from the desired ejection charge to deploy the parachute out of the rocket's airframe.

#### **3.4.2 Multiple parachute (cluster) recovery**

This method uses multiple smaller parachutes instead of a singular larger one. Distributing the drag force over several parachutes can offer better stability and prevent oscillations during descent. This also reduces the stress on an individual parachute hence offering even slower descent.

#### **3.4.3 Glided recovery**

This approach utilizes wings or fins designed to generate lift, allowing the rocket to glide back to ground after launch. Offers more horizontal travel compared to a straight descent, allowing for a designated landing zone further from the launch site (Milligan T. V., The Different Rocket Recovery Techniques, 2017). The wings or fins create lift as the rocket descends, enabling a controlled glide path and

potentially extending flight time. However, this recovery system requires a more complicated aerodynamic design.

### **3.4.5 Streamer recovery**

A streamer recovery utilizes long, thin strips of material deployed after launch to create drag and slow the rocket's descent. Streamers are typically made of lightweight materials like nylon. They are cut into long strips and rolled or folded inside the recovery compartment. Similarly, to the parachute, it is deployed at apogee through the ejection charge. This is usually used in low powered and small rockets.

### **3.4.6 Helicopter recovery**

This method of recovery is similar to a parachute but deploys helicopter like blades instead. The blades are connected to the nose cone via a rubber band. When the nose cone is ejected the blades come out the body tube and rotate, producing lift resembling a helicopter (Milligan T. V., *The Different Rocket Recovery Techniques*, 2017).

### **3.4.7 Net recovery**

This approach is the simplest method and involves a recovery net that is deployed on the ground to catch the rocket. The net cushions the impact of the rocket and therefore not damaging any of its components. This is only suitable for very lightweight rockets because of the net's limited impact tolerance. In addition, this recovery system only works for low altitude rockets as it is easier to predict the landing area.

## **3.5 Expected Flight Envelope & OpenRocket (Ruben)**

To justify the rocket design, a predicted maximum altitude model must be used to show the rocket will reach and exceed the I class record stated in the first section. In this report the prediction model used will be OpenRocket.

OpenRocket is a software done as part of a thesis by Sampo Niskanen in 2013. OpenRocket boasts a library of pre-defined components alongside the ability to create custom shapes, facilitating rapid design exploration and performance analysis. Sophisticated algorithms assess the rocket's aerodynamics, predicting factors like drag, stability, and centre of pressure. Furthermore, a powerful flight simulator estimates the rocket's trajectory, apogee, and other performance metrics based on motor selection and launch conditions.

### 3.5.1 Drag equations from OpenRocket

OpenRocket calculates Nose pressure drag through these equations:

At transonic and supersonic speeds, (Niskanen, 2013) combines Hoerner's half apex-angle equation and experimental data to give these two equations.

$$(C_d)_{cone} = \frac{2.1}{1+f_n^2} + \frac{0.5}{\sqrt{(4f_n^2+1)(M^2-1)}} \quad (Eq. 24)$$

$$(C_d)_{nose} = [0.72 \times (k - 0.5)]^2 + 0.82] \times C_{d_{Cone}} \quad (Eq. 25)$$

OpenRocket calculates fin pressure drag through these equations:

The first equation calculates the pressure drag coefficient for a leading-edge rounded fin (Niskanen, 2013)

$$(C_d)_{LE} = 1.213 - \frac{0.0502}{M^2} + \frac{0.1095}{M^2} \quad (Eq. 26)$$

$$(C_d)_{fin} = [C_{d_{LE}} + C_{d_{TE}}] \times \cos^2 \theta_{LE} \quad (Eq. 27)$$

OpenRocket calculates skin drag through these equations:

The prediction of skin friction remains a challenge due to limitations in our understanding of the transition process between laminar and turbulent flow regimes, as acknowledge by Nielsen. Therefore, all calculations for skin friction assume turbulent boundary layer.

$$C_f = \frac{1}{1.50 \ln R - 5.6^2} \quad (Eq. 28)$$

Compressible corrections (Niskanen, 2013):

$$c_{fc} = C_f(1 - 0.1M^2) \quad (Eq. 29)$$

$$(C_d)_{friction} = c_f \frac{\left(1 + \frac{1}{2f_b}\right) \times A_{wet,body} + \left(1 + \frac{2t}{c}\right) \times A_{wet,fins}}{A_{ref}} \quad (Eq. 30)$$

### 3.5.2 OpenRocket Validation

The accuracy of OpenRocket's simulations has been validated through comparisons with real-world data. Technical documentation highlights that key aerodynamic parameters like centre of pressure location and drag coefficient are simulated with an accuracy of around 10% at subsonic speeds (Niskanen, 2013). This accuracy is comparable to established commercial software like RockSim. Furthermore, the document suggests that this reasonable level of accuracy extends up to Mach 1.5 (Niskanen, 2013). This makes this software tool adequate for predicting the performance of our proposed rocket model.

### 3.5.3 OpenRocket flight simulations for proposed model

OpenRocket's flight simulations consider both atmospheric properties and roll dynamics to achieve a comprehensive performance prediction. User-defined atmospheric profiles or standard models account for air density variations with altitude, impacting drag and influencing the trajectory and apogee (maximum height). Similarly, wind speed and direction can be specified, enabling simulation of wind shear's effect on the rocket's course.

*Table 2: Simulation parameters*

Average windspeed (m/s)	2
Standard deviation (m/s)	0.2
Turbulence intensity (%)	10
Wind direction (°)	90
Launch rod length (mm)	1000
Launch rod Angle (°)	0
Atmospheric temperature (C°)	15
Atmospheric pressure (mbar)	3

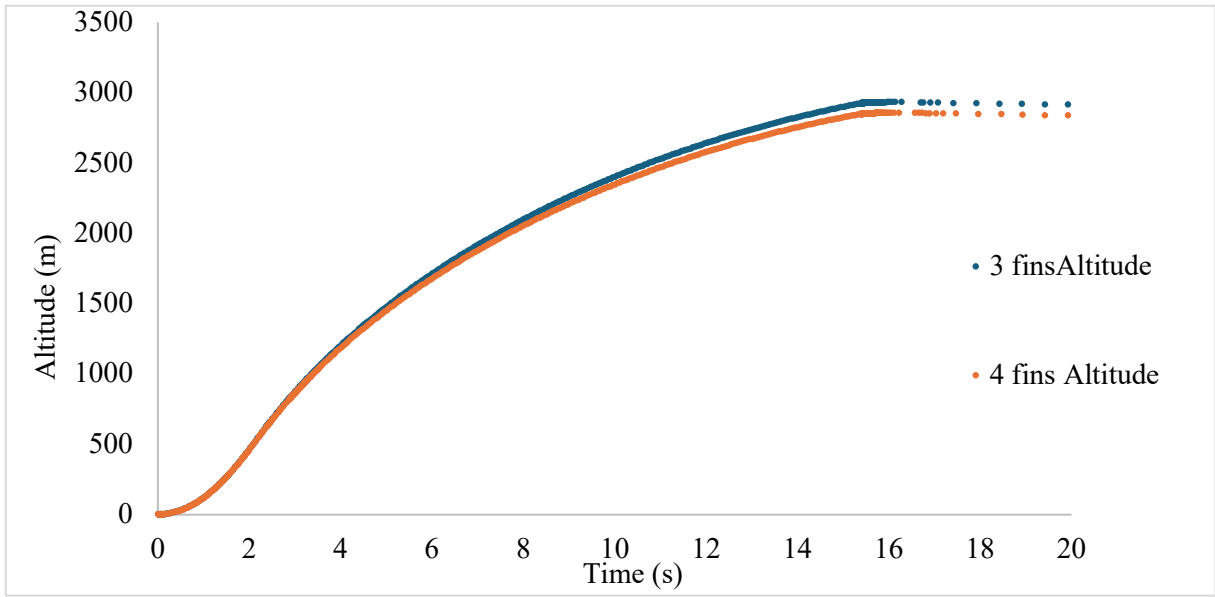


Figure 12 - Altitude against time until apogee (Pro38 I350-16A engine)

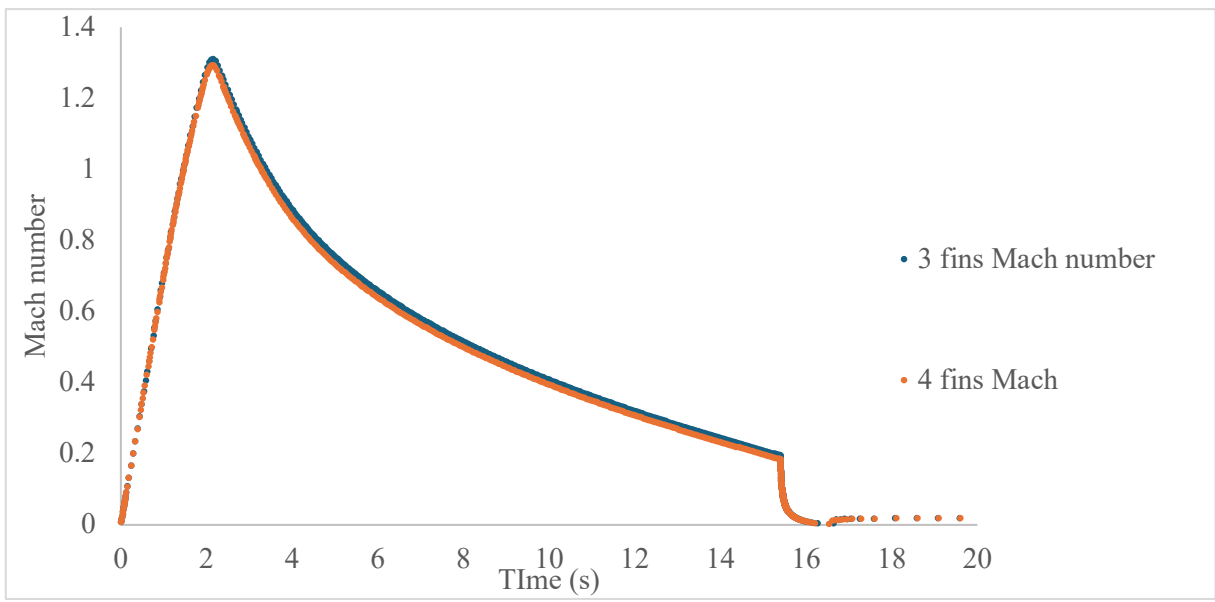


Figure 13 - Mach number against time until apogee (Pro38 I350-16A engine)

The Figure (13) represents the Mach number of the rocket relative to time. From the graph it is evident the rocket accelerates for about 2.5 seconds reaching a maximum Mach number of about 1.32 for 3 fins and about 1.3 for 3 fins. Proceeding this, the rocket starts to decelerate until it reaches apogee at 18.44 seconds for both fins. Figure (14) shows the graph of altitude against time. From the graph, altitude steadily increases until it reaches a maximum altitude of about 2870 m for 3 fins and just under 2850 for 4 fins.

## 4. Research and Design

### 4.1 Nose Cone (Paula)

A good chosen nose cone will allow the optimisation of the aerodynamics of the I-class rocket intended for reaching a 3km apogee while ensuring reusability. The Von Karman nose cone design was chosen after careful consideration for the reason stated in the literature review, including drag reduction, pressure distribution, and payload capacity.

The process of designing the nose cone for the project included adjustments to achieve a 5:1 length to diameter ratio to adjust it to the desired diameter – in order to fit the I-class engine – and make sure the length was compatible with the aluminium body. Rooted in the pioneer designs by Ludwig Prandtl and Theodore Von Karman, this section assesses some analyses of aerodynamic principles and experimental data from NASA and NACA.

Through analysis of the effects of nose bluntness, fineness ratio, and geometric parameters, the Von Karman nose cone was found to be a viable option with good subsonic, transonic, and supersonic performance characteristics. Beginning with the importation of the Von Karman coordinates tailored to the desired external diameter into SolidWorks, the design was adjusted and redesigned until arriving at the final proposed design.

#### 3.1.1 SolidWorks Nose Cone model

The conclusion that could be taken from the nose cone literature review, it is evident that nearly all research papers agree that no single geometry is solely responsible for a rocket's best performance at subsonic, transonic, and supersonic speeds and that the geometry that needs to be selected must be customised to the vehicle's intended purpose or apogee.

Taking into account the aims of this project (to reach 3km apogee) the Von Karman nose cone was chosen because it was the geometry that most aligned with them.

*Equation 31* was derived by Theodore Von Karman to design an innovative geometry that would then give rise to the Von Karman Nose Cone discussed in the literature review.

$$y(\theta, C) = \frac{R}{\sqrt{\pi}} \sqrt{\theta - \frac{1}{2} \sin(2\phi) + C \sin^3(\phi)} \quad (\text{Eq. 31})$$

Where

$$\theta(x) = \cos^{-1} \left( 1 - \frac{2x}{L} \right) \quad (\text{Eq. 32})$$

Where the target parameter – in this case an internal diameter of 41mm – needs to be optimised to determine the value of C; for the Von Karman geometry with fineness ratio this parameter is taken as zero (Gary & Crowell, 1996).

Based on the diameter required to fit the engine and payload inside the body, the nose cone's length was then calculated using the equations. Various numbers of x were input, in increments of 5, into the following equation in order to get corresponding y values and therefore attain coordinates for Van Karman to plot. The following is an example calculation for an x coordinate with a value of 5.

$$y = \frac{22.15}{\sqrt{\pi}} \sqrt{\cos^{-1}\left(1 - \frac{2 \cdot 5}{115}\right) - \frac{1}{2} \sin\left(2\left(\cos^{-1}\left(1 - \frac{2 \cdot 5}{115}\right)\right)\right)} = 1.673$$

This equation was used to import the Von Karman coordinates into SolidWorks as a curve through XYZ coordinates. The curve was converted into an entity and the sketch portrayed on *Figure 13* was revolved by 360°.

The Nose cone on SolidWorks was made of a total length of 175mm: 115mm for the primary nose section and an additional 60mm with a reduced diameter intended for insertion into the aluminium tube.

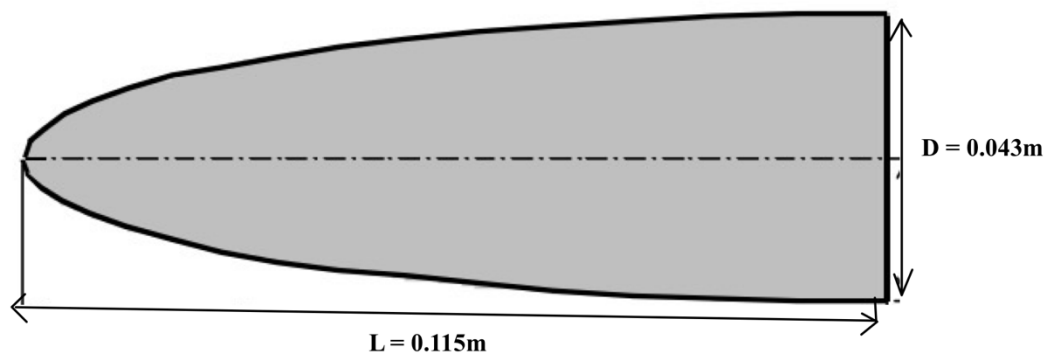


*Figure 14 - Von Karman geometry for fineness ratio 5:1 for a needed diameter of 0.043m*

The Nose cone on SolidWorks was made of a total length of 115mm: 115mm for the primary nose section and an additional 60mm with a reduced diameter intended for insertion into the aluminium tube.

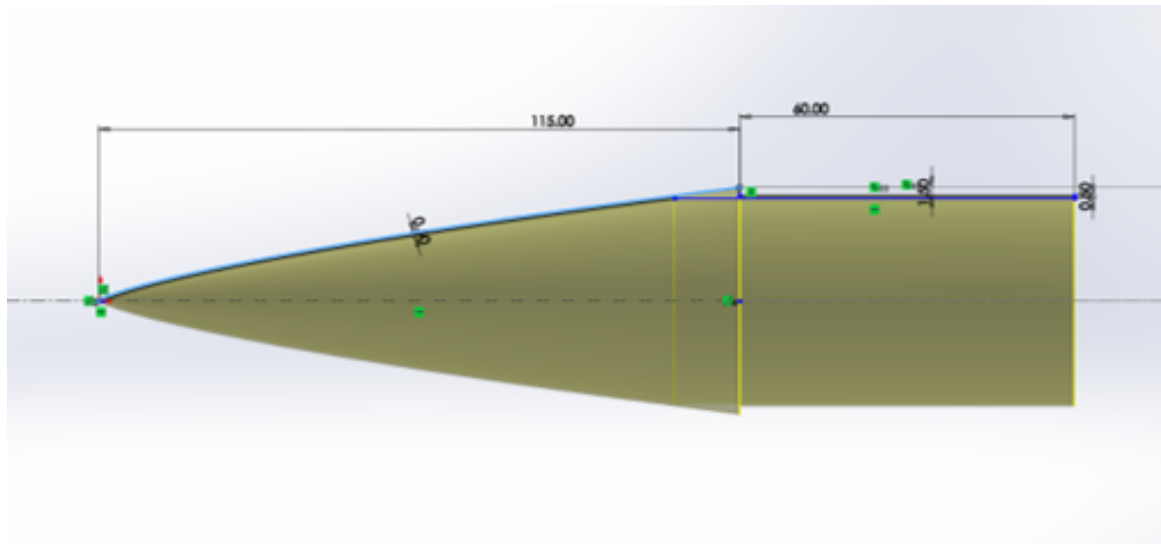


Figure 15 - SolidWorks nose cone sketch

The final design can be seen on *Figure 16* featuring holes around the circumference to accommodate small screws if they had been necessary to secure the nose cone to the aluminium tube.

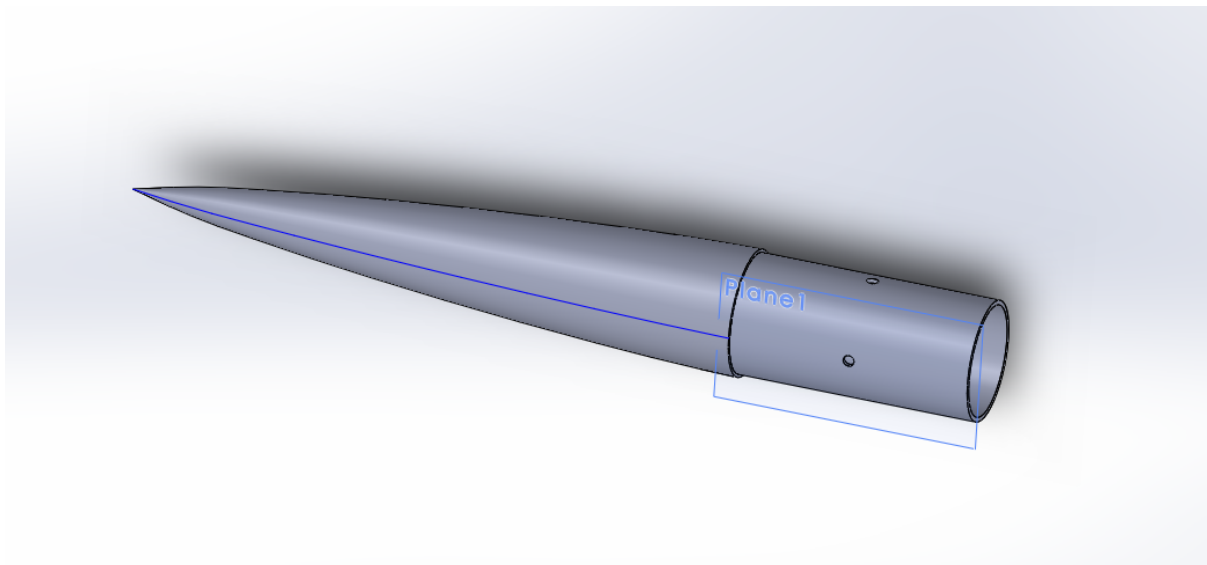


Figure 16 - Final SolidWorks nose cone component

## 4.2 Fins (Paula)

A well-chosen fin shape and fin count is crucial for the optimisation of the aerodynamics of the I-class rocket intended for reaching a 3km apogee while ensuring reusability. The shape of the fins was chosen in order to stabilise the rockets' trajectory and minimise its spinning during flight. As mentioned in the literature review, a rectangular fin was chosen due to its sweep angle at the leading edge, allowing less air to travel around the fin therefore lowering the centre of pressure towards the end of the rocket away

from the nose cone (Lucas, 2014). The final chosen shape for the fin with its final dimensions is portrayed on *Figure 11*; with a root chord of 45.1mm, a tip chord of 19.1mm, a height of 43mm and a sweep angle of  $40^\circ$ , giving the rocket a stability margin of 1.3.

Once the fin profile fin was decided, the shape of the airfoil had to be considered. Most model rockets are made with square tapered fins, however significant improvements can be done just by using an airfoil that will decrease fin mass, decrease the drag and reduce longitudinal moment of inertia of the rocket (Milligan T. V., 2012). After considering the requirements of the rocket, a NACA0008 was chosen for its symmetry and low-thickness profile. Due to its symmetry, the NACA0008 ensures consistent lift and stability, even when encountering unexpected shifts in angle of attack and will perform the best at a transonic range (Milligan T. V., 2012). When these shifts in angle of attack occur, the chosen airfoil responds by producing lift, enhancing the stability of the rocket during ascent hence maintaining its desired flight path. Moreover, the NACA0008 has a straightforward design that would make production easier, facilitating cheaper and more efficient manufacturing process.

The NACA0008 airfoil, tailored for optimal performance at low Reynolds numbers, was not deemed the only suitable choice, but was the perfect option for this project to design and manufacture an I-class rocket, due to its simplicity, stability and manufacturing costs.

### **3.2.1 SolidWorks fin mounts designs**

The process of designing the fins for the project started by sketching the side view of the fins with the parameters mentioned before (refer to *Figure 17*). The external diameter of the fin mount bodies was designed to match that of the aluminium body tube, ensuring a seamless fit. The body was engineered with a thickness that would be able to withstand the forces that the rocket would experience during flight and still leave enough space for the engine and any adhesive it required. Additionally, a section of length 100mm with a reduced external diameter was extruded intended for insertion into the aluminium tube to facilitate a 'tight fit' attachment.

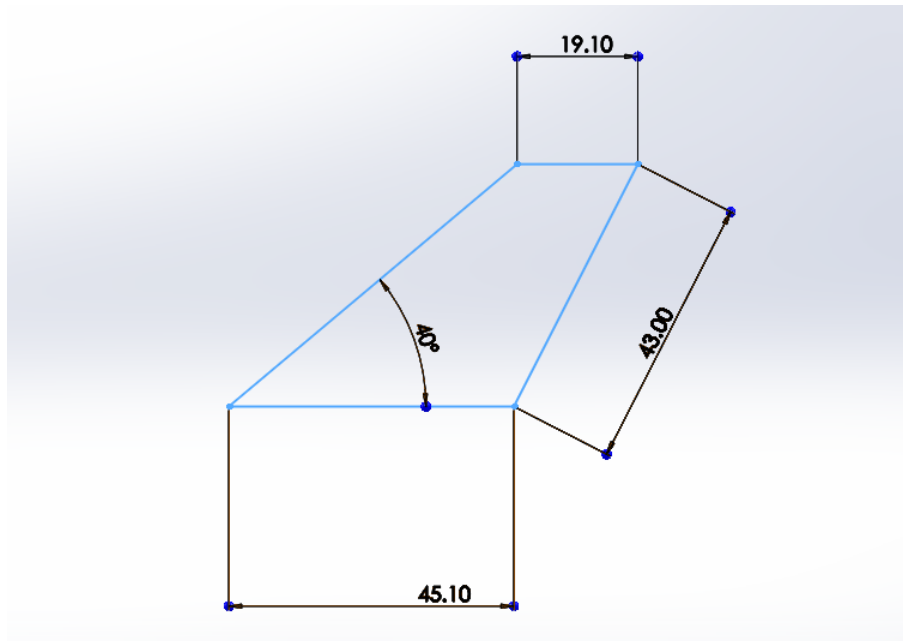


Figure 17 - SolidWorks initial sketch of the fins' planform area

The following design steps included importing NACA0008 coordinates for a root chord of 45.1mm, a tip chord of 19.1mm, and a height of 43mm (NACA 0008, 2024) into SolidWorks (refer to *Figure 19*). The following design steps included importing NACA0008 coordinates for a root chord of 45.1mm, a tip chord of 19.1mm, and a height of 43mm (NACA 0008, 2024) into SolidWorks (refer to *Figure 18*).

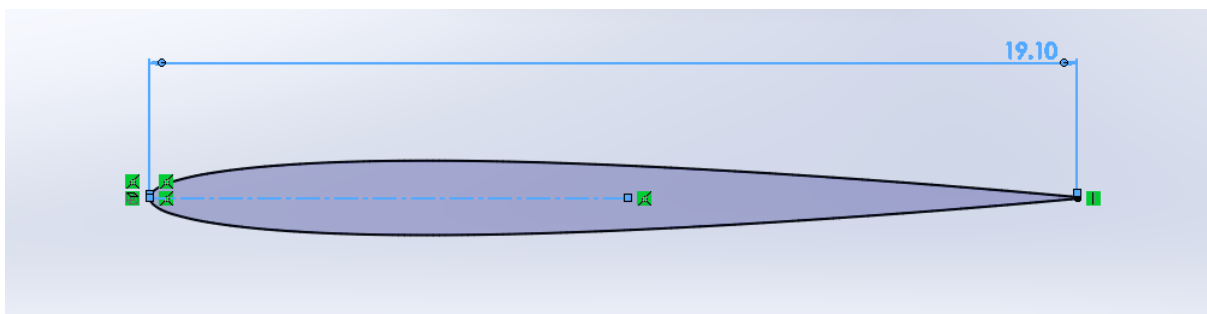


Figure 18 - Airfoil sketch of the NACA0008 with a chord of 19.1mm (fin tip)

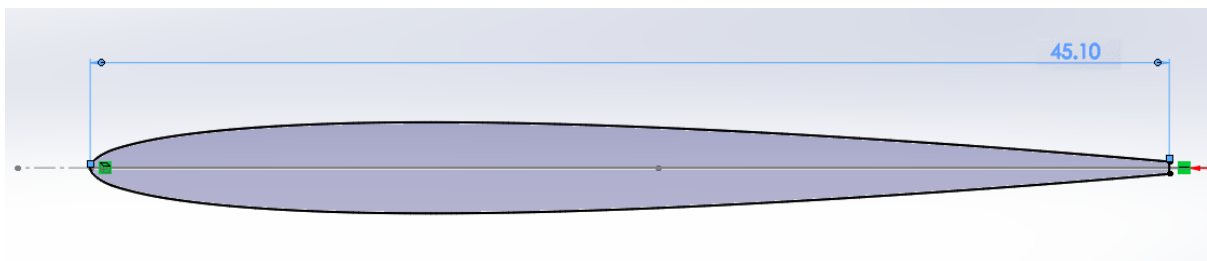
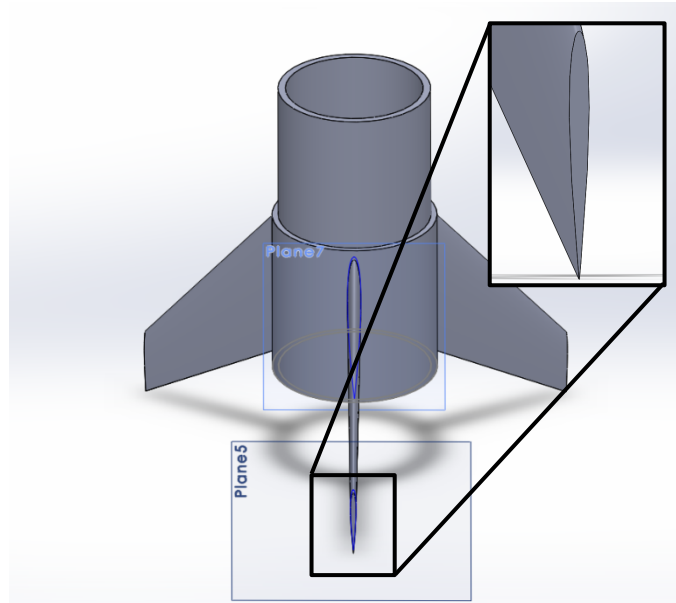
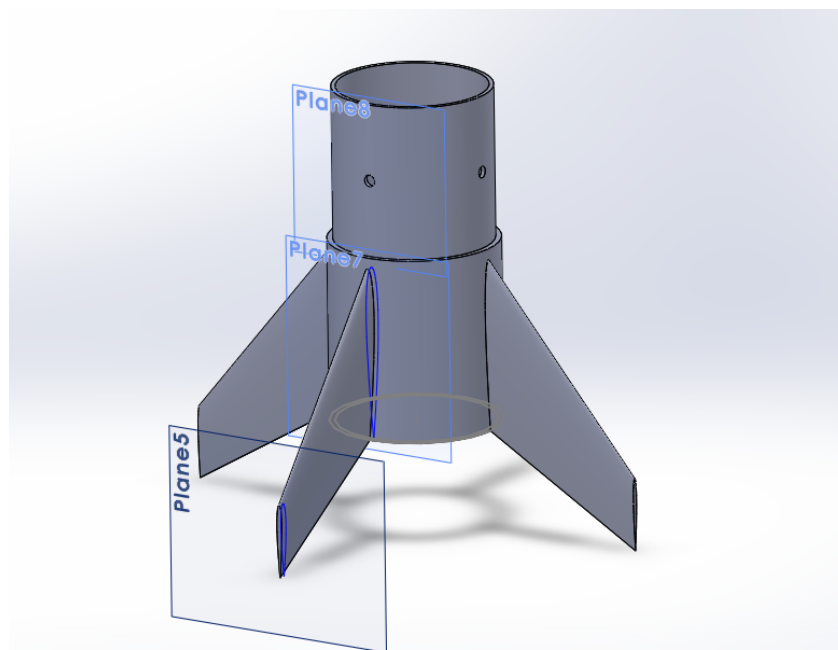


Figure 19 - Airfoil sketch of the NACA0008 with a chord of 45.1mm (fin base)

The final steps were to assemble the parts. The final designs for the 3-fin mount and the 4-fin mount designs can be seen on *Figures 20 and 21* respectively. Where the perforations seen on the 4-fin mount are to accommodate small screws should they had been necessary to secure the mounts to the aluminium body.



*Figure 20 - Final design for the 3-fin configuration - later used in wind tunnel testing - with an aerofoil close up*



*Figure 21 - Final design for the 4-fin configuration also used later in wind tunnel testing.*

### 4.3 Proposed final Rocket Design (Ruben)

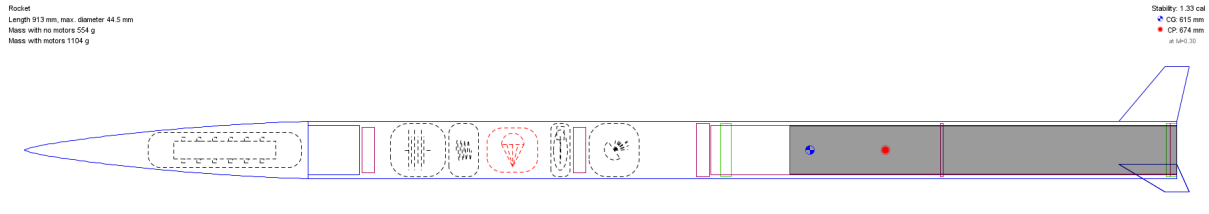


Figure 22 - OpenRocket schematic of proposed 3 fins design

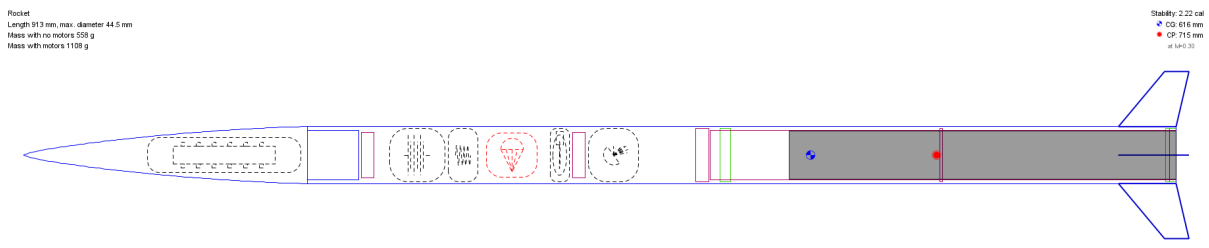


Figure 23 - OpenRocket schematic of proposed 4 fins design

Figure 22 and 23 shows the proposed 3 fins and 4 fins rocket design with all its components. This design uses the same nose cone as described in 4.1 as well as the fin design in section 4.2. To connect these two components, a fibre class rocket tubing was selected. These three components shall have the same diameter as the one used in the low-speed wind tunnel. The engine casing is shown by the grey section of the figures and is held by a motor mount. The following components are co2 deployment charge, recovery wadding, parachute and a battery connected to the flight computer.

### 4.4 Proposed final components (Ruben)

#### 4.4.1 Material comparison

Table 3 - Material comparison (MatWeb, 2024)

Properties	Aluminium 2024-T6	E-Glass Fiber, Generic	Kevlar - 29	Epoxy/Carbon Fiber Composite	ABS
Density (g/cc)	2.78	2.54	1.44	1.41	1.07
Tensile strength, Ultimate (MPa)	476	3450	2920	1010	38.4
Tensile strength, Yield (MPa)	393	3445	2758	1230	44.7
Elongation at Break (%)	5	4.8	3.6	1.52	14.4
Shear modulus (GPa)	27	30	70.3	4.12	87.5

<b>Shear Strength (MPa)</b>	283	50	9.2	86.7	N/a
<b>Modulus of Elasticity (GPa)</b>	72.4	72.4	70.3	99.9	2.04
<b>Electrical Resistivity (ohm-cm)</b>	4.49e-006	4.02e-006	1.0e-0014	1.0e-0014	7.26-e-15
<b>Specific Heat Capacity (J/g-°C)</b>	0.875	0.810	1.42	1.13	1.99
<b>Thermal Conductivity (W/m-K)</b>	151	1.30	0.04	78.8	0.171
<b>Melting Point (°C)</b>	502 - 638	1725+	800-900	1927+	100
<b>Cost (USD/Kg)</b>	2-3	2-3	7-27	13-53	Unknown
<b>Ease Of Fabrication</b>	Good	Good	Good	Difficult	Very Good

Carbon fibre composite provides several properties that make it in theory, the best material for both the body tube and fins of a rocket. Its high tensile strength compared to its low density means that it can be lightweight whilst withstanding significant forces during launch and flight. However, carbon fibre was not the material of choice as it is significantly more expensive than the other choice. In addition, carbon fibre requires more complicated manufacturing techniques which are not available. On the other hand, the fins are simple to manufacture with the 3D printer using carbon fibre nylon. Given the limitations of carbon fibre, fiberglass becomes the second-best option for both the body tube. Fibre glass also offers a high strength to weight ratio adequate for the mission profile. Furthermore, fibre glass tubes can be commercially bought with the desired dimensions at a more reasonable cost than carbon fibre. For the nose cone, ABS was the material of choice. This is because the nose cone design is complicated and unique and therefore cannot be commercially bought at the desired dimensions. A nose cone made from ABS can be 3d printed making readily available and convenient. While not as strong as fiberglass or carbon fibre, ABS still offers a high tensile strength to density ratio.

#### 4.4.2 Avionics

*Table 4 - Avionics comparison*

<b>Category</b>	<b>TeleMetrum Flight computer (Garbee, Packard, Finch, &amp; Towns, 2016)</b>	<b>CATS Vega (CATS, 2024)</b>
<b>Microcontroller</b>	Not specified	STM32F411
<b>Flash Memory</b>	2 MB	16MB
<b>Sensors</b>	IMU, Barometer, MPU6000	IMU, Barometer, GNSS
<b>Telemetry</b>	Beeps protocol	2.4GHz ISM Radio, Up to 1W
<b>Radio Range</b>	20Km	10km
<b>Power Consumption</b>	150 mA	100mA
<b>Size</b>	70 x 27 x 16 mm	100 x 33 x 21 mm
<b>Weight</b>	20 g	25 g

<b>Additional Features</b>	Dual Deploy Launch Trigger	2 Pyro Channels, 2 Servo Channels
----------------------------	----------------------------	-----------------------------------

*Table 4* compared 2 commercially used flight computers, the TeleMetrum and the CATS Vega. The microcontroller for the TeleMetrum is not specified in the specification's handbook. This makes it difficult to compare processing power. For that reason, we can assume the CATS Vega likely has more processing power due to its much high memory capacity of 16Mb. Both offer telemetry, but TeleMetrum Flight Computer uses the Beeps protocol, while CATS Vega uses a 2.4GHz ISM radio. While the Telemetry Flight Computer boasts a longer 20 km range, the specific protocol might limit real-world performance compared to the CATS Vega's established radio technology. Telemetrum Flight Computer uses slightly more power (150mA) compared to the CATS Vega (100mA) this is important to established which battery is needed. In terms of size and weight, the TeleMetrum is the best choice as it is both lighter (by 5g) and it is noticeable smaller in dimensions. In addition, Telemetry Flight Computer offers a dual deploy launch trigger, while the CATS Vega offers dedicated channels for controlling servos and pyrotechnics.

The Telemetrum flight computer was chosen for the proposed rocket design. For our mission, we only desire basic data collection like altitude and Mach number. Therefore, the more complex processing from the CATS Vega will not be fully utilised. We will also be using a simple deployment system and so there is no need for the complex deployment or servo control which The CATS provides. In addition, the smaller size of the Telemetrum is ideal in order to fit in our compact and lightweight rocket.

#### **4.4.3 Recovery**

Section 3.4 states multiple recovery systems. For the proposed design, the parachute remains the optimal choice. The proposed parachute is a round 24-inch radius parachute made from Nylon ripstop. This parachute more than strong to withstand the force of the rocket once deployed. Furthermore, it gives a descent velocity of 5.18 m/s which is within safety regulations.

A co2 ejection system was decided to accompany this recovery system, specifically the peregrine system. Compared to black powder ejection systems, CO2 offers a cleaner and more user-friendly solution. There is no residue left behind in the rocket compartment, simplifying post-flight cleaning and maintenance. Black powder performance can deteriorate at high altitudes due to reduced atmospheric pressure. CO2, being a gas, is not affected by altitude (Settlemyer & Motter, 2022). The peregrine system is particularly advantageous due to its compact size (4.5 inches). The peregrine also allows for double redundancy by mounting two units side-by-side on a standard 4" AV-Bay cap (tinderocketry, n.d.).

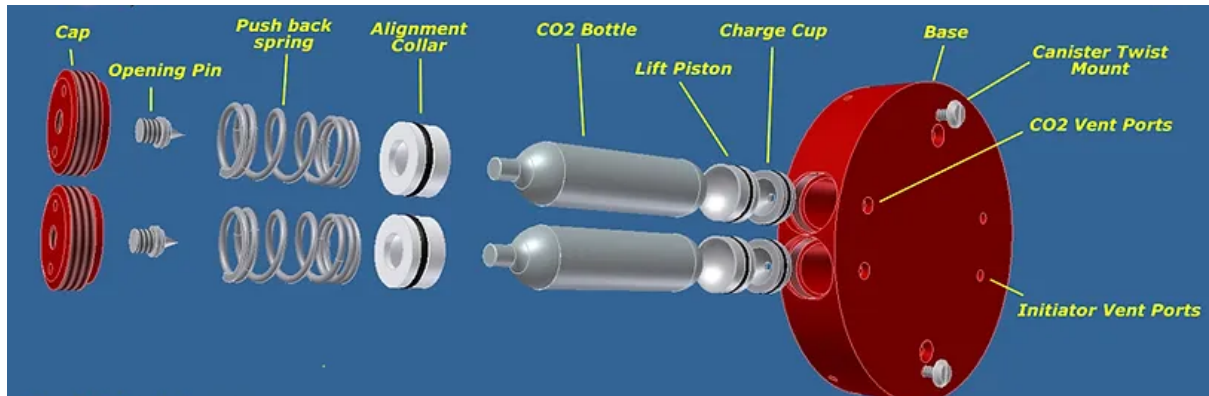


Figure 24 - Peregrine co2 system (tinderocketry, n.d.)

The ejection system relies on the flight computer's altimeter. The altimeter senses the rocket reaching apogee. Upon reaching this point, the flight computer sends an electrical signal through an electric match to the systems initiator. The initiator is a small pyrotechnic device that holds a small amount of black powder. When it receives the signal it fires, this fire creates a hot spot that punctures the co2 canister and releases the pressurised gas.

The parachute is connected to both the nose cone and the body tube via a shock cord and an eyebolt. When the ejection system goes off, the nose cone screws are designed to break allowing for the nose cone to be pushed off. When the parachute is airstream. The air flowing past the parachute fills the canopy, creating drag that slows the rocket's descent for a safe and controlled landing. The shock chord will have to withstand the high force of the parachute when its initially deployed, so a Kevlar shock chord was chosen.

#### 4.4.4 List of components

Table 5 - Components cost and supplier table

Component	Projected cost (£)	Supplier
Engine	~150	Unknown
Pro38 casing	81.77	Euro Space Technology EU
Peregrine co2 system	193.00	Apogee components
Parachute	73.66	Rocketman Parachutes
Shock cord	19.34	Blackcat Rocketry
Flight computer	307.09	Apogee components
Battery	14.75	cpc farnell
Fibre glass tube	17.36	Carbon Fibre Profiles

Miscellaneous (Eye bolt, wadding, wires, etc)	~30	Amazon
---	-----	--------

The motor casing chosen was a 5-grain casing. This was chosen as it is powerful enough to reach out desired apogee without compromising space for the avionics and recovery system. The eyebolt chosen is made of steel in order to make sure that it withholds the force of the shock chord. A 3.7v+ LiPo battery is needed to charge the TeleMetrum flight computer. Wadding is used to protect the parachute from ignition. The parachute is Made from .66oz Nylon Ripstop. It has a packing volume of 1.375” diameter x 1.569” length = 2.331”<sup>3</sup> with a weight of 198 grams. The fibre glass tube chosen has an internal diameter of ~40mm. This is wide enough to fit the engine casing and all the rest of the components.

## 4.5 Propulsion specifications (Ruben)

### 4.5.1 Regulations

As stated previously, this rocket is categorized as a small high-Power rocket. Following the UKRA regulations, it is required to have a certification to fly and is strongly recommended to be flown with a UKRA affiliated club. It is required to have a level 1 certification for rocket motors through impulse class of H to I. Furthermore, Level 1 certification requires a successful test flight performed before a UKRA certified safety officer.

### 4.5.2 Suppliers & Proposition

To adhere to the UKRA regulations the team has joined the East Anglia Rocketry Society (EARS). This was done by joining the British Model Flying Association and then applying for the EARS. By being a member of the society, it is possible to launch a I class rocket with the society. The society has a launch event every month. In this launch event, there is a list of engine suppliers that will deliver our requested engine to the launch site. Therefore, no need for storing explosives is needed at the university. To reach our apogee, we need to request an I class engine with an impulse of 350 Ns or higher and a burn out time of 16 seconds.

## **5. Experimental Testing (Ardrit & Paula)**

### **5.1 Introduction**

This section presents a comparative study aimed to investigate the aerodynamic performance of the model rocket with different fin configurations through low-speed wind tunnel testing.

The primary objective for the low-speed wind tunnel experiment was to test and compare a 3-fin and a 4-fin mount on the model rocket by transitioning between the two and determining which one provided the most stability and efficiency, aligning with the broader aim of this technical report of designing and manufacturing a reusable rocket capable of reaching an apogee of 3km. The associated aerodynamics forces and coefficients were then carefully analysed. This section attempts to evaluate the impact of fin count change on the rockets aerodynamic behaviour by extracting the forces in the X, Y, and Z directions as well as determining coefficients of drag and lift. Furthermore, statistical analysis and visualisation methods were used to identify noteworthy variations among the configurations, enabling well-informed conclusions concerning the best fin arrangements for this project. Through this comparative study using wind tunnel testing, valuable insights into the relationship between fin count and resulting aerodynamic forces, contributing to advancements in rocket design and engineering. Additionally, the primary objective for the high speed wind tunnel testing cone to identify the pressure distribution of the airflow surrounding it and assess its aerodynamic properties.

### **5.2 Low Speed Experimental testing (Paula)**

A slightly smaller model of the final design was created in order to be tested in the slow speed wind tunnel. The nose cone and fin mount were manufactured with aluminium whilst the actual fins were printed with ASA material. The nose cone and fins followed the design described in the previous section: Von Karman nose cone and swept back fins with a NACA0008 airfoil. Even though swept wings have proven to be the optimal option for rockets flying at supersonic speeds, because the rocket model inside the wind tunnel wont experience these speeds, we could say that the swept fin design chosen would be purely for aesthetic reasons – as well as part of the projects final rocket design – and exclusively to test the fin configuration, as it does not prove better or worse than a clipped-delta at subsonic speeds (Cruchet-Pasos, 2023).

#### **5.2.1 Apparatus**

The Queen Mary University of London's closed-circuit subsonic wind tunnel was used for the experiment. The working part of the wind tunnel measures 1.2x the width, 1.0x the height, and 2.4x the length, with a contraction ratio of 7.2/1. The airspeed in the wind tunnel can reach up to 40 meters per

second. The data and variation of the X, Y, and Z forces and moments were collected using Gamma ATI Model 6-component balance with computerised data capture. The sampling rate was set at 1000 samples per second and the wind-tunnel speed controller was attached to a Betz manometer and an inclined manometer, which were used to adjust the velocity to the required value.

Table 6 - Uncertainties of the apparatus

Parameter	Uncertainty
Betz Manometer	$\pm 0.1 \text{ mmH}_2\text{O} = \pm 1 \text{ Pa}$
Inclined Manometer	$\pm 0.5 \text{ mmH}_2\text{O} = \pm 4.9 \text{ Pa}$
Tunnel working section	$1.03 \times \Delta P$

Table 7 - Resolutions for each component of the six-component balance

$F_x$	$F_y$	$F_z$	$T_x$	$T_y$	$T_z$
1/40N	1/40N	1/20N	1/800Nm	1/800Nm	1/800Nm

### 5.2.2 Six-component balance

The 6-component balance receives its name from the fact that its capable of measuring six different components of force and moments acting on a body. Its sophisticated balance measures components that consist of the moments about each of the forces in three orthogonal directions – usually denoted by the letters X, Y, and Z – and the three axes: roll, pitch and yaw. This measurement ability enables thorough examination of the aerodynamic forces and moments acting on a body, therefore is a vital tool in aerospace engineering.

The 6-component balance's working principle is based on its capacity to convert mechanical moments and forces operating on the rocket model into electrical signals, which are subsequently recorded and processed for study. The balance works on the basis of strain measurement, which states that variations in resistance or deformation within the gauge elements are proportionate to the applied forces and moments (Nouri, Mostafapour, Kamran, & Bohadori, 2014). Usually, precision strain gauges or load cells are used in the construction of the balance (see *Figure 25*).

As stated previously, the 6 component balance measures 3 components of force and 3 components of torque. The Force X ( $F_x$ ) – measured along the x-axis – represents the aerodynamic force that acts in the direction of the flow or against it; Force Y ( $F_y$ ) – measured along the y-axis – represents the aerodynamic forces that act perpendicular to the direction of the flow, normally associated with side-slip force; and Force Z ( $F_z$ ) – measured along the z-axis – represents the aerodynamic force that acts perpendicular to the surface of the model, normally associated with thrust or drag. These forces can all be identified using the right-hand rule. Additionally, the Torque X ( $T_x$ ) – measured, again, along the x-axis – represents the rotational force that acts around the longitudinal axis, normally associated with the roll motion experienced by the model; Torque Y ( $T_y$ ) – measured along the y-axis – represents the rotational force or moment that acts around the lateral axis, normally associated with the pitch motion experienced by the model; and lastly, Torque Z ( $T_z$ ) – measured along the z-axis – represents the rotational force or moment that acts around the vertical axis, normally associated with the yaw motion experienced by the model.

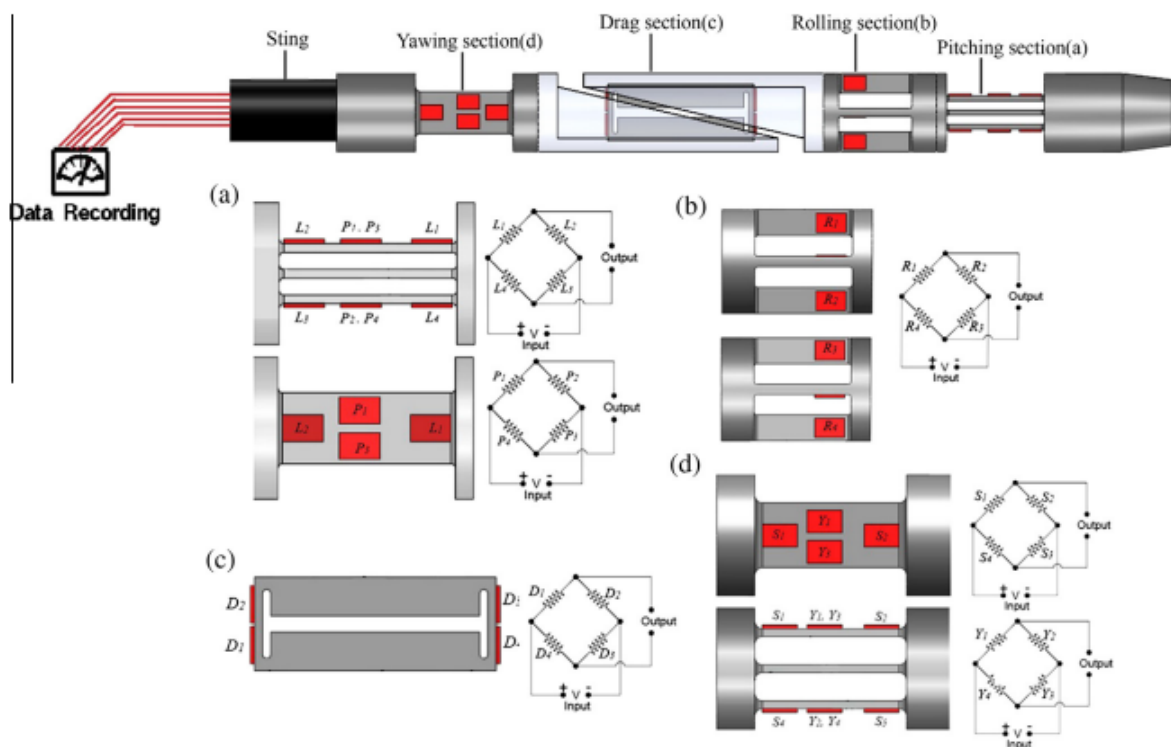


Figure 25 - Six-component balance for the measurement components and three moment components by means of strain gauges (Nouri, Mostafapour, Kamran, & Bohadori, 2014) where (a) is the setup for the pitching sensor; (b) is the sensor for the rolling sensor; (c) is the sensor for the drag, and (d) is the sensor for the yaw motion. The 'Data Recording' icon represents the ATI program.

### 5.2.3 Procedure

The model rocket was positioned within the closed-return low-speed wind tunnel with a working section of width 1.2m, height 1m and length 2.4m, maintaining a  $0^\circ$  pitch and yaw. Refer to Figure 26 to better

understand the reference axis used for this procedure. These adjustments were made manually using appropriate tools: pitch adjustment was achieved manually using a level tool, while yaw adjustment involved positioning a slender steel rod with pointed ends to locate the exact centre of the rod and then the centre of the steel rod was made to be equidistance from to the sides of the working section of the wind tunnel by measuring with a tape. Given the rocket's symmetry, setting the roll angle to  $0^\circ$  was unnecessary; it could be initialised at any arbitrary angle, as the only necessary measurement from the roll was the deviation from the initial reading.

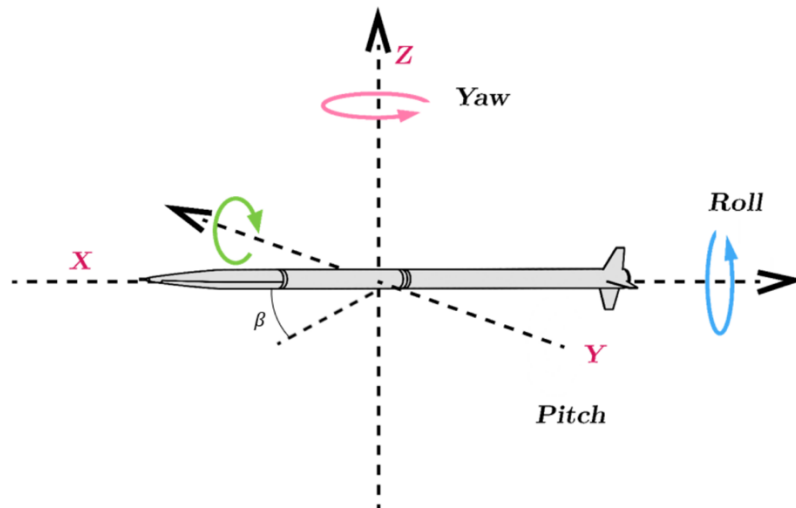


Figure 26 -Reference frame used in the experiment (Cruchet-Pasos, 2023)

To guarantee accurate measurement of the forces and moments acting on the model rocket, the apparatus's six-component balance underwent calibration; to remove any potential biases in the measurements, the calibration process involved zeroing off the model mass using the ATIAQF application.

The wind tunnel is operated by the ATIAQF program – a crucial part of the testing gear – that offers real-time monitoring and control capabilities during the tests. With the use of this software, airflow parameters may be adjusted, guaranteeing consistent and regulated airflow over the model, which was necessary for a precise evaluation of its aerodynamic properties for every experimental run.

Using the ATI programme, a data collection process was started where the recorded data was placed in a specified directory, and file management and file names were carefully considered to avoid losing any information. The frequency and length of the sampling were set using the data collecting options within the application interface.

The sample procedure was started when the data collection parameters were set, with the balance sampling at a rate of 1000 times per second, making the thorough data collection of the aerodynamic forces and moments made possible due to the high sampling frequency. To preserve the validity of the

results, any anomalies or inconsistencies in the measurements were addressed and the testing parameters were changed as needed.

After every test run data was saved in an Excel file for later review and analysis. It included measurements of forces in the X, Y, and Z directions as well as moments about the X, Y, and Z axes.

Overall, this planned testing process guaranteed a reliable and precise evaluation of the model rocket's aerodynamic characteristics to establish the best fin arrangement for the performance of the rocket.



Figure 27 - Low speed model rocket mounted on the 6-component balance within the wind tunnel with side view, back view, and top view presented from left to right.

#### 5.2.4 Relevant Calculations

The model rocket was tested at four different speeds: 10.4mmH<sub>2</sub>O, 20.1mmH<sub>2</sub>O, 30.5mmH<sub>2</sub>O, and 40.2mmH<sub>2</sub>O; at four different yaw angles: 0°, 2°, 4°, and 6°. Assuming the airflow was constant for every experiment, the following relevant calculations were performed to attain the processed data shown on *Table #*.

The air density of the flow inside the wind tunnel can be calculated with *Equation 33*:

$$\rho_{atm} = \frac{P_{at}}{RT_{at}} \quad (Eq. 33)$$

Where  $P_{at}$  was recorded on site from the barometer at 1007hPa therefore *Equation 34* is used to attain atmospheric pressure in Pascals.

$$P_{at} = 1007hPa \times 100 = 100700Pa \quad (Eq. 34)$$

And the atmospheric temperature is calculated using *Equation 35* using the recorded data from the thermometer on site that read  $t_{at}$  was 18°C:

$$T_{at} = t_{at} + 273.16K = 291.16K \quad (Eq. 35)$$

Therefore, the density of the airflow was:

$$\rho_{atm} = \frac{100700}{287.3 \times 291.16} = 1.2038 \text{ kgm}^{-3}$$

The viscosity,  $\mu$  of the air in the wind tunnel can be calculated with *Equation36*.

$$\mu = \mu_{ref} \left[ \frac{T_{at}}{T_{ref}} \right]^{1.5} \left[ \frac{T_{ref} + S}{T_{at} + S} \right] \quad (Eq. 36)$$

Given:  $\mu_{ref} = 1.789 \times 10^{-5} \text{ kgm}^{-3}$ ,  $T_{ref} = 288.2K$ ,  $R = 287.3 \text{ m}^2 \text{ s}^{-2} \text{ k}^{-1}$ ,  $S = 110.4$

$$\mu = 1.789 \times 10^{-5} \left[ \frac{291.16}{288.2} \right]^{1.5} \left[ \frac{288.2 + 110.4}{291.16 + 110.4} \right] = 1.803 \times 10^{-5} \text{ kgm}^{-1} \text{ s}^{-1}$$

Table 8 - Atmospheric parameters of the experiment

$P_{at}(Pa)$	$T_{at}(K)$	$\rho_{atm}(kgm^{-3})$	$\mu (Msm^{-2})$
100700	291.16	1.2038	$1.803 \times 10^{-5}$

As the Betz manometer was broken during testing, the velocity (in mmH<sub>2</sub>O) was calculated with the use of the multitube manometer and the use of Equation 37.

$$H_{betz} = \rho_{manometer} \times \frac{h_1 - h_2}{100} * \sin(\alpha) \quad (Eq. 37)$$

Where  $\alpha = 45^\circ$ , the inclination of the multitube manometer in degrees and  $\rho_{manometer}$  is the density of the fluid inside the multitube manometer and  $(h_1 - h_2)$  is the difference in height in the multitube manometer in mm. The following equation calculates the speed in mmH<sub>2</sub>O when the rocket was set at 2° yaw and the reading of the manometer read  $h_1=8.1$  and  $h_2=5.2$ .

$$H_{betz} = 813.86 \times \frac{8.1 - 5.2}{100} * \sin(45) = \mathbf{20.08 \text{ mmH}_2\text{O}}$$

The velocity,  $U_\infty$  and Reynolds number for the same procedure at 2° yaw, can be calculated with Equations 38 and 39 respectively (Anderson, 2016).

$$U_\infty = \sqrt{\frac{2k\Delta P_{betz}}{\rho_{at}}} \quad (Eq. 38)$$

$$Re = \frac{\rho U_\infty c}{\mu} \quad (Eq. 39)$$

Where  $\Delta P$  is the reading from the Betz manometer in Pa and k is the winds tunnel calibration constant, which is given as 1.03, and c is the length of the rocket from the tip of the nose cone to the base of the body (869mm):

$$U_{\infty} = \sqrt{\frac{2\Delta Pk}{\rho}} = \sqrt{\frac{2 \times 196.92 \times 1.03}{1.2038}} = \mathbf{18.36 \text{ m/s}}$$

$$Re = \frac{\rho U_{\infty} c}{\mu} = \frac{1.2038 \times 18.36 \times 0.869}{1.8032 \times 10^{-5}} = \mathbf{1.065 \times 10^6}$$

The Mach number for the experimental data at 10.39mmH<sub>2</sub>O speed was calculated using the following equation:

$$M = \frac{13.20}{342} = \mathbf{0.04}$$

Table 9 - General wind tunnel calculated values

Yaw angle (°)	Betz manometer reading (mmH <sub>2</sub> O)	Pressure (Pa)	Velocity (m/s)	Reynold Number	Mach number
0	10.39	101.9	13.20	7.66E+05	0.04
2	20.08	196.9	18.36	1.06E+06	0.05
4	30.47	298.8	22.61	1.31E+06	0.07
6	40.17	393.9	25.96	1.51E+06	0.08

After collecting 24000 samples for each yaw angle, the data was averaged to reduce errors. The Force Y values obtained were multiplied by -1 because only the absolute values were needed as the rocket will have a vertical trajectory.

Equation 40 and 41 are used to calculate the Drag and Lift acting on a moving body. Given these forces and force components were compiled using the ATI program, the equations can be rearranged to calculate their coefficients.

$$D = \frac{1}{2} \times \rho \times A \times V^2 \times C_D \quad (\text{Eq. 40})$$

$$L = \frac{1}{2} \times \rho \times A \times V^2 \times C_L \quad (\text{Eq. 41})$$

The only values for drag attained by the ATI program that could remain raw were the values attained of Force (X) for the model at a yaw angle of 0°. For the remaining angles, *Equation 42* was used to calculate the drag. The values for lift, F(z), were left unprocessed as they were not components of the force along the Z axis, therefore left as Lift = Fz. The following is the calculation used to calculate the drag on the 4-fin model with at a yaw angle ( $\varphi$ ) of 2° at a speed of 18.36m/s:

$$D = \frac{F_X}{\cos(\varphi)} + \frac{F_Y}{\sin(\varphi)} \quad (\text{Eq. 42})$$

$$D = \frac{0.237}{\cos(2)} + \frac{0.071}{\sin(2)} = 2.27 \text{ N}$$

The coefficient of drag and lift can be calculated with the use of *Equations 43 and 44* respectively.

$$C_D = \frac{F_x}{\frac{1}{2} \times \rho \times A \times U^2} \quad (\text{Eq. 43})$$

$$C_L = \frac{F_y}{\frac{1}{2} \times \rho \times A \times U^2} \quad (\text{Eq. 44})$$

Where  $F_x$  are the forces in the x direction (in the direction the rocket is facing) and  $F_y$  are the forces in the y direction (perpendicular to the rocket),  $\rho$  is the density of the air inside the tunnel, A is the reference area (cross-section of the rocket) calculated with *Equation 45*, and  $V$  is the freestream velocity inside the tunnel. The following is an example calculation for the simulation at a speed of 18.36m/s for the rocket set at 0° yaw.

$$A = 2\pi r^2 = 2 \times \pi \times 0.0430^2 = 0.0116\text{m}^2 \quad (\text{Eq. 45})$$

$$C_D = \frac{0.20512}{\frac{1}{2} \times 1.2038 \times 0.0116 \times 18.36^2} = 0.0872$$

$$C_L = \frac{0.04635}{\frac{1}{2} \times 1.2038 \times 0.0116 \times 18.36^2} = 0.0197$$

## 5.2.5 Results

The aim of this procedure was to observe the effect of the number of fins on a rocket by comparing experimental results of both configurations at different yaw angles. The data was successfully gathered, processed and tabulated, and the results were presented as plotted graphs in this section.

Table 10 - Processed data for low wind tunnel experimenting.

Speed (mmH <sub>2</sub> O)	Speed (m/s)	Yaw	3 Fins				4 Fins			
			CD	CL	D	L	CD	CL	D	L
10.39	13.20	0°	0.0515	0.1186	0.0628	0.1446	0.0406	0.0179	0.0496	0.0219
		2°	0.0171	0.0441	0.1982	0.1039	0.0314	-0.0064	0.1982	-0.0151
		4°	0.0141	-0.0004	0.4884	-0.0015	0.0217	-0.0042	0.4884	-0.0150
		6°	0.0109	0.0172	0.8457	0.0812	0.0161	0.0012	0.8457	0.0055
20.08	18.36	0°	0.0841	0.0443	0.0209	0.0537	0.0841	0.0443	0.0383	-0.0078
		2°	0.0466	0.0636	0.1097	0.1499	0.0520	0.0187	0.1226	0.0440
		4°	0.0334	0.0320	0.2680	0.2641	0.0369	0.0033	0.2629	0.0913
		6°	0.0233	0.0197	0.4049	0.0105	0.0281	0.0068	0.4641	0.0942
30.47	22.61	0°	0.1366	0.0446	0.0172	-0.0005	0.1366	0.0446	0.0264	-0.0051
		2°	0.0750	0.0739	0.0787	0.0753	0.0735	0.0255	0.0870	0.0077
		4°	0.0453	0.0035	0.1620	0.0126	0.0516	0.0051	0.1846	0.0181
		6°	0.0300	0.0160	0.1805	0.0960	0.0373	0.0081	0.2198	0.0468
40.17	25.96	0°	0.1794	0.0409	0.0133	0.0210	0.1794	0.0409	0.0196	0.0014
		2°	0.0859	0.0022	0.0549	0.0465	0.0985	0.0200	0.0663	0.0160
		4°	0.0523	0.0243	0.1071	0.0571	0.0627	0.0155	0.1333	0.0288
		6°	0.0383	0.0204	0.1805	0.0960	0.0466	0.0099	0.2198	0.0468

The graphs for the processed data were plotted in graphs to help the visualise the attained results.

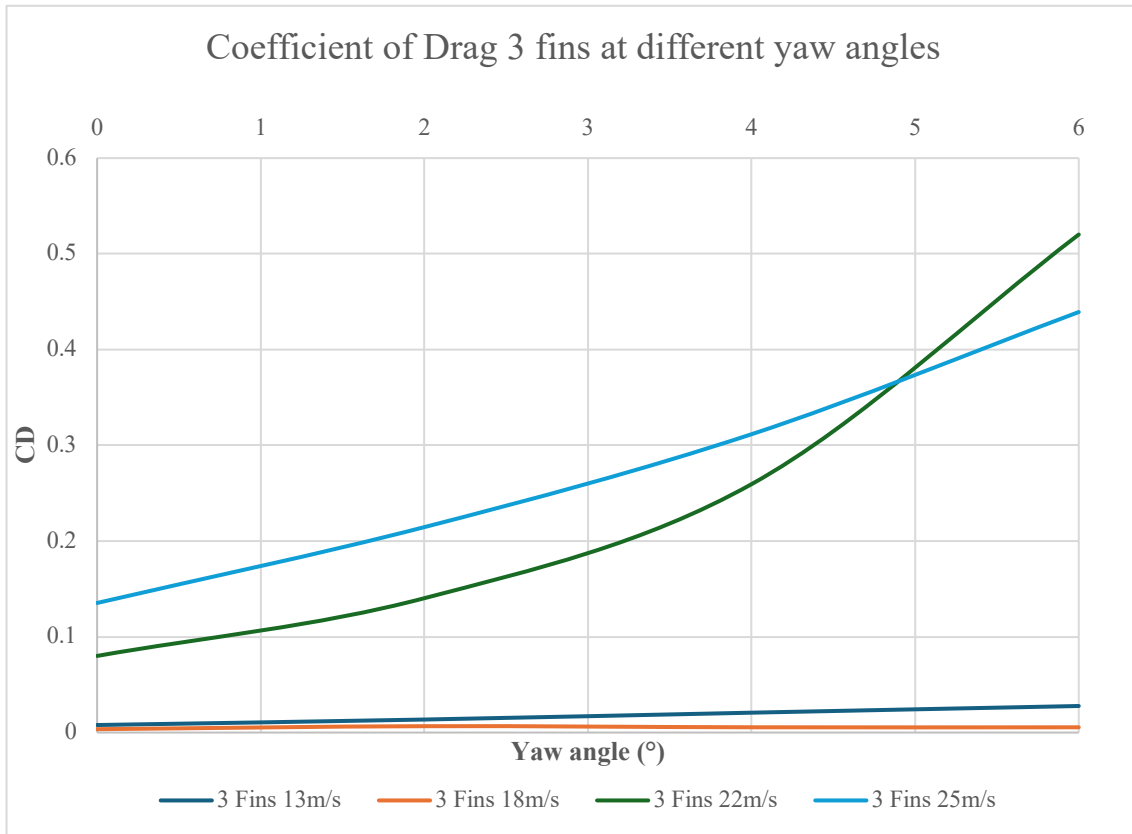


Figure 28 - Plotted graph of the drag coefficient against the tested yaw angles for the 3-fin configuration

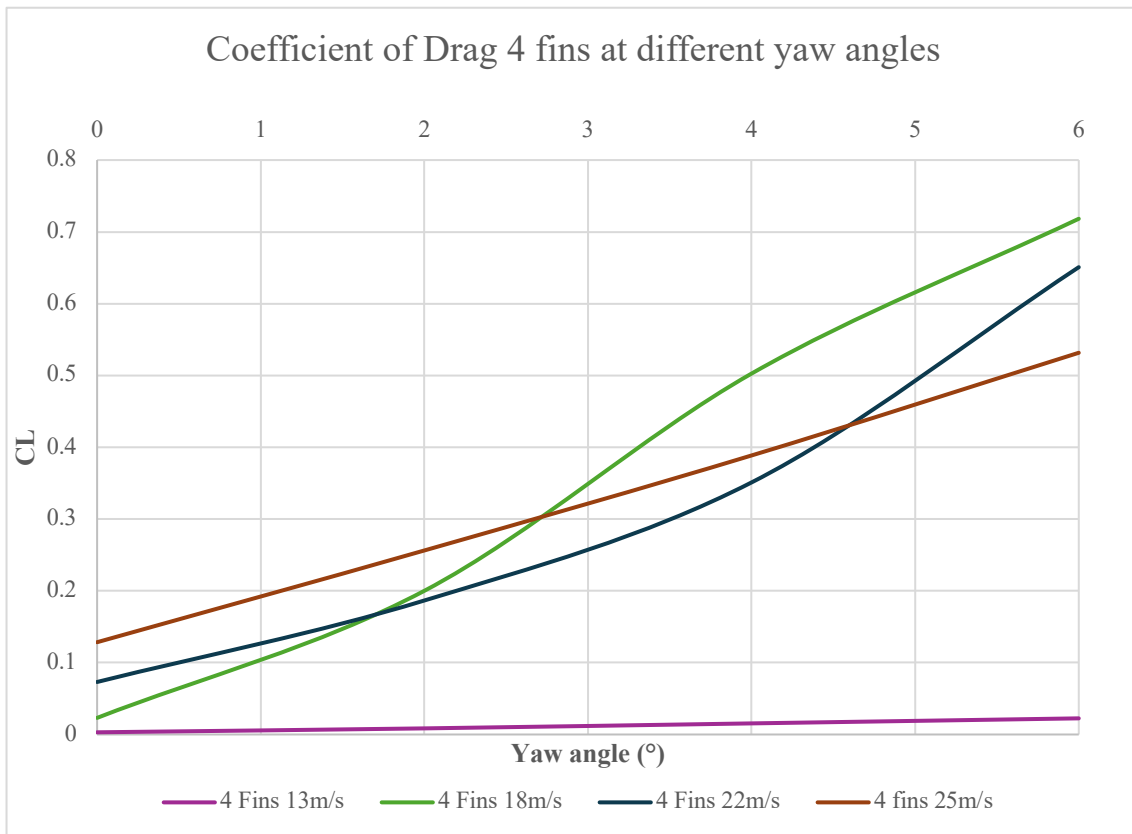


Figure 29 - Plotted graph of the drag coefficient against the tested yaw angles for the 4-fin configuration

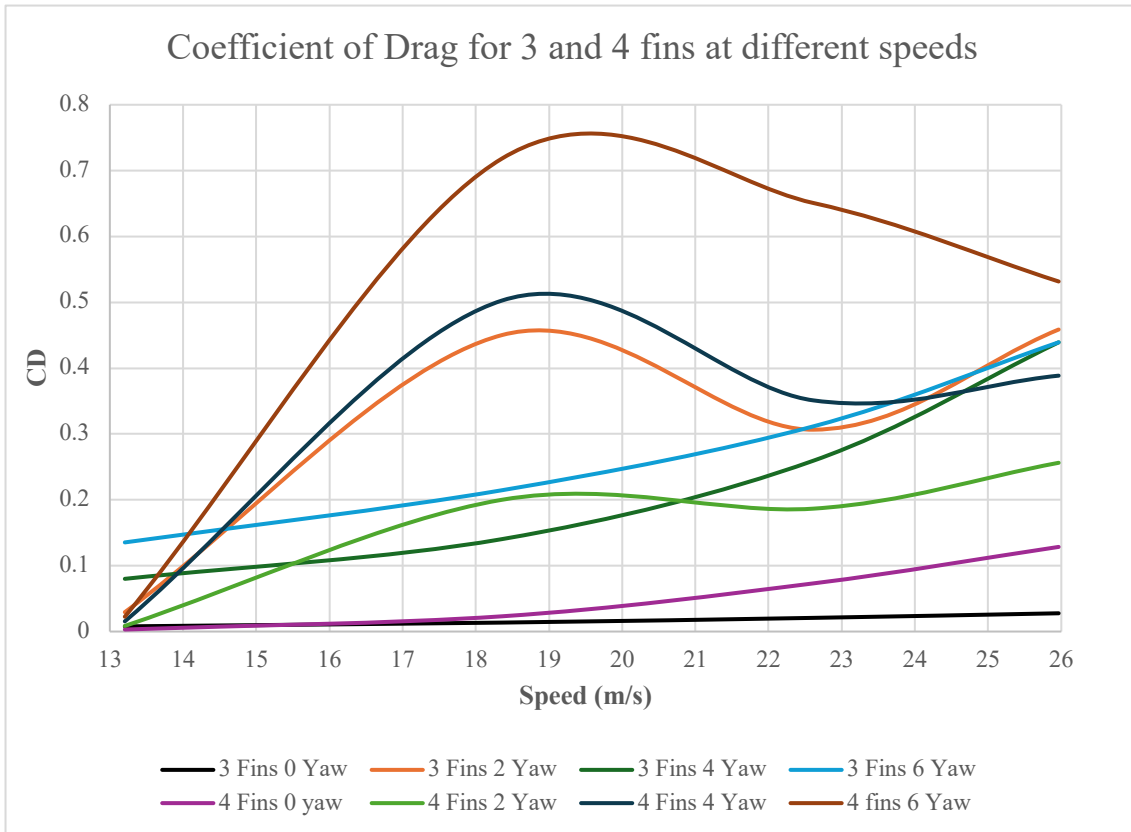


Figure 30 - Plotted graph of the drag coefficient against the tested yaw angles for the 3-fin and 4-fin configuration

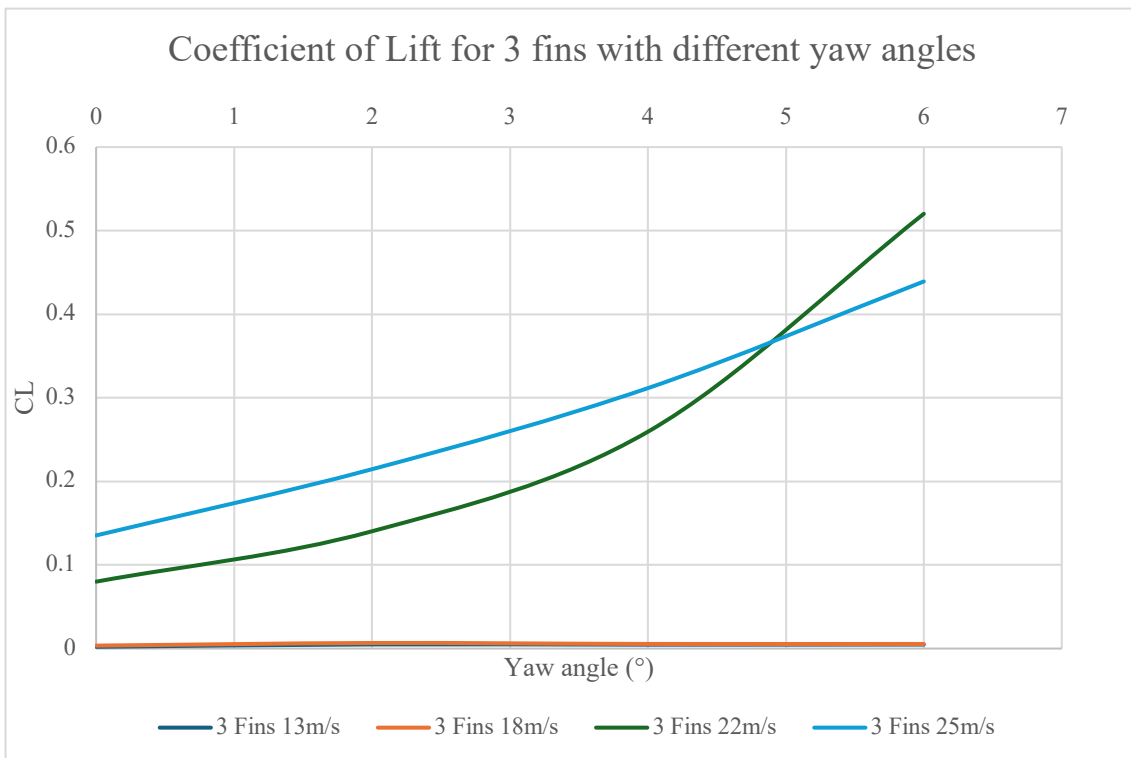


Figure 31 - Plotted graph of the lift coefficient against the tested yaw angles for the 3-fin configuration

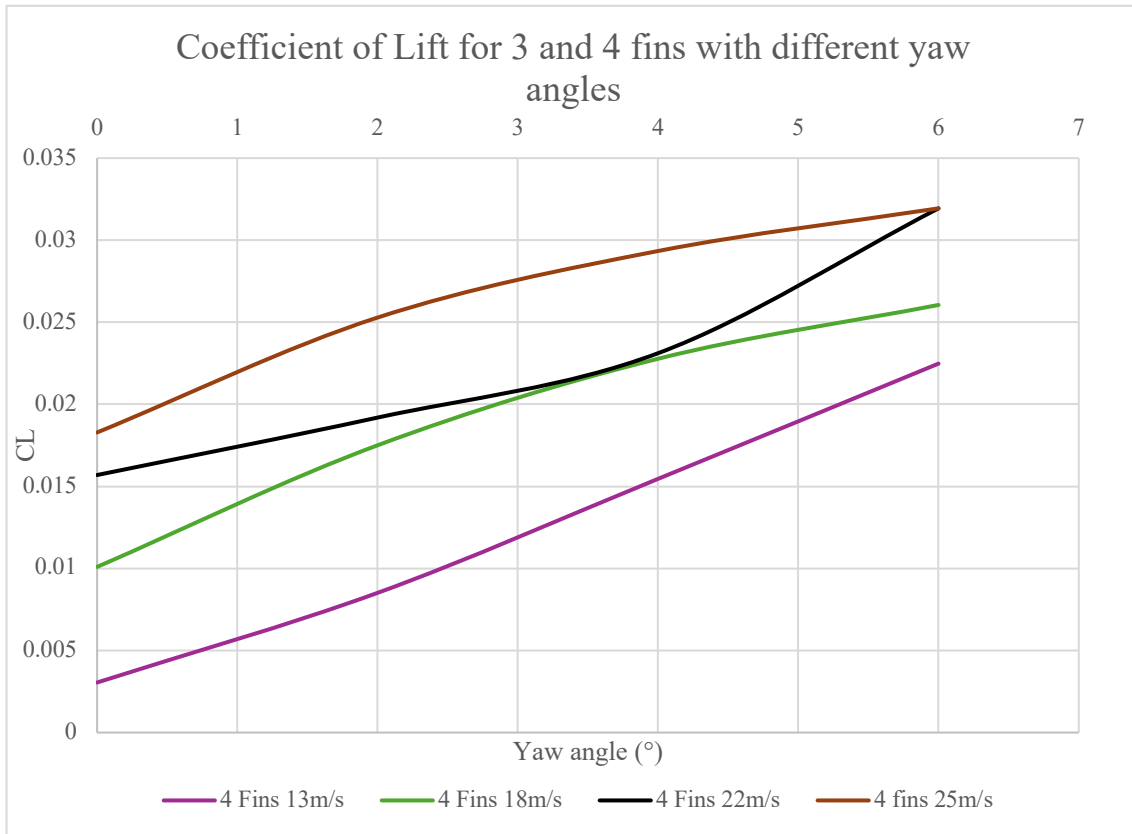


Figure 32 - Plotted graph of the lift coefficient against the tested yaw angles for the 4-fin configuration

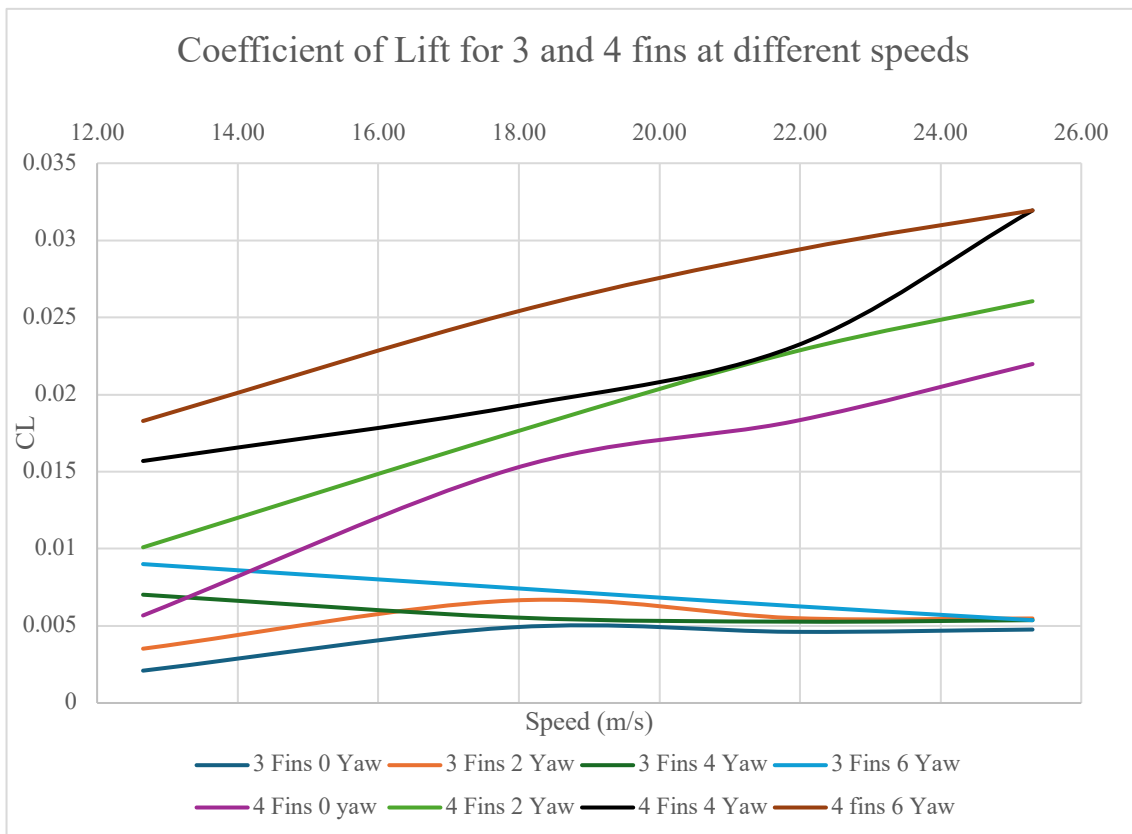


Figure 33 - Plotted graph of the lift coefficient against the tested yaw angles for the 3-fin and 4-fin configuration

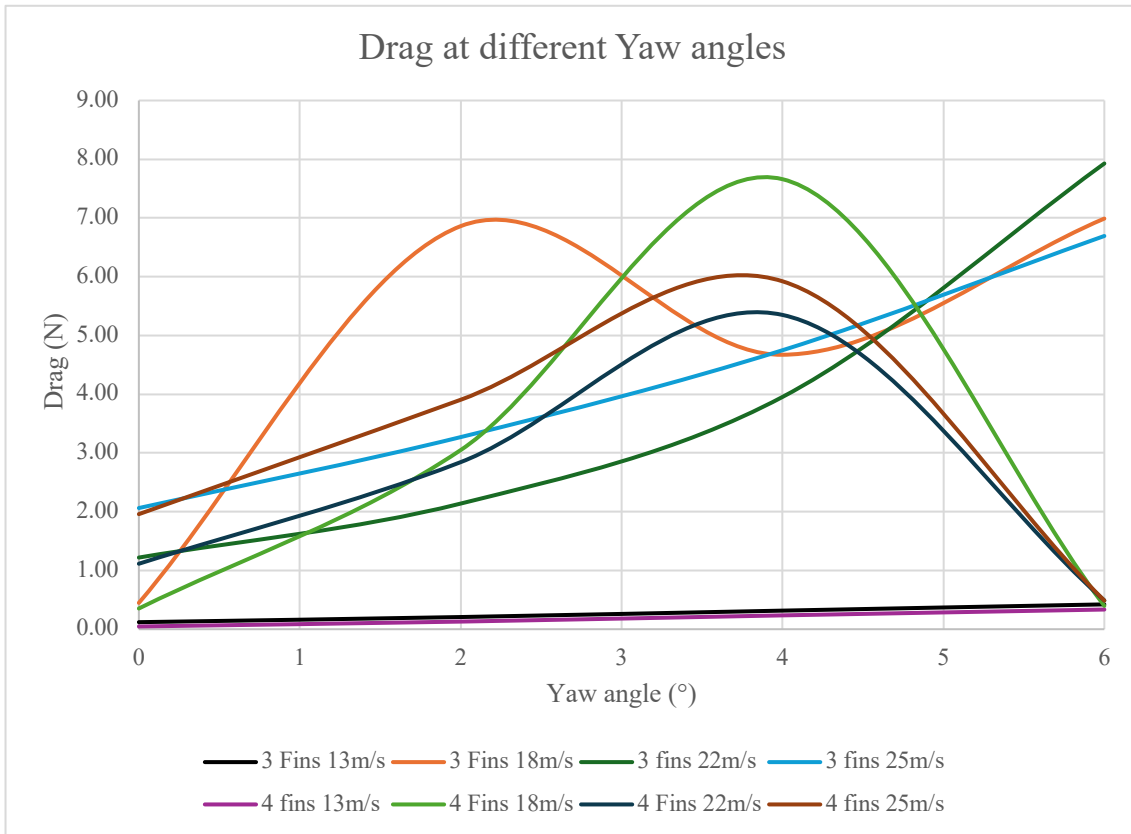


Figure 34 - Plotted graph of the drag against the tested yaw angles for the 3-fin and 4-fin configuration

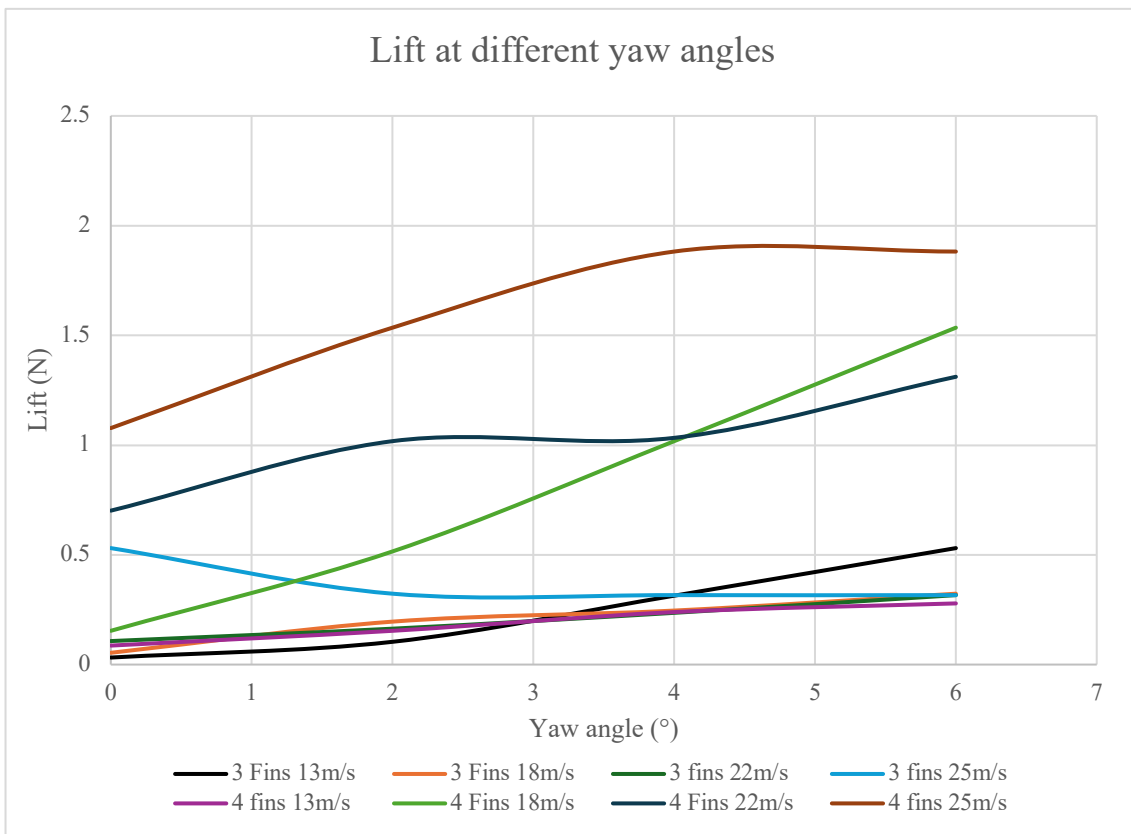


Figure 35 - Plotted graph of the lift against the tested yaw angles for the 3-fin and 4-fin configuration

### **5.2.6 Limitations and Improvements**

Numerous difficulties were encountered during the wind tunnel testing process which affected the precision and reliability of the experimental results. One significant problem was the malfunction of the Betz manometer, making it impossible to monitor air velocity directly in the working section of the wind tunnel. As a result, velocity readings had to be approximated by first setting the tunnel speed and using the differential pressure measured with the tilted multitube manometer. The manometer had two pressure tapings inside the tunnel, one to measure the pressure at the beginning of the working section and another at the end of the working section and was tilted at a 45° angle. Therefore, a limitation encountered during wind tunnel testing was the velocity measuring technique was made the procedure prone to human error which impacted the reliability and accuracy of the wind tunnel data.

Moreover, when reading off the inclined multitube manometer, parallax error occurred. This might have led to erroneous measurements, which would have compromised the experiment's accuracy. If this experiment were to be reproduced, parallax error may be eliminated by using sophisticated, computerised equipment that can detect airflow characteristics precisely and automatically (electronic manometer), which would result in more accurate measurements and calculations, and minimise the need for manual corrections. Furthermore, taking multiple pressure tapping readings from the manometer tubes and averaging them would be another method of eliminating parallax error, though this might not be as efficient as utilising an electronic manometer. Lastly, pressure tapings on the length of the model rocket and measuring the pressure difference over multiple sections of it would also enhance the accuracy of the results.

In addition, to maintain optimal performance and prevent equipment faults, a thorough maintenance and calibration schedule should be done for every wind tunnel apparatus. Regular inspections and calibration checks can help find and fix problems before they affect experimental results, especially for important instruments like manometers and six-component balance.

## **5.3 High Speed Experimental Testing (Ardrit)**

### **Equipment and Method**

A nosecone with properties as described in / has been manufactured to a scale at which it may fit in the working section of a supersonic wind tunnel. The design is that of the Von Karman nosecone with fineness ratio 5. Four pressure tapings are located along the nose cone as stated in Table 11, radially displaced by 90° so as to allow for the extraction of a pressure tapping as close to the leading edge as possible. The nose cone is manufactured out of an aluminium body, where a brass tip has been made separately to incorporate tapping 1. For tapings 2 through 4 a larger diameter hole is drilled from the

nose cone body and a brass fitting is tapped into the hole, the model was fully fitted together before a final layer was taken off on the CNC machine and the model was polished to ensure no surface perturbation exist. This is done to allow for easier drilling of the fine pressure tapping holes seperately of the nosecone. The nose cone was manufactured by the technicians at the Queen Mary University of London SEMS Mechanical Workshop.

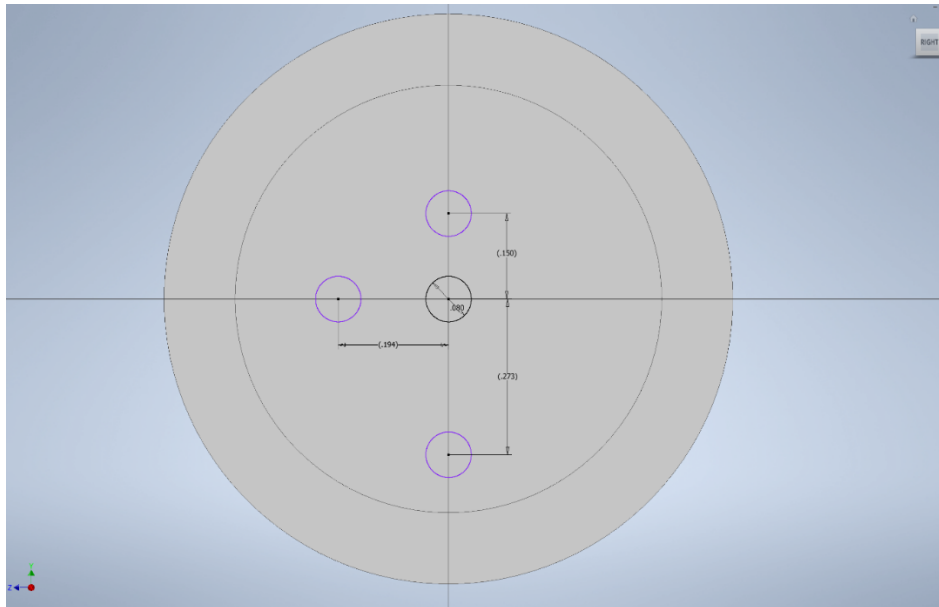


Figure 36 – Tapping extraction holes

Table 11 – Model parameters

Scale (experimental : full)	0.5734 : 1
Fineness ratio (L/d)	5
Length	0.127m
Pressure tapping diameter	0.2mm
Production time	~ 4 months
Material	Aluminium, Brass

Table 12 – Tapping locations

Tapping number	Distance from leading edge (x/L)
1	0.1
2	0.3
3	0.5
4	0.7

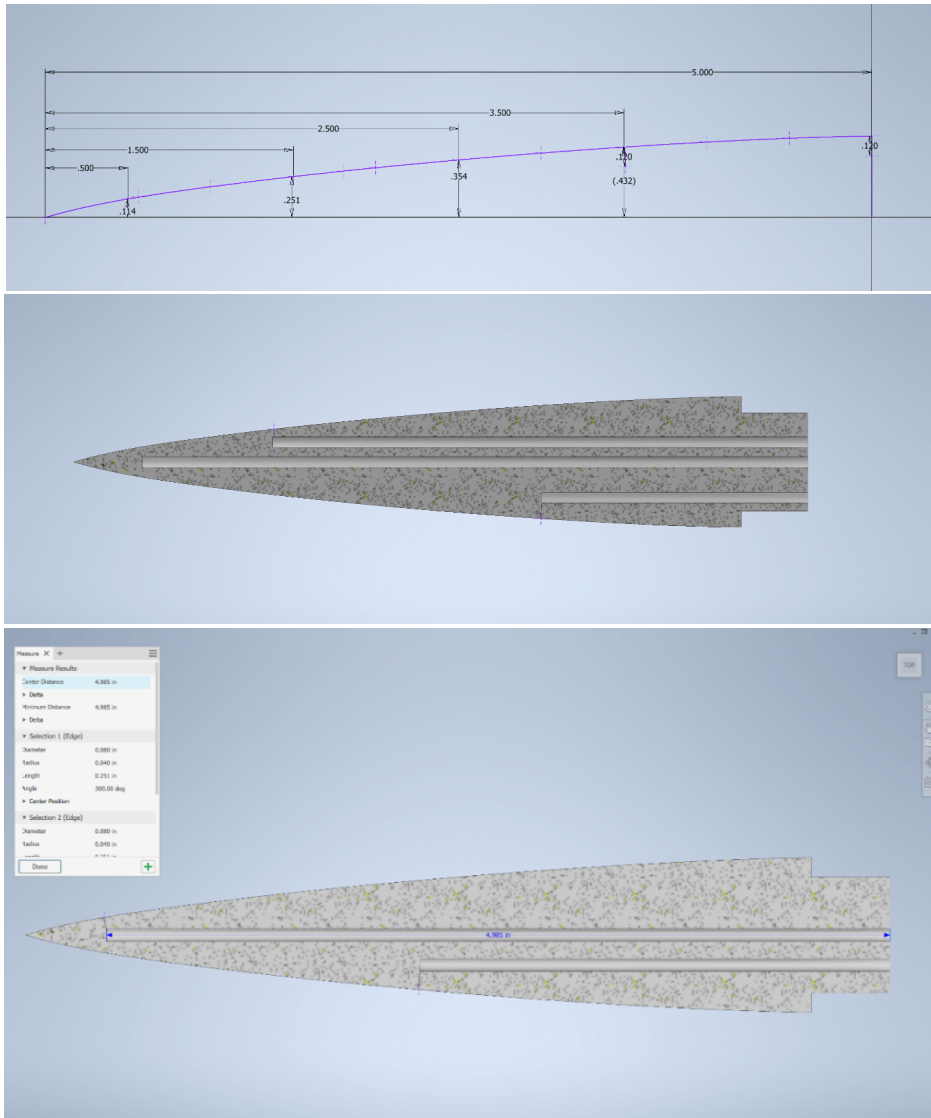


Figure 37 – Model dimensions



Figure 38 – The model

The nose cone will be placed in the supersonic blowdown wind tunnel at the Queen Mary University of London SEMS High Speed Lab. The working section of the wind tunnel is 165 x 165mm and has the capacity to produce a Mach number of 2.0 or 3.0 with a Reynolds number up to  $65 \times 10^6$ . The blowdown wind tunnel is a closed system wind tunnel in which pumps are used to create a pressure gradient over the tunnel. Upstream of the working section a pump pressurizes a chamber with dry air and a vacuum pump creates a chamber of low pressure down stream. The two chambers are closed by digital valves and once operated, high pressure passes through a convergent divergent valve where the flow is compressed down to the throat diameter, at which the sonic threshold is reached and the expansion in the divergent duct further increases the velocity magnitude. Air then passes through the working section and is compressed back down in a second throat to reduce its velocity before reaching the vacuum chamber. In between the storage tank and working section a settling chamber is used to decrease unsteadiness in the flow, at which point the stagnation pressure and temperature of the flow can be measured. Being an enclosed system, the operating time of the tunnel is short and decreases with a higher pressure gradient however, the tunnel has the capability to produce a high and steady Mach number with a fast starting time. As the experiment only calls for the steady state capture of the flow field around the nose cone, the short operating time is sufficient with the added benefit of reducing the overall stress exhibited on the model.



*Figure 39 – Wind tunnel setup*

The model pressure tapings are connected to a Scanivalve DSA 3217 digital sensor array capable of measuring and recording data from 16 points at one time. The sensor measures the gauge pressure to a full scale accuracy of  $\pm 0.05\%$  and records data at a polling rate of 4Hz. The Scanivalve will be run during the operation of the wind tunnel allowing the pressure over the nosecone to be time averaged.

To provide additional data for analysis, a Schlieren method of flow visualisation of the run will be incorporated. The Schlieren method is a density based solution to flow visualisation of supersonic flows. As it is found that the refractive index of air is a function of its density, changes in density within a flow field can be visualised with a grey scale light image. The method uses a uniform light source passed through a slit and onto a concave mirror which then reflects the light through the working section. When placed at the correct focal point, the concave nature of the mirror produces a segment of parallel rays of light across the working section, after which a similar concave mirror will refocus the light to a point after which the image is flipped. Deviations in density will cause the light passing through that section to deflect and not return to the same focal point as the rest of the light. A sharp edged instrument, such as a blade, placed near the focal point of the mirror will block light which has been deflected, in which the sensitivity of the method can be adjusted by moving the blade closer to the focal point to increase sensitivity or away to decrease it. After this point a camera is placed to capture the flipped image. The image presents as a grey scale depiction where dark regions indicate an area of higher density and light regions indicate a region of low density. Shockwaves have a steep gradient and step change in density therefore the Schlieren method is ideal for visualising this flow regime. From the Schlieren method the shockwave angle due to deflection will be measured together with the Mach wave angle in order to verify the flow Mach number. The Mach number can be derived from the Mach angle  $\mu$ ;

$$M = \frac{1}{\sin(\mu)}$$

### 5.3.1 Pressure distribution

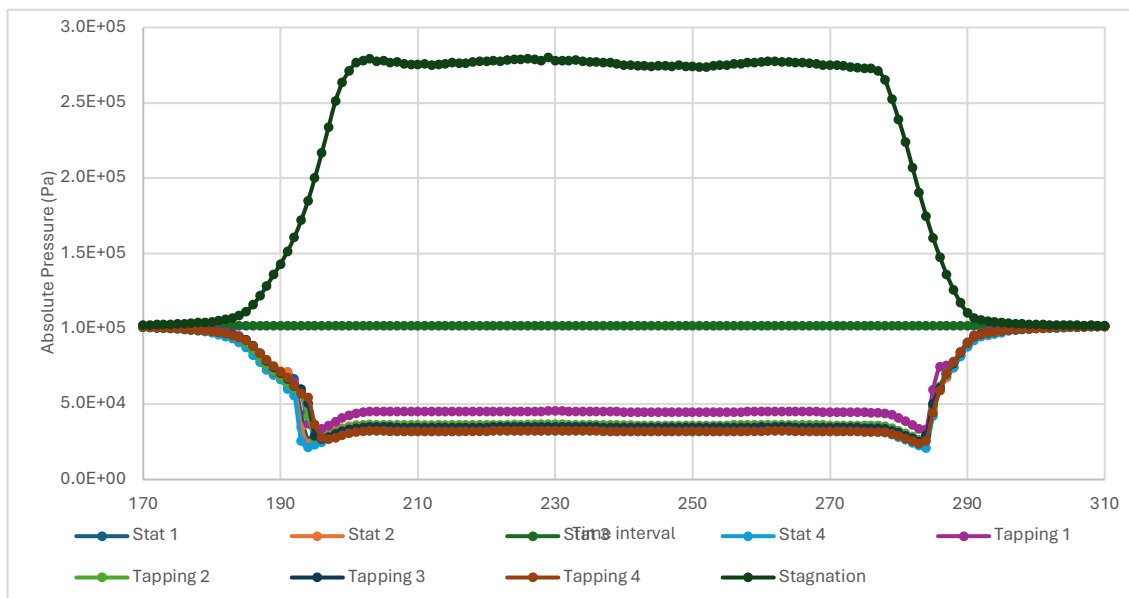


Figure 40 – Pressure over time

Table 13 – Average pressure ratio with tapping

x/L	0.1	0.3	0.5	0.7
Average	0.16303	0.13176	0.12696	0.11666

### 5.3.2 Schlieren Photograph

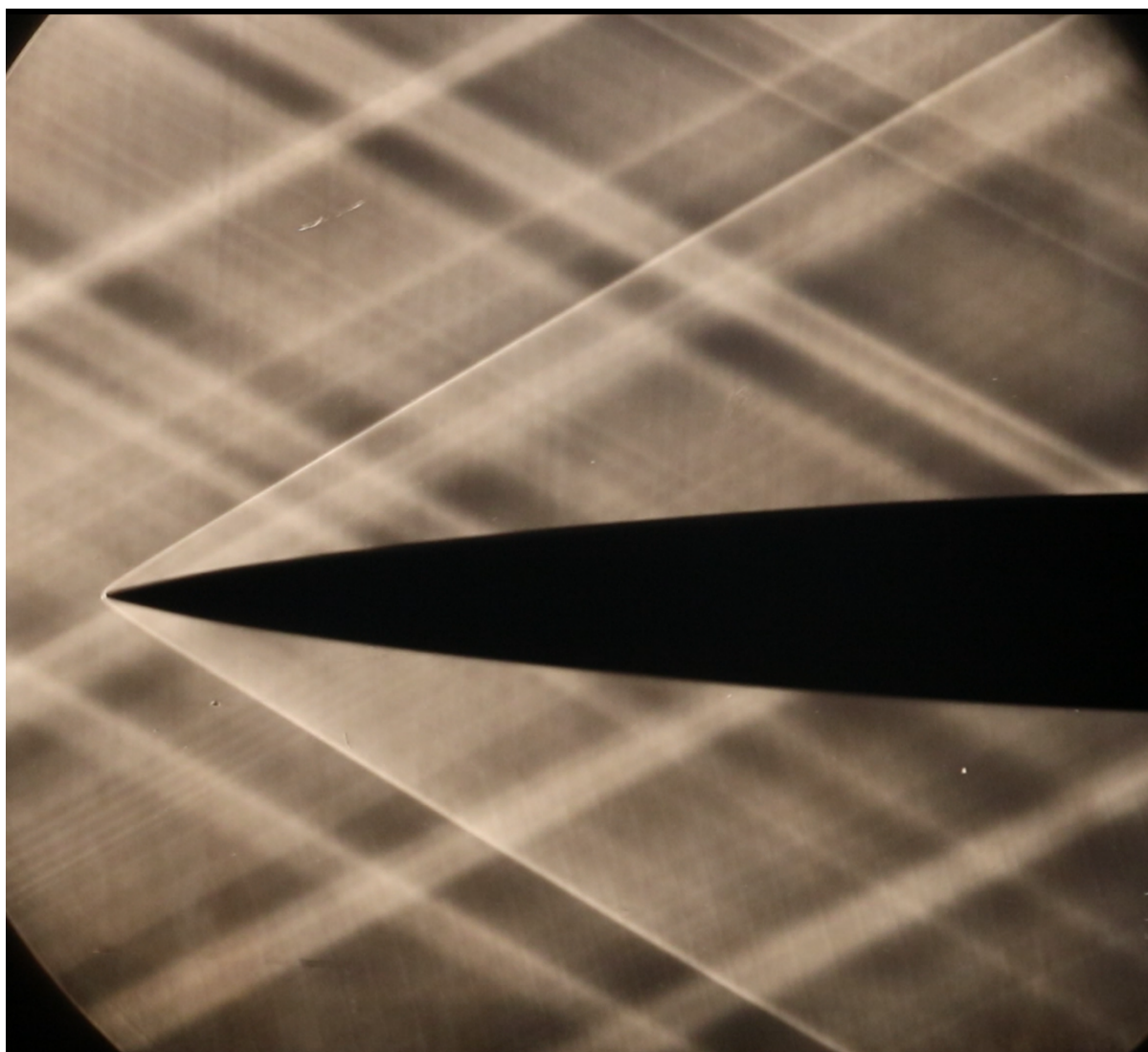


Figure 41 – Schlieren Photo

Table 14 – Schlieren measurements

Shockwave angle (°)	Mach angle (°)	Mach number
31.2	29.435	2.034

## 5.4 CFD (Ardrit)

### 5.4.1 Methodology

The analytical problem will be considered in several geometrical configurations beginning with a 2-dimensional axisymmetric model as is the case in the experimental high speed testing with the scaled down nose cone, which will progress onto a 3 dimensional scale model of the rocket.

### 5.4.2 Axisymmetric

The supersonic wind tunnel testing will be modelled as a validation case for the commercial software STARCCM+'s ability to accurately predict heavily compressible flows and shockwaves. The test case at Mach 2.0 will be considered after which the analysis of the nose cone will be conducted in a transonic and supersonic regime of  $0.8 < M < 1.4$ .

The axisymmetric flow calculations were conducted of the scaled down nose cone with a semi-infinite body tube. This was done as the fin section could not be represented in a two dimensional format and validation data of the fins was not collected for high speed testing. Having a semi-infinite body tube as compared to a scaled down body tube reduces the flow separation and expansion behind the nose cone thus reducing the complexity of the flow field. This means that the calculated solution will be as alike to the experimental testing while also maintaining a smaller grid size to reduce the computational expense. Due to the disruptive nature of a shockwave and their reflection from surfaces, a large domain was modelled, spanning 20 nose cone lengths in all directions from the leading edge of the nose cone.

A hexahedral, hanging node transition, mesh type was chosen for this test case due to its higher computational efficiency as all nodes are on a cartesian grid and do not require trigonometric functions or mappings to define. Generally a polyhedral mesher is chosen for rocket flows however as the geometry of the axisymmetric case was not complex, a node could be placed on the leading edge with a larger surface refinement in areas of curvature to accurately represent the geometry. The mesh was additionally refined in regions where compressibility effects and large gradients occurred in the flow. Employing an axisymmetric solution meant that a cell size in the magnitude of  $2 \times 10^{-4}$  could be maintained over the shockwave while keeping a sub 0.5 Million cell mesh. The mesh was built in a RANS type configuration where a layering mesher was applied on the surface to add several thin layers with a high aspect ratio, for the wall thickness and assuming turbulent boundary layer thickness condition of equations. This allows for the resolution of the velocity gradient perpendicular to the wall is necessary for resolving shear forces, while not over refining the mesh. The layers were done so as to maintain a low wall  $Y^+$  treatment with the total thickness increasing in the spanwise direction so as not to artificially influence the free flow inertial regime close to the leading edge where the boundary layer is thin, additionally prism layers are added to the axis in order to have a smooth transition of layers in the streamwise direction at the sharp edge where layers would otherwise be automatically collapsed by

the software. The symmetry axis is that of the Y axis in which the distribution about the Y axis is modelled as being uniform, with the stream wise direction in the positive X .

From a converged solution, the static pressure along the surface of the nose cone and the drag and coefficient of drag due to both pressure and shear forces will be extracted, drag due to the body tube will be neglected as it is not within the scope of this analysis. Shockwave angle will be measured as well as shockwave location in cases of normal shockwaves.

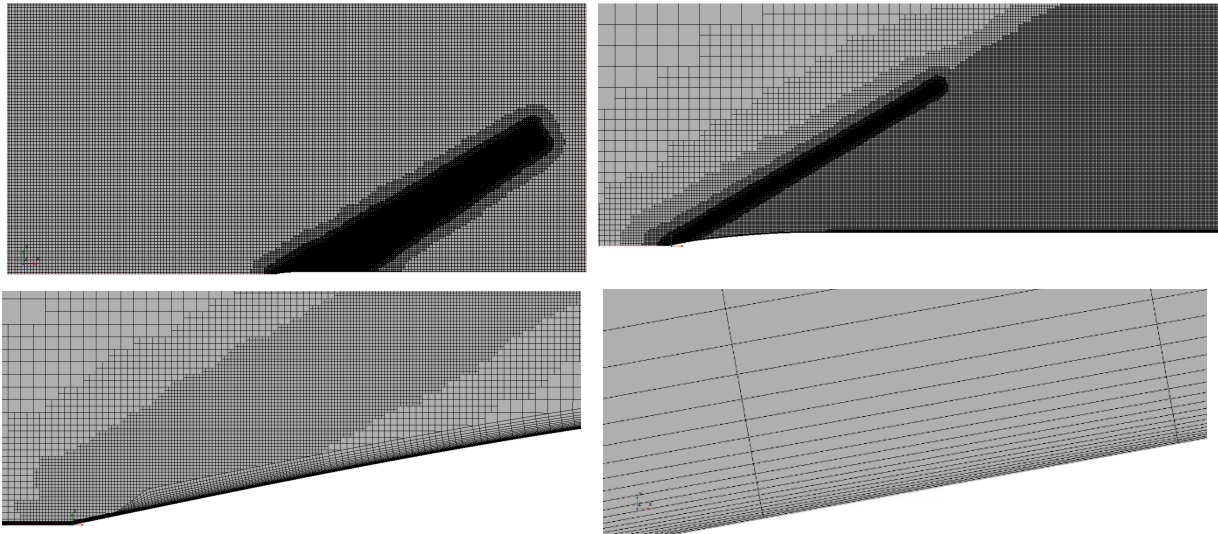


Figure 42 – Axisymmetric mesh Far (top left) near (bottom right)

Table 15 – Mesh parameters

Chosen prism layer total thickness (mm)	Number of prism layers	Wall thickness specification (mm)
0.4 - 2	30	$8.705947 \times 10^{-4}$

Table 16 – Boundary conditions

Boundary	Specification	Values
Inlet	Stagnation Inlet	Total Pressure: $2.7646 \times 10^5$ Pa Static Pressure: $3.2246 \times 10^4$ Pa Temperature: 296.15K
Outlet	Pressure outlet	Pressure: $3.2246 \times 10^4$ Pa Temperature: 296.15 K
Upper Surface	Symmetry Plane	Slip condition
Axis	Axis	Axisymmetric axis
Nose cone and body tube	Wall	No Slip condition Adiabatic Condition Smooth surface
Number of Cells	Hexahedral	395864
Re		$6 \times 10^6$

For the initial axisymmetric case, a RANS approach was taken as the main aim was in the identification of compressibility effects and prediction of drag which do not require the resolution of turbulence, additionally the problem is steady in nature with a constant flow field therefore a URANS approach is not necessary. While  $k-\omega$  models are common in studies for rocket aerodynamics, these are generally conducted at low/ subsonic velocities. An argument for the  $k-\omega$  model is also that it handles adverse pressure gradients better, however the gradual slope of the Von Karman nose cone is designed to be more aerodynamically efficient than a standard nose cone therefore in the local domain of the nose cone, the flow should be mostly wall bounded.  $k-\epsilon$  has been chosen for use due to its suitability for higher Reynolds numbers which are expected due to the high speed flow, in addition to its strong convergence and handling of complex flows. STARCCM+ uses a 4 cycle Algebraic MultiGrid solver with a Gauss-Seidel relaxation scheme for error smoothing, within this an implicit linear upwind discretisation is used to prevent propagation of properties upstream of a disturbance, as is the case for a supersonic flow. The solver uses a density based solver for the coupled energy and flow which is necessary for the compressible regime, and a Realizable  $k-\epsilon$  Two Layer turbulence model. Convergence criteria is set for a magnitude of  $10^{-4}$  with the coefficient of drag being monitored.

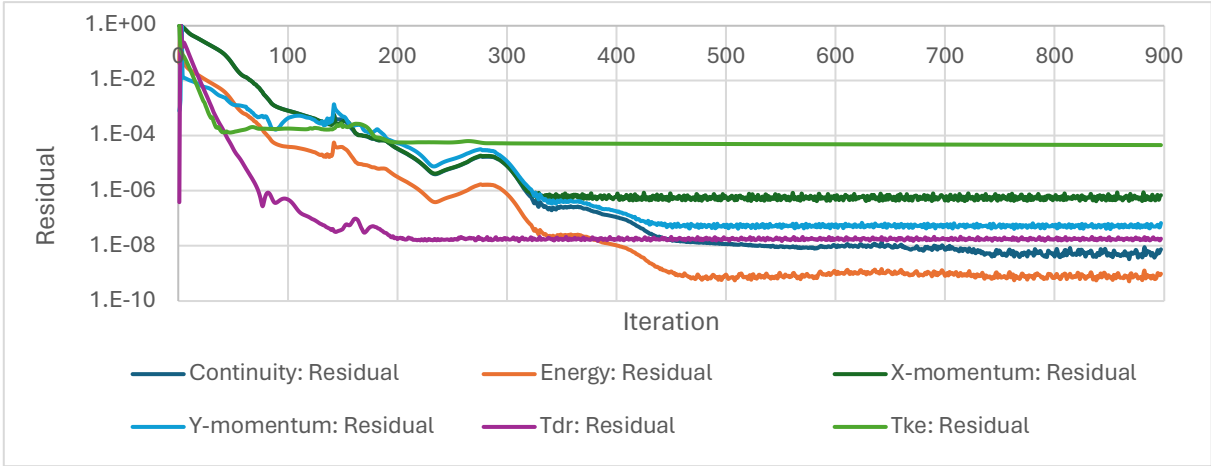


Figure 47 – Residuals graph for CFD

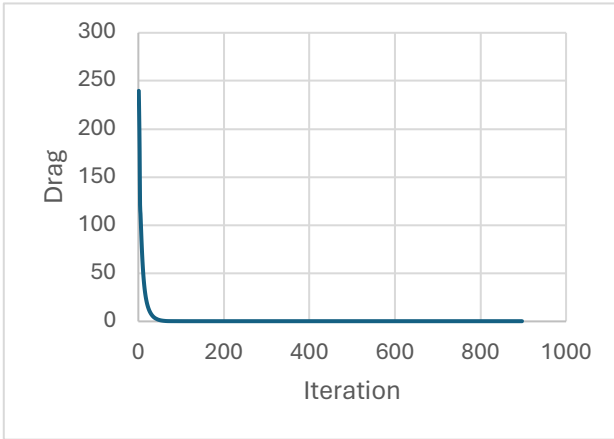


Figure 45 - Figure 46 – Drag against number of iterations

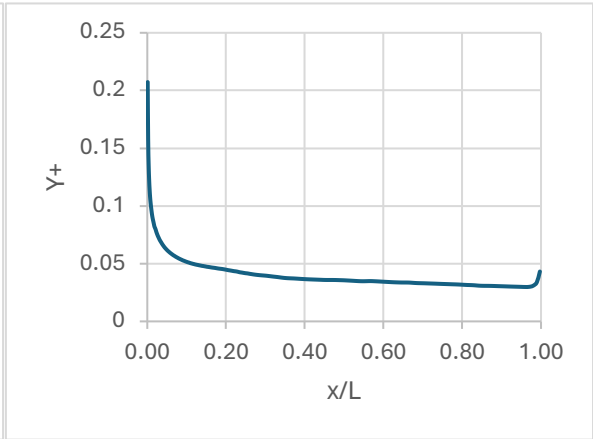


Figure 43 - Figure 44 – Y+ value against x/L

### 5.4.3 Validation

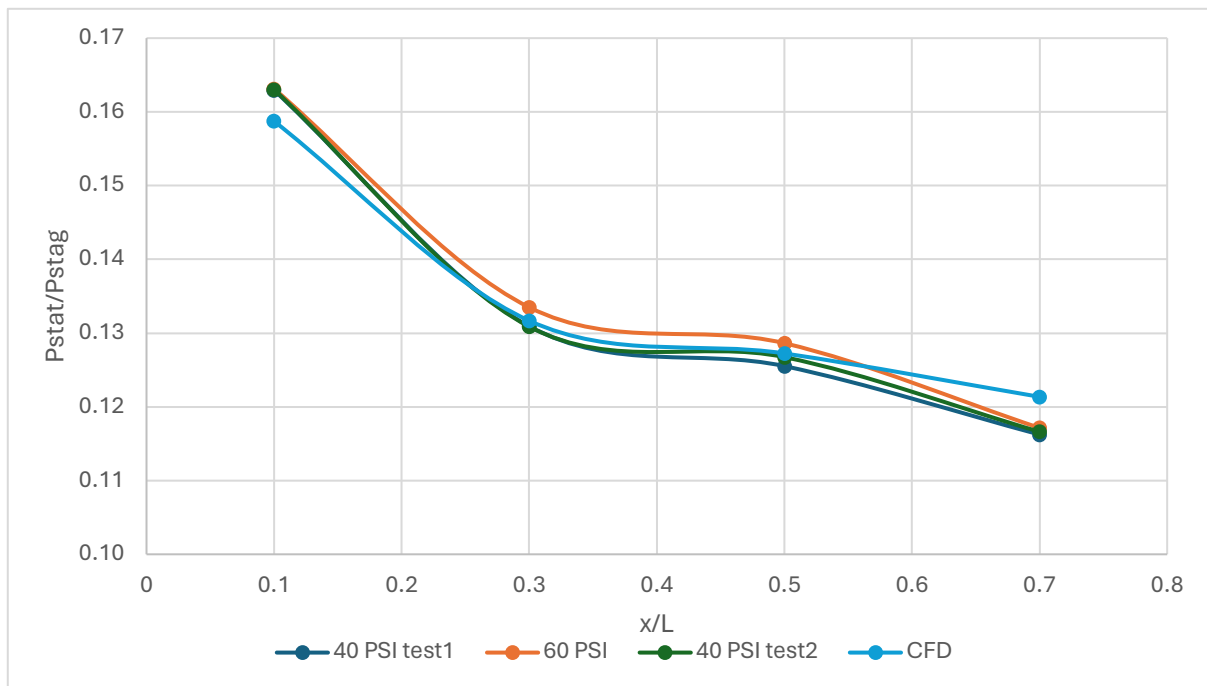


Figure 48 –  $P_{stat}/P_{stag}$  against  $x/L$

Table 17 - CFD attained values

Average pressure ratio (Experimental)	Pressure ratio (CFD)	% Error
0.16303	0.15873	2.635
0.13176	0.13168	0.066
0.12696	0.12724	0.220
0.11666	0.12136	4.021

Table 18 - CFD attained values

Source	Cd by Cranfiel (Maarson, 1954)	Cd by modified ogive of curvature (Maarson, 1954)	Cd by E.perkins (M = 3.0) (Perkins, Jorgensen, & Sommer, 1958)	Axisymmetric CFD
Cd (nose cone)	0.0226	0.0230	0.029	0.0231

## Results

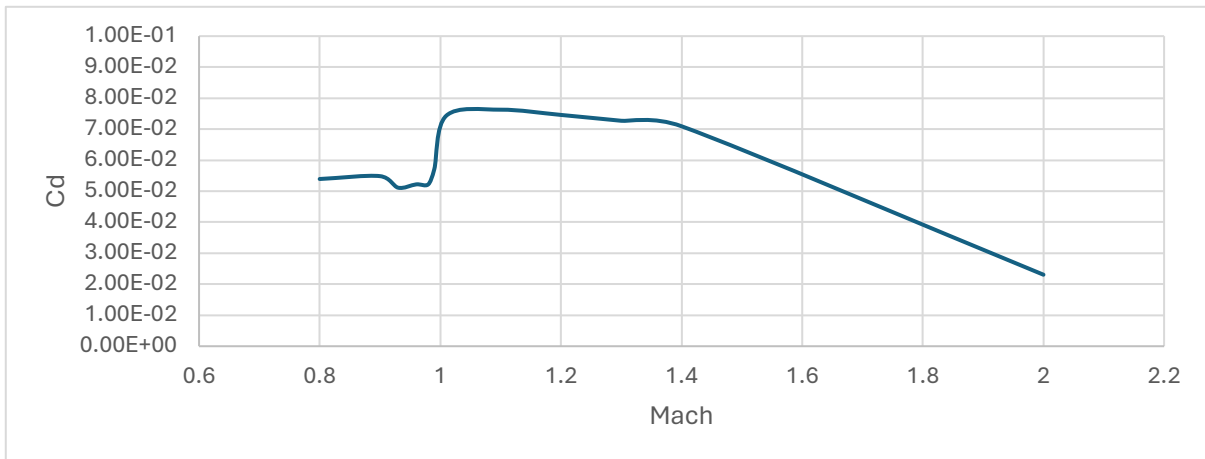


Figure 49 – Cd against Mach number

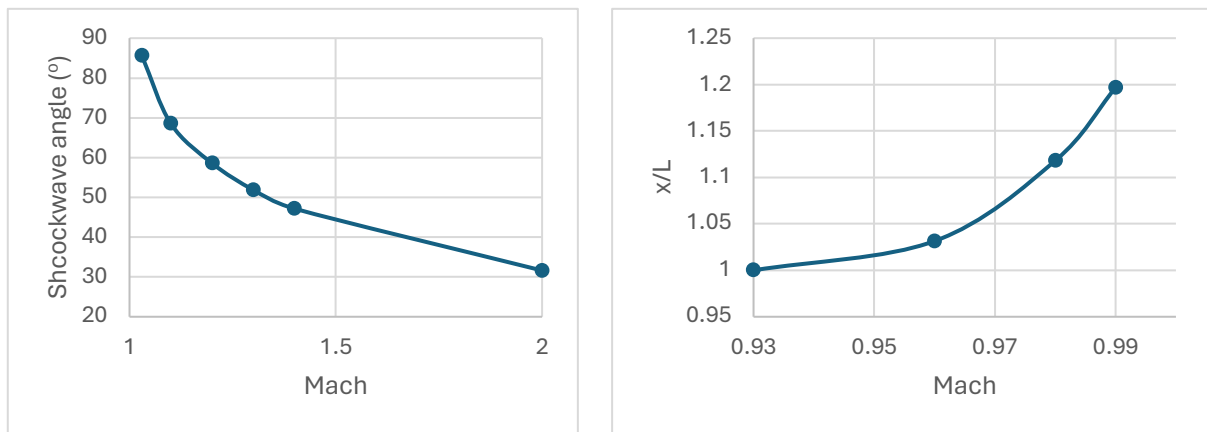


Figure 50 – Shockwave angles vs Mach number(left), Shockwave location vs Mach number (right)

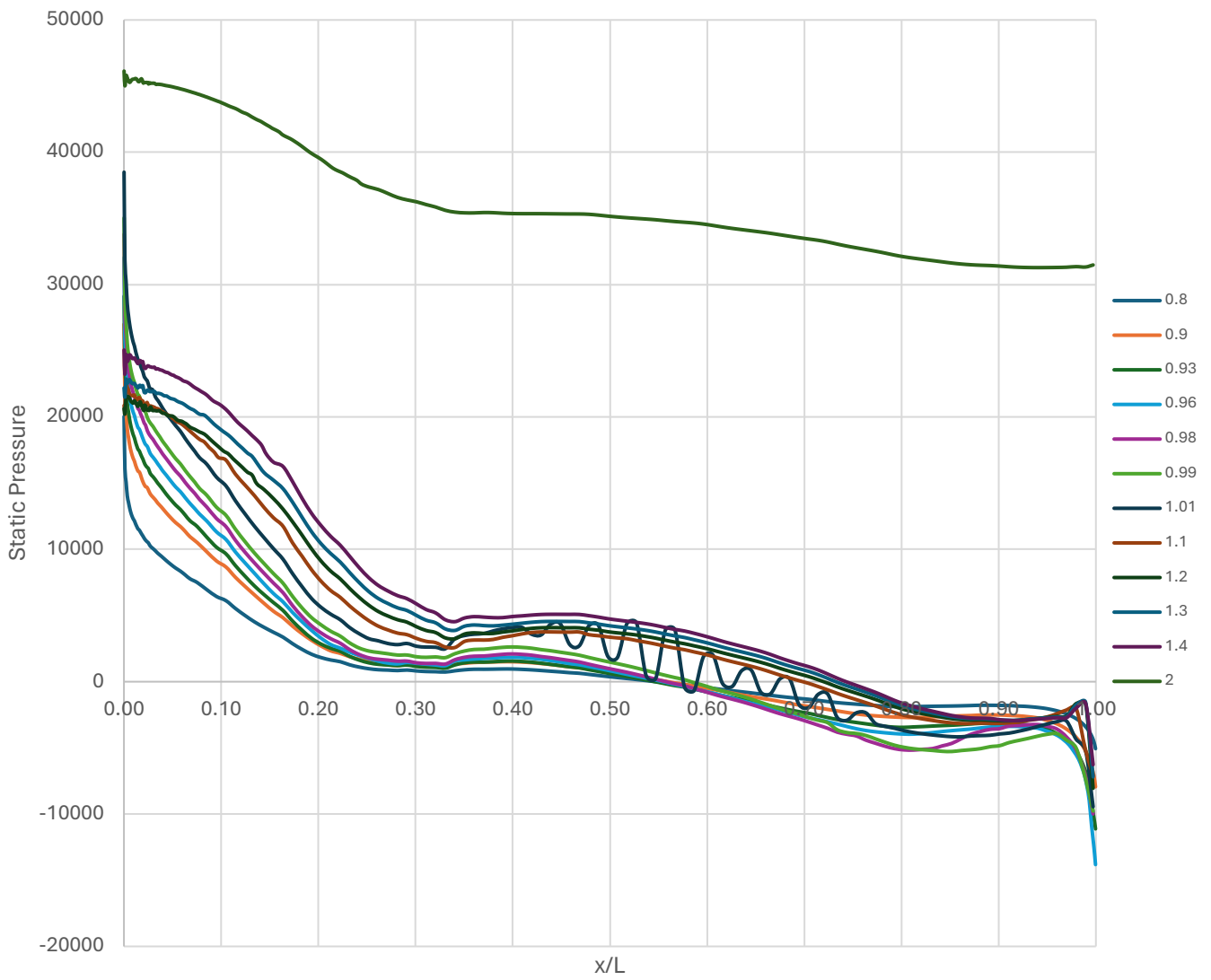


Figure 51 – Static pressure against  $x/L$



Figure 54: Mach contours for freestream  $M = 2.0$



Figure 53: Pressure contours for free stream  $M = 2.0$

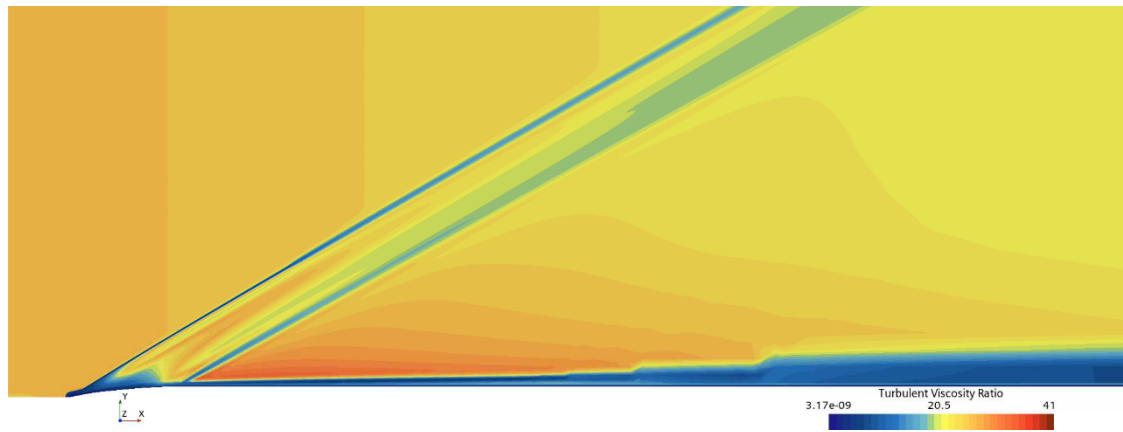


Figure 52: Turbulent viscosity ratio contours for  $M = 2.0$

Contour plots for  $0.8 < M < 1.4$  can be found in appendix D.

### 5.4.4 3D

In order to have a representation of the performance of the rocket as a whole, a scale model of the rocket has been developed for numerical analysis. While a model of such scale would require a mesh size above what is capable within the limitations of this analysis to accurately resolve the complex flow field around the rocket in supersonic flight, an analysis in the compressible regime without shockwaves can be conducted. The rocket nose cone, body tube and 3 fin section will be modelled for comparison with the experimental data via the low speed wind tunnel, as well as the regime of  $0.2 < M < 0.8$  to bridge the gap between other studies within this report.

The rocket is placed in a cylindrical volume spanning 10 nosecone lengths upstream, 30 downstream and a radius of 10 lengths. While a hexahedral mesher is the preferred grid as previously mentioned, due to the complexity and size of the domain, a hexahedral mesh could not be reasonably achieved with the resources available. As such a polyhedral mesher was implemented which while more computationally and memory intensive, provides a better mapping of the surface geometry with a smaller number of cells, as well as generally converging in less iterations than a hexahedral mesher. Similar best practices were followed as with the axisymmetric case to increase the resolution of the mesh in key areas. This was done predominantly near the stagnation points at the leading and trailing edges of the rocket parts, as well as at the transition of the nose cone to the body where a pressure gradient can be observed. As the body is now a finite length, further refinement is required in the region behind the rocket as a region of flow separation is expected. Moving away from the rocket surfaces a volumetric growth rate is applied so as to not refine the mesh in uniform areas.

Similar prism layering is applied to the rocket surfaces with the total thickness of the layers growing in the streamwise direction. The mesh again aims for a low wall  $Y^+$  treatment in the magnitude of 1. As the chosen schemes had previously proved successful in the supersonic flow, the methods used in these calculations will remain mostly the same with the exception of the change to a 2<sup>nd</sup> order implicit central scheme as disturbances will now be transported upstream since the flow is no longer supersonic. Additionally the inlet condition has been changed from a stagnation inlet to a velocity inlet to match the specification from the dataset in 17.

*Table 19 – Mesh properties*

Chosen prism layer total thickness (mm)	Number of prism layers	Wall thickness specification (mm)
0.25 – 7.5	35	$1.5478246 \times 10^{-3}$

Table 20 – Boundary conditions

Boundary	Specification	Values
Inlet	Velocity inlet	Velocity: 13.2 – 273.12 Temperature: 296.15 Atmospheric pressure: 101325 Pa
Outlet	Pressure outlet	Pressure: 101325Pa Temperature: 296.15 K
Radial surface	Symmetry Plane	Slip condition
Rocket	Wall	No Slip condition Adiabatic Condition Smooth surface
Number of Cells	Polyhedral	5617656
Re		$4 \times 10^6$

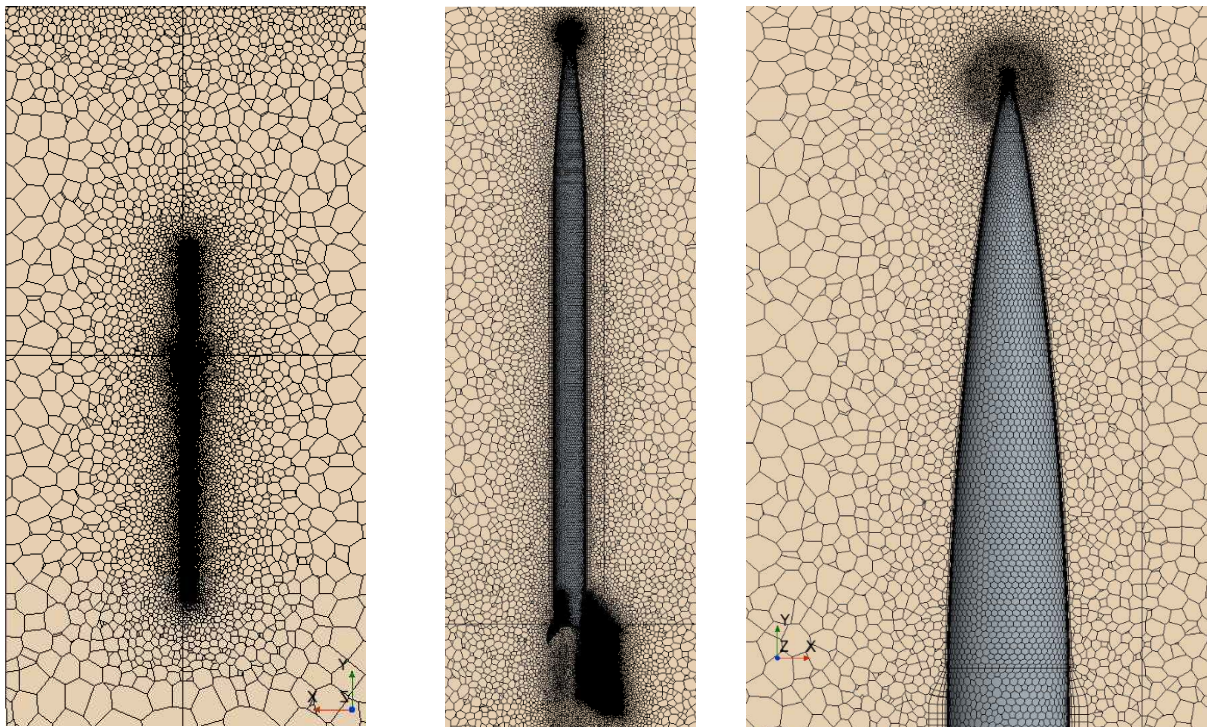


Figure 55 – Leading edge mesh

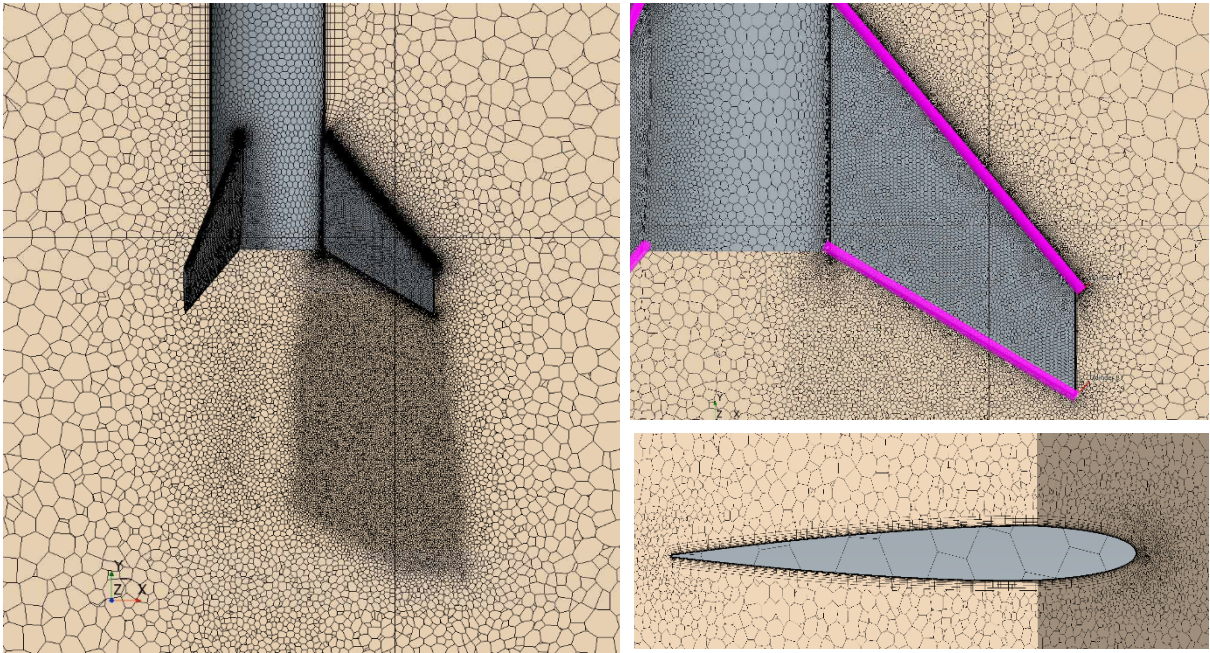


Figure 56 – Trailing edge mesh

## Results

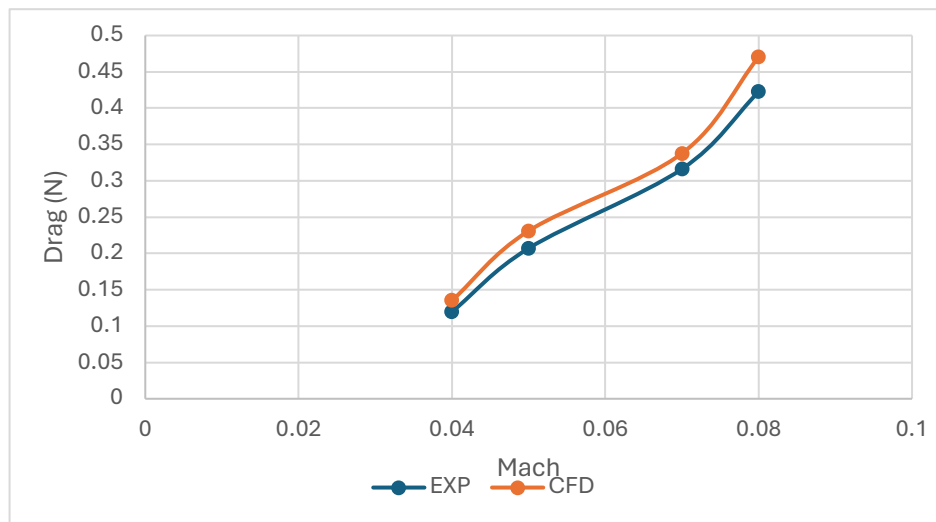


Figure 57 – experimental (experimental data contributed by Paula) vs cfd Drag

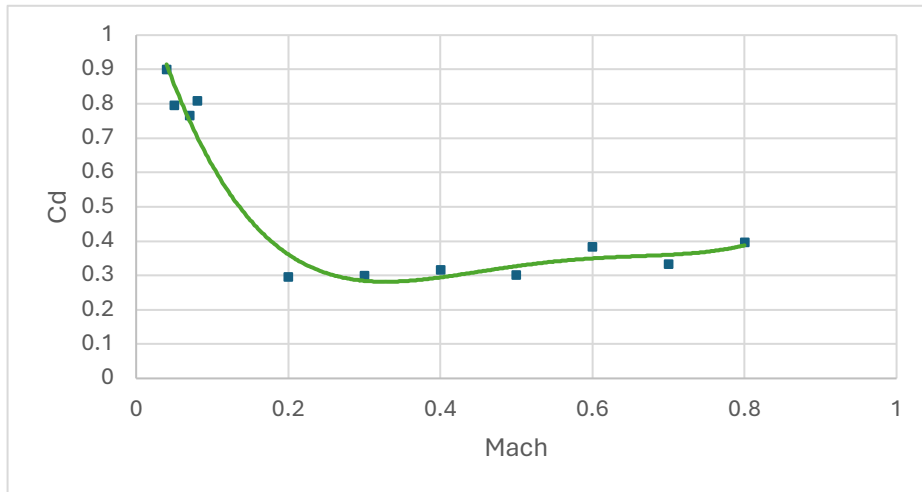


Figure 58 – Cd vs Mach

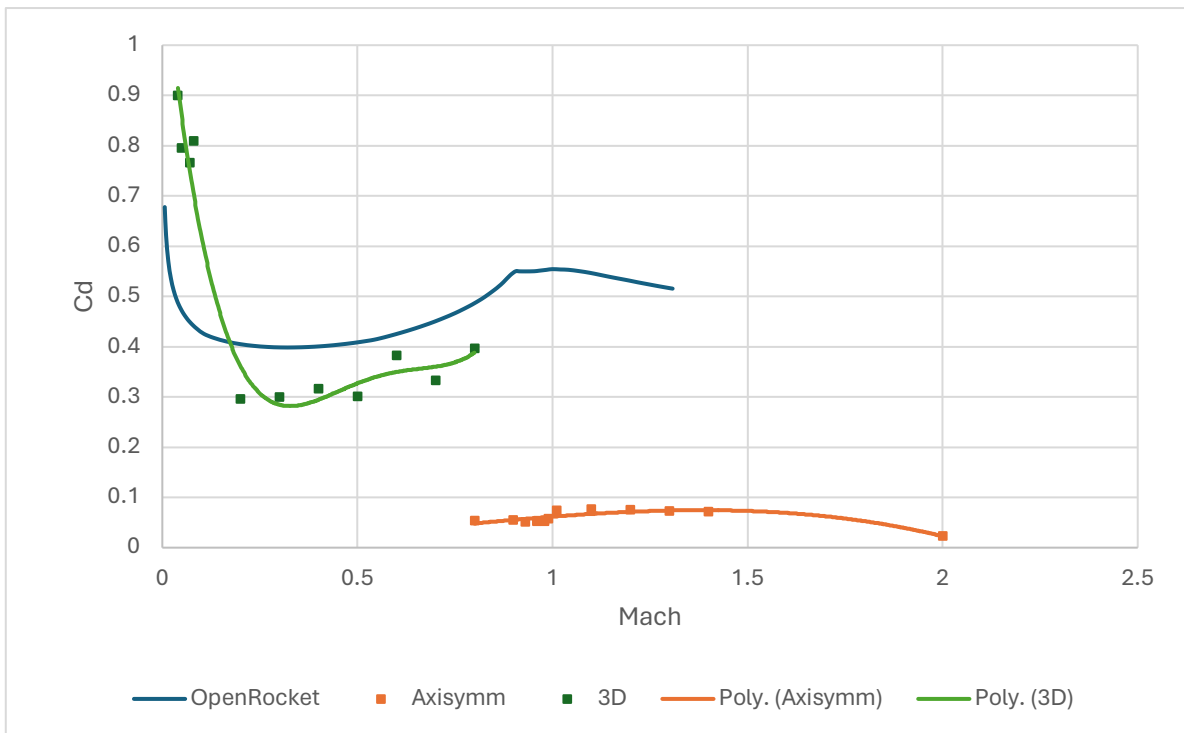


Figure 59: Cd vs Mach by computational methods as compared to OpenROcket (Open rocket data contribution by Ruben)

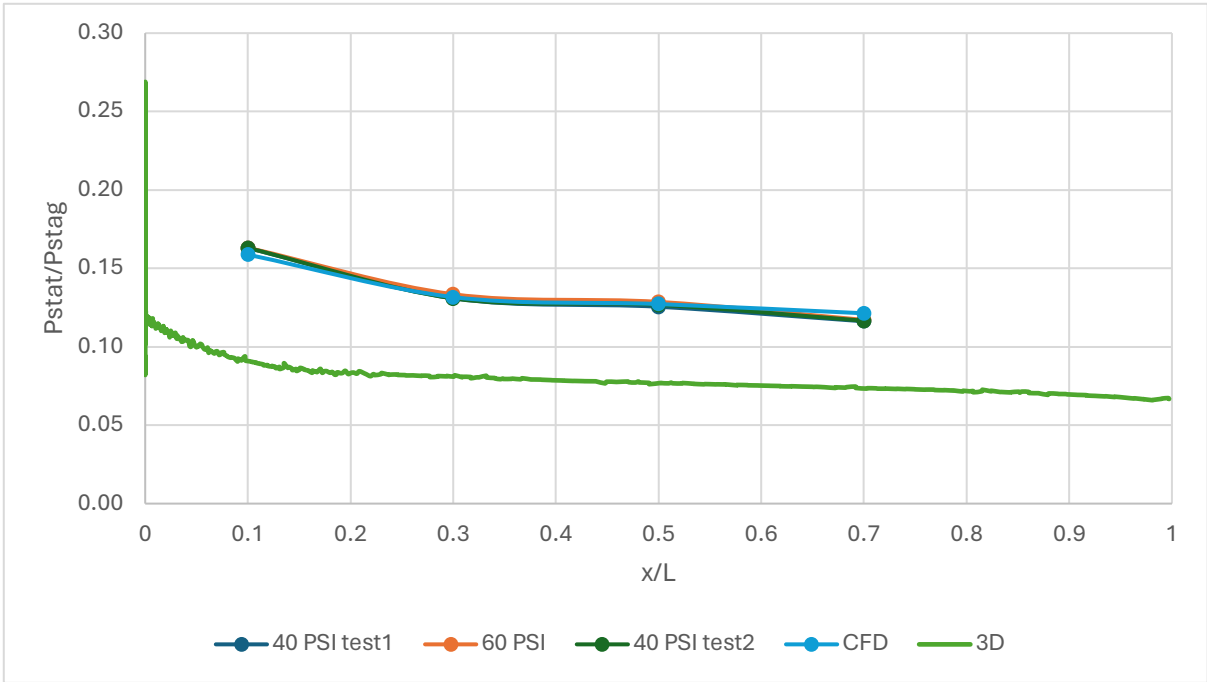


Figure 60: 3D CFD Pstat/Stag compared to previous data

Table 21 – Cp vs Mach

Mach	CP (m) from leading edge
0.04	0.767
0.05	0.812
0.07	0.795
0.08	0.799
0.2	0.755
0.3	0.754
0.4	0.803
0.5	0.786
0.6	0.645
0.7	0.742
0.8	0.738

Table 22 – Open rocket vs CFD

CFD	OpenRocket (Contributed by Ruben)	% Difference
0.763273	0.674	11.7

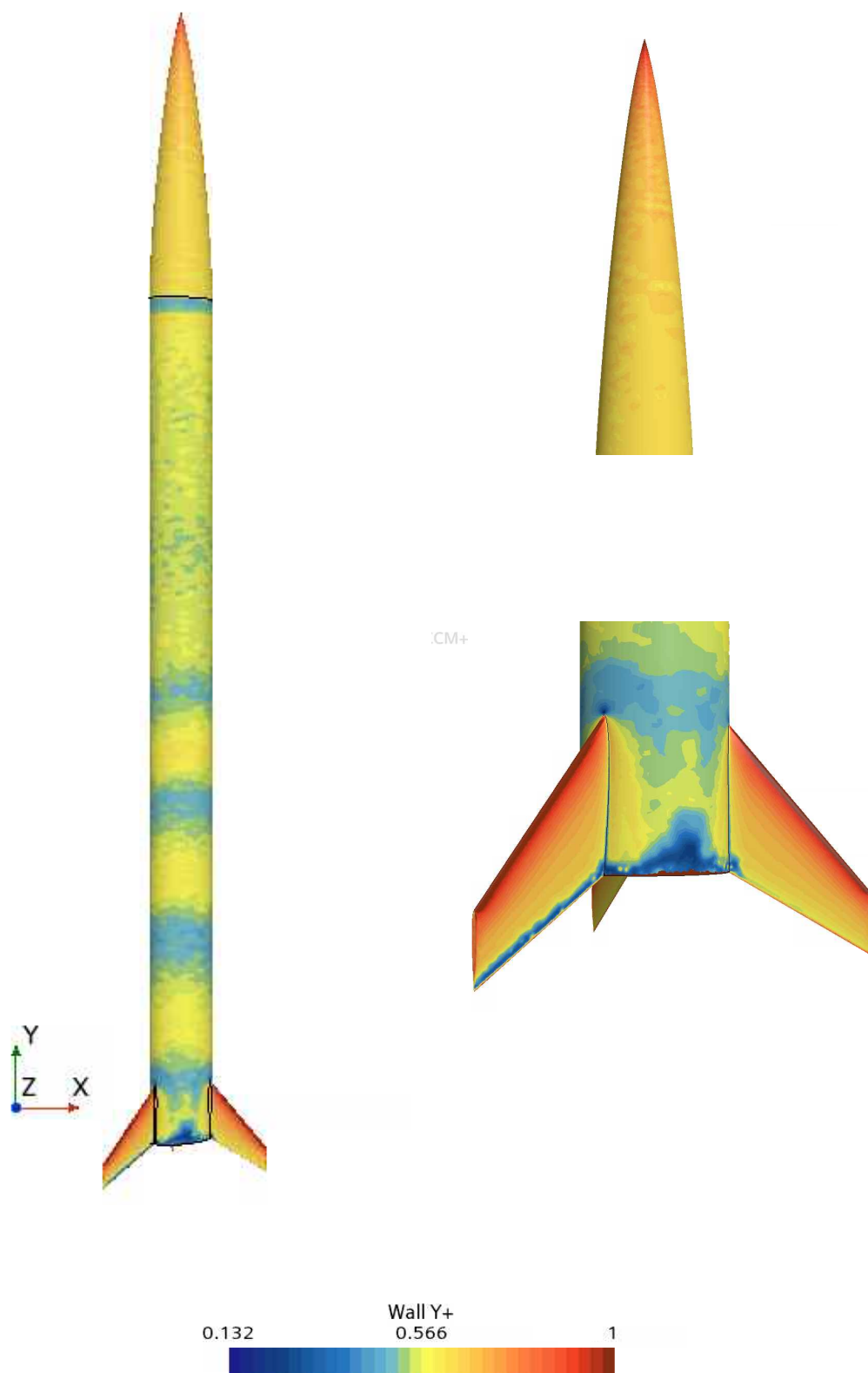


Figure 61: Wall Y+ for 3D rocket

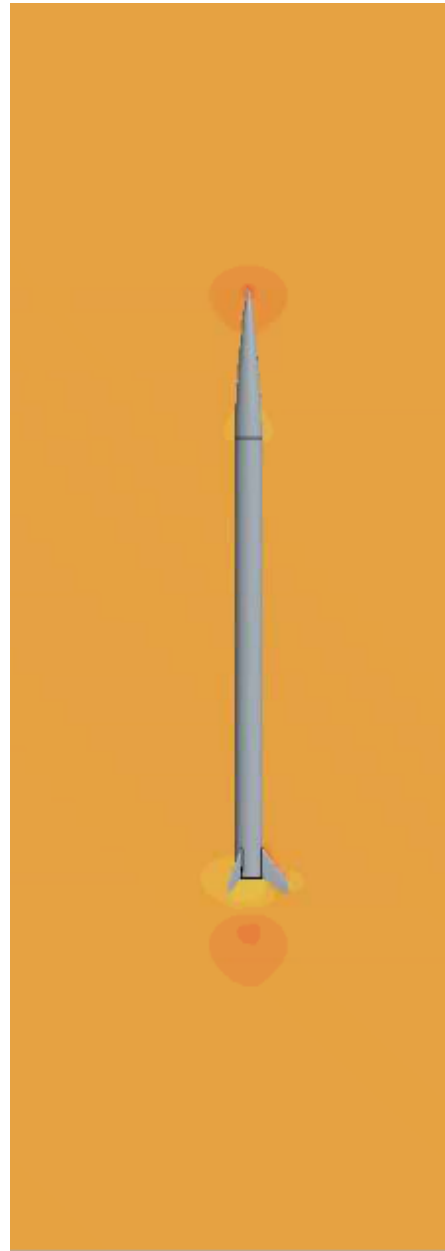
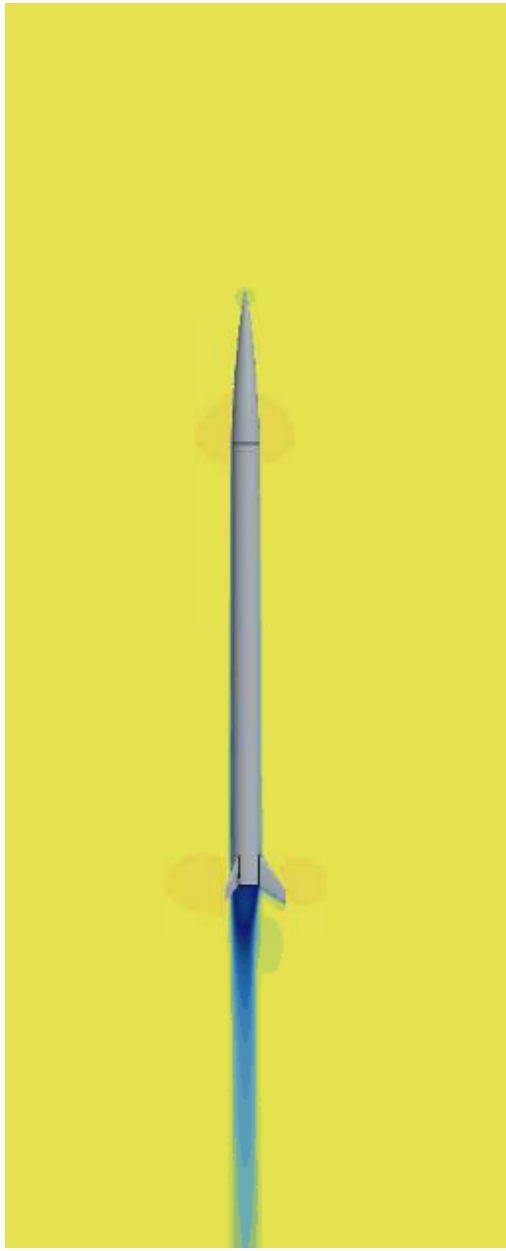


Figure 62 Mach and Pressure coefficient contours for  $M = 0.8$

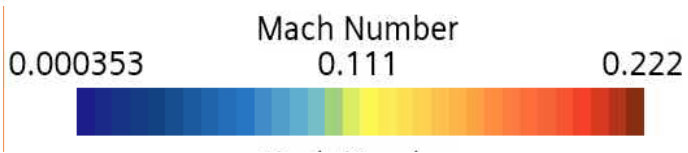
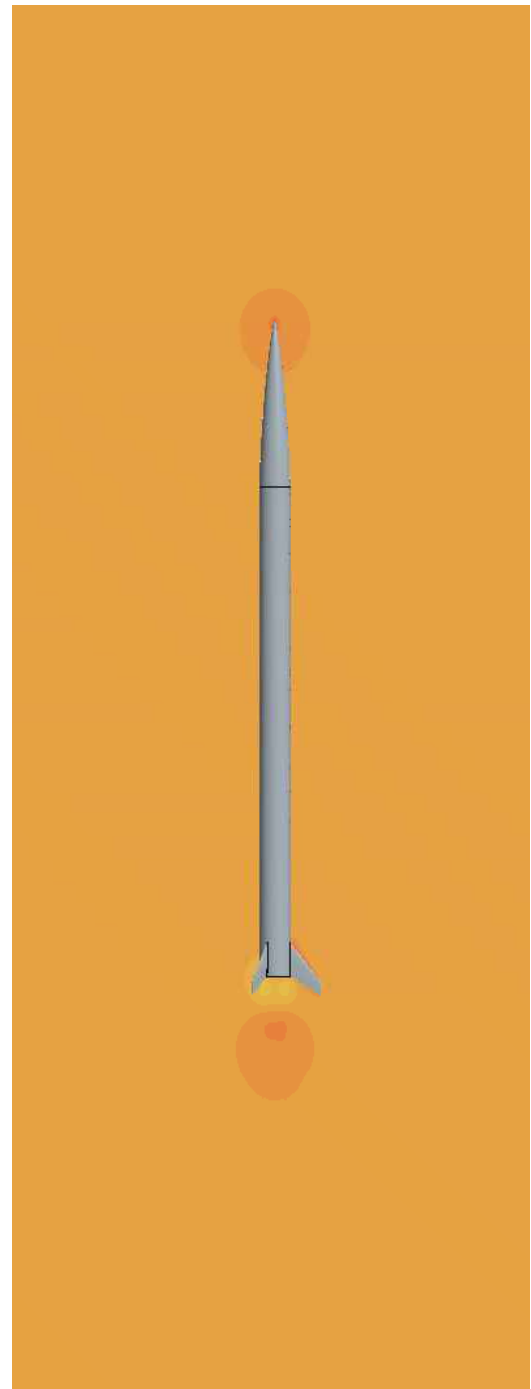


Figure 63: Mach and pressure coefficient plots for  $M = 0.2$

Further contour plots can be found in Appendix E

## LES

Having proven its ability to accurately capture the flow field, the case of the Axisymmetric model has been chosen to conduct a transient calculation of 3D Von Karman nose cone. The solver chosen is a wall modelled LES solver using the CABARET upwind method with GPU acceleration. snappyHexMesh was used to generate a hexahedral mesh with refinement regions as dictated by the axisymmetric RANS and Schlieren photography in order to be able to properly resolve the gradient over the shockwave and resolve turbulence scales which it will cause. The grid spans 10 nose cone lengths upstream, and 20 lengths in all other directions to produce a mesh of 66 Million cells. The mesh is based upon a cartesian base mesh on which the rocket geometry is cut out and cells are split into hanging nodes along the surface and conical refinement regions, then the solver was run on an NVIDIA A100 GPU with 80GB for approximately 12 hrs. Boundary conditions are as described in the axisymmetric case. As with an explicit asynchronous time stepping method is used with an automated CFL.

Table 23 – Mesh properties

Expansion Ratio	Number of prism layers	Wall thickness specification (mm)
1.2	4	$3.2 \times 10^{-2}$

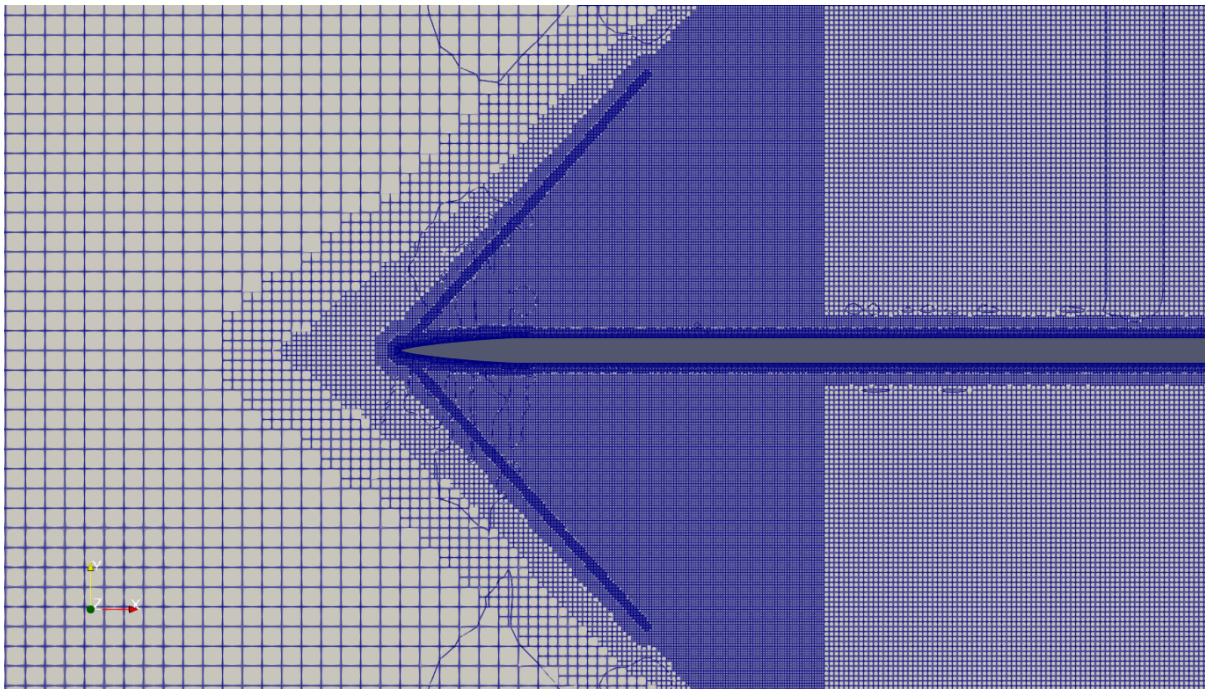


Figure 64: snappyHexMesh of rocket nose cone

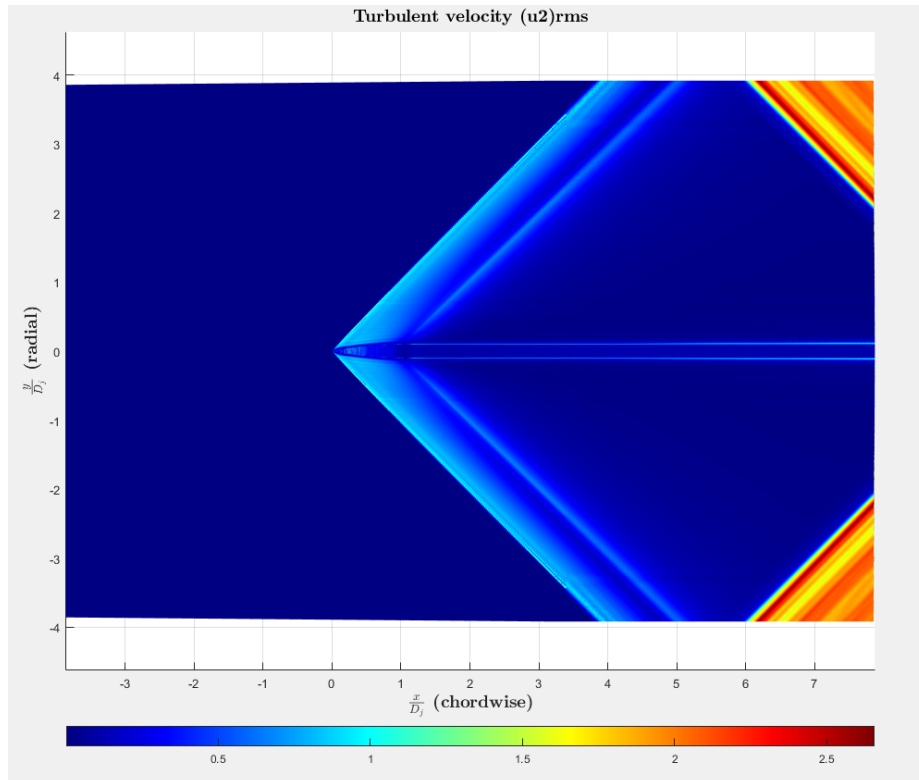


Figure 65 – Turbulent velocity field (RMS)

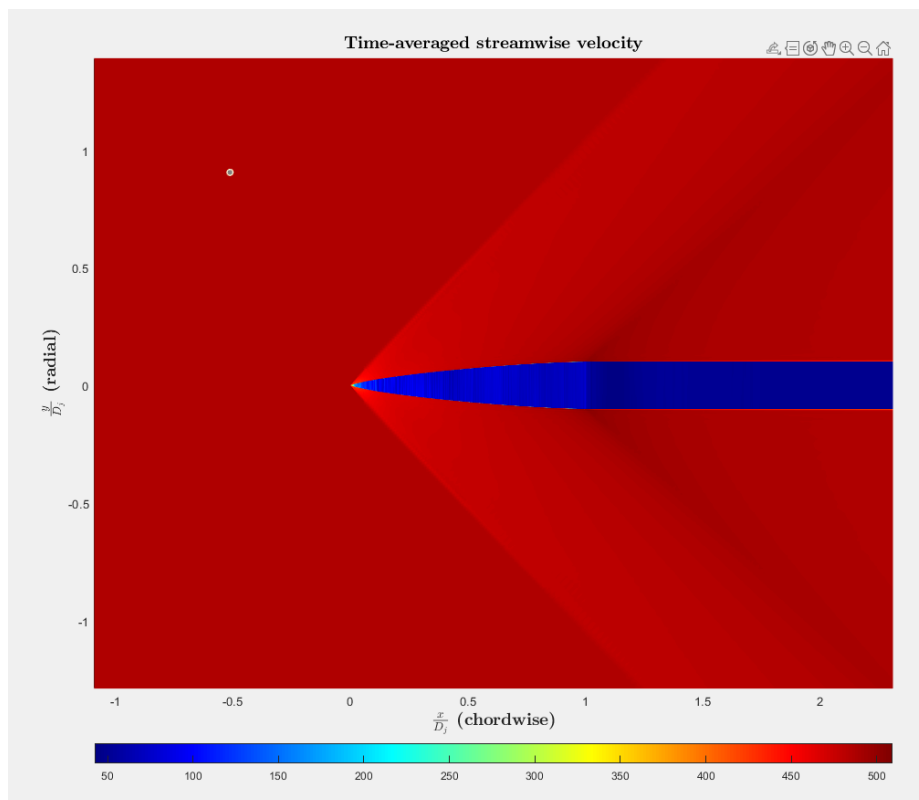


Figure 66 – Time averaged velocity field

## 6. Discussion

The low-speed wind tunnel experimental data showed that the 3-fin and the 4-fin configuration experienced very similar coefficients of drag at a yaw angle of  $0^\circ$ , meaning that the additional fin would not impact drag significantly if the rocket was travelling in stable conditions. This result suggests that at a  $0^\circ$  yaw angle, the airflow around the fins was relatively undisturbed, which would result in comparable drag coefficients for both configurations.

*Figure 28* also demonstrates that the 3-fin model experienced the lowest coefficient of drag when set at a yaw angle of  $6^\circ$ . This could be attributed to the specific aerodynamic characteristics as it shows that the 3-fin configuration resulted in improved flow control and reduced drag at this angle in comparison to the 4-fin model.

The steady increase in  $C_D$  with increasing yaw angle seen for both fin models' graph plots (see *Figure 30*) – with steeper gradients where the yaw angles  $> 2^\circ$  – indicates that yaw angles have a significant impact on a rocket's aerodynamic performance (Chin, Cheng, Mansor, & Baru, 2018). This observation is consistent with the expected behaviour of a rocket that experiences slight changes in yaw, where the side force seems to increase with yaw angle, leading to higher drag. Overall, the conclusion drawn from the observations seen on the drag coefficient graphs, show that the better option between both configurations was the 3-fin.

Looking at the graph plot for CL on *Figure 33*, it is evident that both the 3-fin and the 4-fin configuration produce lift (upward force) at higher speeds shown by the positive gradient from both configurations. The variations in CL between the 3- and 4-fin configurations at a  $0^\circ$  yaw angle imply that the rocket's lift characteristics are dependent on the number of fins.

The 4-fin model initially experiences larger positive lift than the 3-fin showing there were variations in fin geometry or airflow interaction. Specifically, the 4-fin configuration has a larger aspect ratio than the 3-fin configuration which can significantly impact the generation of lift due to its ability to generate more lift-induced airflow circulation. Therefore, the 4-fin configuration experiences the most lift as the yaw angle and speed increases, as seen on *Figure 33*.

Interestingly, even though the 3-fin configuration appears to be the configuration yielding the least amount of lift, it shows a more gradual positive gradient at lower speeds. The 4-fin configuration at the lowest speed presents the gentlest positive gradient, indicating more control authority, and is the configuration that experiences the least amount of lift.

This shows that the 4-fin configuration provides more control authority – or in other words: the degree of control the rocket has on its trajectory – meaning the rocket will be able to perform more precise manoeuvres, however, also meaning that it will be more prone to deviate during flight. In light of these observations, the conclusion drawn was that the 4-fin configuration despite offering

more control authority, will induce more deviations than the 3-fin configuration. The findings indicate that the 3-fin configuration, once again, presented the best option for this project.

For the data compiled of Torque X, Torque Y and Torque Z, against the increasing speeds and yaw angles. For torque X (roll) plotted against speed (see *Figure 67* – Appendix A), every design shows a positive gradient, meaning that as speed increases, roll torque increases as well. The largest torque, increasing almost linearly, is experienced by the 4-fin design at a 6-degree yaw angle implying that the extra fin might strengthen the forces of aerodynamics that contribute to roll torque at this yaw angle. Although it fluctuates, the 3-fin arrangement at a 6-degree yaw angle likewise exhibits an increase in torque. This might be the result of sporadic variations in roll torque caused by differences in airflow surrounding the fins. Configurations with 0-degree yaw angles exhibit practically horizontal lines on the graph, which represent negligible roll torque. This implies that when the airflow is parallel to the rocket's longitudinal axis, the rocket experiences little or no roll motion.

For the data compiled and plotted for torque Y (see *Figure 68* – Appendix A), similar positive gradients are seen in all configurations, again suggesting that pitch torque increases with speed. Pitch torque is maximum in the 4-fin configuration at a 6-degree yaw angle and lowest in the 3-fin configuration at the same angle. This implies that at different yaw angles, the extra fin may have a variable effect on the aerodynamic forces causing pitch torque.

Lastly, for the data compiled and plotted for torque Z (see *Figure 69* – Appendix A), most setups exhibit a negative gradient, which means that as speed increases, yaw torque decreases. The 3-fin at 0-degree yaw angle is an exception; it shows a graph with minimal negative gradient, making it practically horizontal. This indicates that there is little yaw torque at this yaw angle, most likely because of balanced aerodynamic forces due to experiencing aligned airflow. At 6-degree yaw angles, the 3-fin and 4-fin arrangements exhibit noticeably larger negative gradients, which suggests stronger yaw torque and steeper speed drops. This would be due to asymmetrical airflow patterns and higher aerodynamic loads on the fins, which result in amplified yawing moments.

The supersonic testing of the Von Karman nose cone showed first that the model could produce consistent and repeatable readings of the surface pressure distribution on the nose cone. Readings were taken with several supply pressures providing a constant pressure ratio suggesting that the manufacturing and reading methods produced valid results. The pressure distribution suggests a larger expansion effect over the first and last quarter span of the nose cone length as compared to the distribution across the middle section. Overall, the ogive curve produces a gradual expansion reducing energy losses to thermal effects and maintaining an almost constant entropy after the shockwave. Schlieren photography shows an attached oblique shockwave and no distinct expansion fans over the nose cone. This suggests that the drag on the nosecone is likely shear dominant, and

no clear disturbances can be noticed along the surface of the nosecone suggesting the flow remains attached passed the nose cone, reducing parasite drag.

The surface distribution along the nose cone is compared to that obtained by the RANS axisymmetric model with a disagreement of sub 5%, additionally the shockwave angle error was 1.35%. This shows excellent agreement between experimental and computational data suggesting that the meshing and methods chosen through CFD were suitable for this flow regime. In combination the experimental and computational data can be used to identify a drag coefficient for the nose cone which is comparable to previous literature. The lead time for experimental testing was in the magnitude of 4 months whereas the CFD calculation was able to produce converged results in under an hour. While the need for a validation model is key, it has proven that the method used can be used for a larger analysis while reducing lead times.

Further extending the application of the model into the transonic regime, a critical Mach number of 0.93 has been approximated, which is higher than traditional nose cones and aerofoils. The model showed good overall agreement however was slightly unstable when approaching the speed of sound suggesting a URANS model or other transient solve may be necessary in this regime.

3D modelling of the rocket showed a degree of agreement with experimental testing as previously mentioned in the low-speed wind tunnel. The chosen methodology slightly overpredicted the forces experienced by the rocket. This is partially due to slight indecencies between the scale of the meshed rocket as compared to that of the experimental method. In comparison with data from Open Rocket in the subsonic regime, the absolute value was of a large magnitude of disagreement however the trend followed almost identically. This could be due to the conditions in which reference values were assumed as OpenRocket uses standard atmosphere values but is not completely clear on the values used. As the agreement with the experimental testing at low speed was within tolerance, this could suggest that the k- $\epsilon$  model failed to predict a degree of flow separation which would have increased the drag.

The centre of pressure was also calculated from the CFD model and remained constant with slight fluctuations through the subsonic regime. When compared to data from OpenRocket the calculation predicted a  $C_p$  further from the nose cone, while the calculated nose cone is a more realistic approximation as the swept fin section and aerodynamic body would lead to the  $C_p$  expecting to be almost within the fin section. Never the less, even if the smaller OpenRocket value is taken, it is still suitably behind the CG suggesting the rocket is stable within the flight envelope.

Additionally, the axisymmetric nose cone model was progressed onto a transient solver in which the turbulent and mean velocity were resolved. The calculation showed agreement with the axisymmetric case to a significantly higher resolution, however no additional flow separation was observed further supporting the results from the first two cases, and the use of the k- $\epsilon$  model. Figure

65 shows the large disruptive nature of the shockwaves to a CFD calculation as the shockwave can be seen reflecting on the boundaries. This was not seen in the STARCCM models suggesting it has a much more diffusive scheme than used with the WMLES CABARET method.

## 7. Conclusion

The proposed design utilizes a fiberglass body tube with a simple 3D printed ABS plastic nose cone. The TeleMetrum flight computer was chosen for its compact size and ease of use for collecting basic flight data like altitude and Mach number. A CO2 deployment system was selected for its cleanliness and reliability at high altitudes. The recovery system utilizes a 24-inch nylon ripstop parachute for a safe and controlled descent.

The analysis of the expected flight trajectory indicates that the rocket design with either 3 or 4 fins will achieve the desired apogee with a maximum Mach number of approximately 1.3. While the 3-fin design offers a slight performance advantage in reaching a higher maximum Mach number, the 4-fin design may provide increased stability.

Considering the findings for the ATI program torque readings and processed data, it appears that, overall, the 4-fin configuration proved to exhibit the best control authority compared to the 3-fin configuration, making it the best option for applications such as missile systems. However, the ultimate choice would depend on the mission requirements. This project required a rocket that would maintain its vertical path without relying on electronic countermeasures for deviation correction. Therefore, as proved by the previous findings, the suggestion for the final design configuration would be 3 fins because it would produce the least deviations.

A reliable Von Karman  $\sim 0.5$  scale replica of the nose cone was manufactured showing accurate and repeatable tests. Schlieren photography showed a shockwave angle of  $31.2^\circ$  and a pressure ratio in the magnitude of 0.16 was observed over the shockwave. Steady RANS,  $k-\epsilon$ , Axisymmetric calculation showed great agreement with the experimental model as well as with previous literature and analytical models at Mach 2.0. 3D calculation showed fair agreement with low speed testing in the magnitude of 10% error but did not agree in magnitude to data obtained by OpenRocket, only achieved agreement by trend. The  $k-\epsilon$  model seemed able to model the flow near the nose cone as 3D and axisymmetric data was in agreement for an isolated nosecone however the model could have failed to predict flow separation further downstream. The centre of pressure obtained through steady state calculation provided a  $C_p$  location of 0.763m from the leading edge. The turnover for an experimental supersonic model was approximately 4 months, with 12hrs for a LES calculation, 3 hrs for a 3D rocket mesh and  $< 1$ hr for the axisymmetric case suggesting that the RANS axisymmetric model is a accurate and rapid solution to a rocket flow problem.

## 8. Suggestions for future work

As mentioned in the low-speed wind tunnel testing section, using sophisticated, computerised equipment that can detect airflow characteristics precisely and automatically (electronic manometer), would reduce parallax error, which would result in more accurate measurements and calculations, and minimise the need for manual corrections. Moreover, pressure tapings should be drilled along the length of the model rocket inside the wind tunnel to measure the pressure difference over multiple sections of its surface to enhance the accuracy of the results.

Testing of the recovery system would provide more insight into the aerodynamics of the parachute and the ejections systems complete functionality Deployment of the parachute under a load equivalent to the rocket would enable precise measurement of descent rates, facilitating potential optimizations in parachute size for weight reduction. In addition, it would be possible to evaluate the parachute under different wind speed conditions and angles.

Finite element analysis (FEA) could be used for evaluating how certain components, such as the fins and the body tube, will respond to forces and stresses when in flight. This would be useful to identify weak points in our design and give us an understanding on which components need to be reinforced. Furthermore, FEA can be used to assess steady state thermal analysis. This can be used to determine the temperature distribution on the rockets body.

Finally simulation of the rocket burn faze could be conducted in order to account for the larger taper of the trailing edge caused by the high pressure jet decreasing the  $C_d$  during a crucial phase of flight. This would provide more accurate data for future launches however the facilities do not currently allow for testing or propulsion combustion.

# References

- Aliabadi, A. A. (2022). *Turbulence* (1 ed.). Springer.
- Anderson, J. D. (2016). *Fundamentals of fluid dynamics* (4th ed.). McGraw Hill.
- Annual number of objects launched into space.* (2024, January 4). Retrieved from Our World in Data: <https://ourworldindata.org/grapher/yearly-number-of-objects-launched-into-outer-space>
- Benson, T. (n.d.). *NASA(.gov)*. Retrieved April 19, 2024, from <https://www.grc.nasa.gov/www/k-12/VirtualAero/BottleRocket/airplane/rktparts.html>
- Braeunig, R. A. (2020). *Rocket and Space Technology*. Retrieved February 2024, from [http://www.braeunig.us/space/aerodyn\\_wip.htm#:~:text=Form%20drag%2C%20skin%20friction%20drag,tip%20of%20an%20aircraft's%20wing.](http://www.braeunig.us/space/aerodyn_wip.htm#:~:text=Form%20drag%2C%20skin%20friction%20drag,tip%20of%20an%20aircraft's%20wing.)
- Bunkling, J. A. (2022). *Design Analysis of Rocket Tail Fins Aimed at Higher Apogee by Computer Simulation*. Newark, New Jersey: s.n.
- CATS. (2024). *CATS User Manual*. Retrieved April 20, 2024, from <https://www.catsystems.io/downloads>
- Chin, K., Cheng, S. Y., Mansor, S., & Baru, P. (2018). Yaw Angle Effect on the Aerodynamic Performance of Hatchback Vehicle Fitted with Combo-Type Spoiler. *Malaysian Journal of Fundamental and Applied Sciences*, 1-11.
- Cruchet-Pasos, G. (2023). *Effect of Fin Geometry on the Aerodynamic performance of an N-class sounding Rocket at Subsonic flight*. London: Queen Mary University of London.
- Davidson, L. (2022). *An Introduction to Turbulence Models*. Gotegorg, Sweden: Chalmers University of Tehcnology.
- Finio, B. (2024). *Diagram of stable and unstable rockets - Science Buddies*. Retrieved from <https://www.sciencebuddies.org/image-credit?id=15668>
- Garbee, B., Packard, K., Finch, B., & Towns, A. (2016). *An Owner's Manual for Altus*. Retrieved April 20, 2024, from [https://www.apogeerockets.com/downloads/PDFs/AltusMetrumUserManual\\_20160904.pdf](https://www.apogeerockets.com/downloads/PDFs/AltusMetrumUserManual_20160904.pdf)
- Gary, A., & Crowell, S. (1996). *The Descriptive Geometry of Nose Cones*.
- Gatski, T., & J.P., B. (2008). *Compressibility, Turbulence and High Speed Flow*. Elsevier.
- Gregorek, G. M. (1970). *Aerodynamic drag of model rockets*. Penrose: Estes Industries.
- Grumman, R. H., Roman, D., & Rajkovic, D. (1997). *Drag: An Introduction*. Dragbusters.
- Hall, N. (2021). *National Aeronautics and Space Administration: Isentropic flow*. Retrieved April 2024, from <https://www.grc.nasa.gov/WWW/K-12/airplane/isentrop.html>
- Hart, R. G., & Katz, E. R. (1949). *NACA ARML913: Flight Investigations at High-subsonic, Transonic, and Supersonic Speeds to determine Zero-Drag of Fin-stabilised Bodies of Revolution having Fineness*. Washington: Nationa Advisory Committee for Aerodynamics.
- Heister, S. D., Anderson, W. E., Pourpoint, T. L., Cassady, J., & Cassad, R. J. (2019). *Rocket propulsion*. Cambridge University Press, 47(1).

- Heister, S., Anderson, W., Pourpoint, T., Cassady, J., & Cassady, R. (2019). *Rocket Propulsion*. Cambridge: Cambridge University Press.
- J, L. (2014). *What is Aerodynamics?* Retrieved April 20, 2024, from <https://www.livescience.com/47930-what-is-aerodynamics.html>
- Jones, R. T. (1956). *Theory of Wing-body Drag at Supersonic Speeds*. Langley: NASA.
- Kundu, P. K., & Cohen, I. M. (2004). *Fluid Mechanics* (3 ed.). San Diego: Elsevier Academic Press.
- Lopes, Á. (2021). *EUROPEAN ROCKETRY CHALLENGE DESIGN, TEST & EVALUATION GUIDE*. Portugal Space.
- Lucas, J. (2014, September 20). *What is Aerodynamics?* Retrieved from LiveScience: <https://www.livescience.com/47930-what-is-aerodynamics.html>
- Maarson, B. (1954). *The calculation of the wave drag of a family of low drag axisymmetric nose shapes of fineness ratio 4,5 at zero incidence at supersonic speeds*. Cranfield: The College of aeronautics, Cranfield.
- Marciniak, V. (2016). *Phenomenological Transition Modelling for Turbomachinery Flows*. Bocum: Fakultat für Maschinenbau der Ruhr-Universität Bochum.
- MatWeb. (2024). *MatWeb Material Property data*. Retrieved April 20, 2024, from <https://www.matweb.com/search/GetReference.aspx?matid=166>
- Milligan, T. V. (2007, September 11). Basics of Dynamic Flight Analysis. *Peak Of Flight*.
- Milligan, T. V. (2012, January 31). Why should you Airfoil your Rocket's fins? *Peak Of Flight*.
- Milligan, T. V. (2017). The Different Rocket Recovery Techniques. *Peak Of Flight*, 1(447), 2-11.
- Milligan, T. V. (2018). Model Rocket Stability. *Peak Of Flight*, 414, 2-8.
- Minnesota, T., & Stroick, G. (2011, January). Retrieved April 21, 2024, from <https://offwegorocketry.com/userfiles/file/Nose%20Cone%20&%20Fin%20Optimization.pdf>
- NACA 0008. (2024, March). Retrieved from Airfoil Tools: <http://airfoiltools.com/airfoil/details?airfoil=naca0008-il>
- Newton, I. (1846). *Newton's Principia: the mathematical principles of natural philosophy*. New York: Daniel Adee.
- Newton, M. (n.d.). *National Association of Rocketry*. Retrieved April 19, 2024, from <https://nar.org/landing/building-rockets-preview-of-member-guidebook/>
- Niskanen, S. (2013). *Development of an Open Source model rocket simulation software*. Helsinki: HELSINKI UNIVERSITY OF TECHNOLOGY.
- Nouri, N., Mostafapour, K., Kamran, M., & Bohadori, R. (2014). Design methodology of a six-component balance for measuring. *Measurement* 58, 544–555.
- Nowak, R., Albertson, C., & Hunt, L. (1984). *Aerothermal tests of a 12.5 percent cone at Mach 6.7 for various Reynolds numbers, angles of attack and nose shapes*. Washington DC: NACA.
- Pektaş, A. D. (2019). Effects of different fin shapes on apogee and stability of model rockets. *International conference on recent advances in space technologies (RAST)*, 9, 193-199.

- Perkings, E., Jorgensen, L., & Sommer, S. (1958). *Investigation of the drag of various axially symmetric nose shapes of fineness ratio 3 for Mach numbers 1.24 to 7.4*. Washinton DC: NACA.
- Settlemier, A. M., & Motter, N. (2022). *CO2 Based Parachute Deployment*. Akron: The University of Akron .
- STAR. (2021). *Sizing Fins*. Retrieved April 20, 2024, from <https://rocketry.gitbook.io/public/tutorials/airframe/sizing-fins#fin-thickness>
- Stasko, M. (2022). *UN Office for Outer Space Affairs and United Kingdom launch new partnership on Registering Space Objects*. Retrieved April 22, 2024, from <https://unis.unvienna.org/unis/en/pressrels/2022/unisos574.html>
- Stine, G. H., & Stine, B. (2004). *Handbook of Model Rocketry 7th Ed*. Hoboken, New Jersey: John Wiley & Sons.
- Summerfield, M. (2013). *Solid propellant rocket research* (1 ed.). Princenton: Princeton University.
- Sutton, G. P., & Biblarz, O. (2001). *Rocket Propulsion Elements* (4 ed.). New York: John Wiley & Sons.
- tinderrocketry. (n.d.). *tinderrocketry*. Retrieved April 2024, 2024, from <https://www.tinderrocketry.com/peregrine-co2-ejection>
- Urzay, J. (2020). *The physical characteristics of hypersonic flows*. Stanford: Stanford University.
- Wang, M. (2021). Reflection of a moving shock wave over an oblique shock wave. *Chinese Journal of Aeronautics*, 5(34), 399-403.
- White, F. M. (2021). *Fluid Mechanics* (5 ed.). Mc Graw-Hill.

# Appendix A

*Table 24 - Averaged raw data collected with the ATI program for the 3-fin configuration*

		<b>Average</b>					
<b>SPEED mmH2O</b>	<b>YAW (°)</b>	<b>Force X (N)</b>	<b>Force Y (N)</b>	<b>Force Z (N)</b>	<b>Torque X (N-m)</b>	<b>Torque Y (N-m)</b>	<b>Torque Z (N-m)</b>
10.39	0	0.119671	0.101573	0.031936	-0.016490	0.041418	-0.000023
	2	0.150468	0.010378	0.053645	0.004615	0.046679	-0.012713
	4	0.158479	0.073992	0.107016	0.033883	0.042503	-0.031886
	6	0.147897	0.200069	0.137258	0.074486	0.024792	-0.061351
20.08	0	0.207117	0.020308	0.144360	0.007592	0.058943	-0.013441
	2	0.236996	0.070495	0.195626	0.048680	0.051392	-0.043900
	4	0.259006	0.131076	0.163554	0.073589	0.083409	-0.063246
	6	0.249361	0.315622	0.219564	0.141568	0.057970	-0.108658
29.78	0	0.316342	0.023781	0.206168	0.016078	0.087192	-0.019973
	2	0.335167	0.151339	0.246034	0.082380	0.084278	-0.067758
	4	0.345115	0.251689	0.235691	0.124116	0.111444	-0.100843
	6	0.360489	0.458516	0.280788	0.199666	0.084818	-0.153145
40.17	0	0.422623	0.029153	0.280631	0.020728	0.109282	-0.022785
	2	0.433282	0.228824	0.322943	0.116616	0.108593	-0.091342
	4	0.446594	0.521792	0.347192	0.224651	0.100526	-0.171018
	6	0.443769	0.653067	0.316408	0.279184	0.126245	-0.212802

*Table 25 - Averaged raw data collected with the ATI program for the 4-fin configuration*

		<b>Average</b>					
<b>SPEED mmH2O</b>	<b>YAW (°)</b>	<b>Force X (N)</b>	<b>Force Y (N)</b>	<b>Force Z (N)</b>	<b>Torque X (N-m)</b>	<b>Torque Y (N-m)</b>	<b>Torque Z (N-m)</b>
10.39	0	0.046472	0.101573	0.086477	0.040168	0.046579	-0.031804
	2	0.055056	0.010378	0.153827	0.021432	0.050482	-0.016513
	4	0.053628	0.073992	0.239137	0.050498	0.048103	-0.038190
	6	0.044495	0.200069	0.278672	0.097698	0.034774	-0.073179
20.08	0	0.129721	0.034666	0.230972	0.029731	0.072843	-0.026680
	2	0.149231	0.101210	0.266756	0.058437	0.085503	-0.049087
	4	0.160162	0.187197	0.292477	0.094352	0.103329	-0.075839
	6	0.144555	0.393074	0.385368	0.170789	0.064779	-0.134085
29.78	0	0.235584	0.046125	0.278395	0.043567	0.107871	-0.039407
	2	0.236488	0.259086	0.347112	0.123426	0.108531	-0.104771

	4	0.257008	0.355219	0.352259	0.162738	0.136238	-0.131870
	6	0.240145	0.593824	0.447153	0.251622	0.098236	-0.199551
40.17	0	0.342592	0.065010	0.334975	0.059921	0.147447	-0.055559
	2	0.337300	0.370248	0.397055	0.169957	0.140131	-0.144724
	4	0.348052	0.667534	0.490063	0.282772	0.118316	-0.228870
	6	0.352408	0.809848	0.486758	0.338066	0.142287	-0.272823

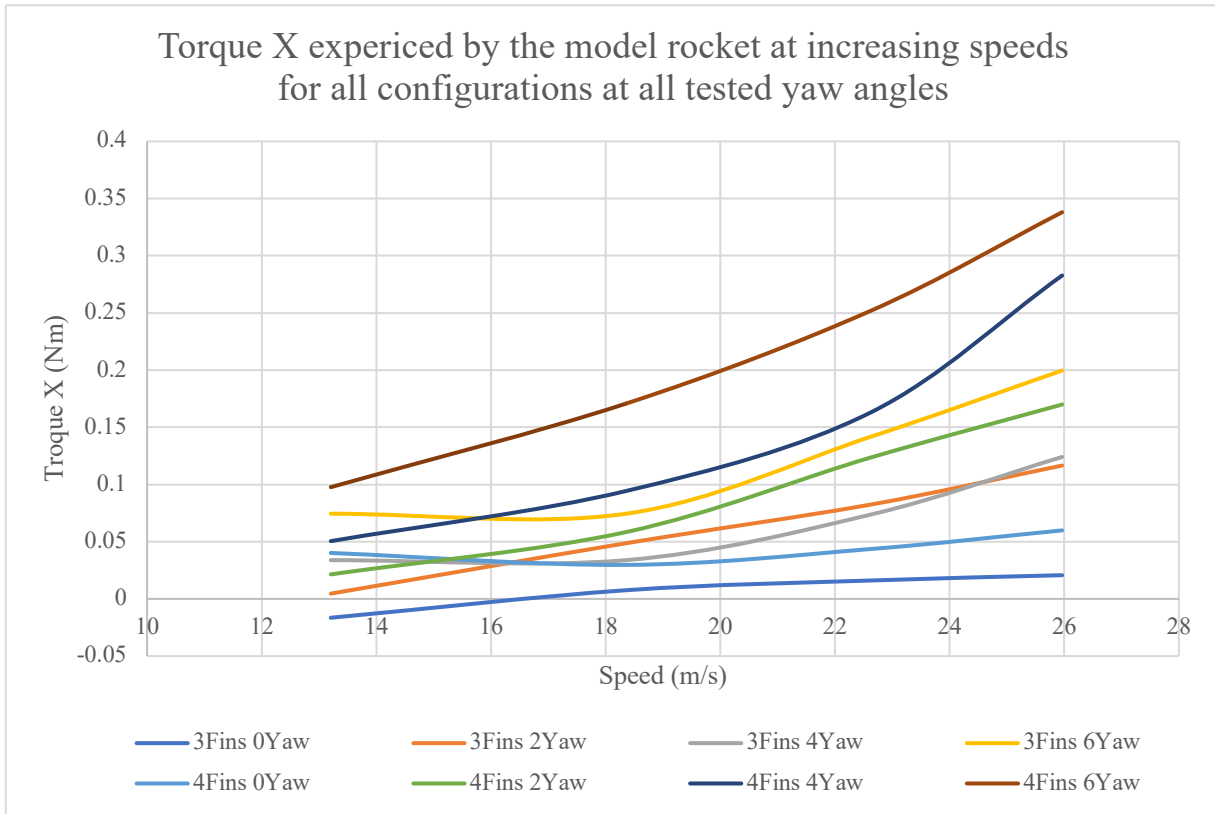


Figure 67 - Plotted data of the torque X experienced by the rocket

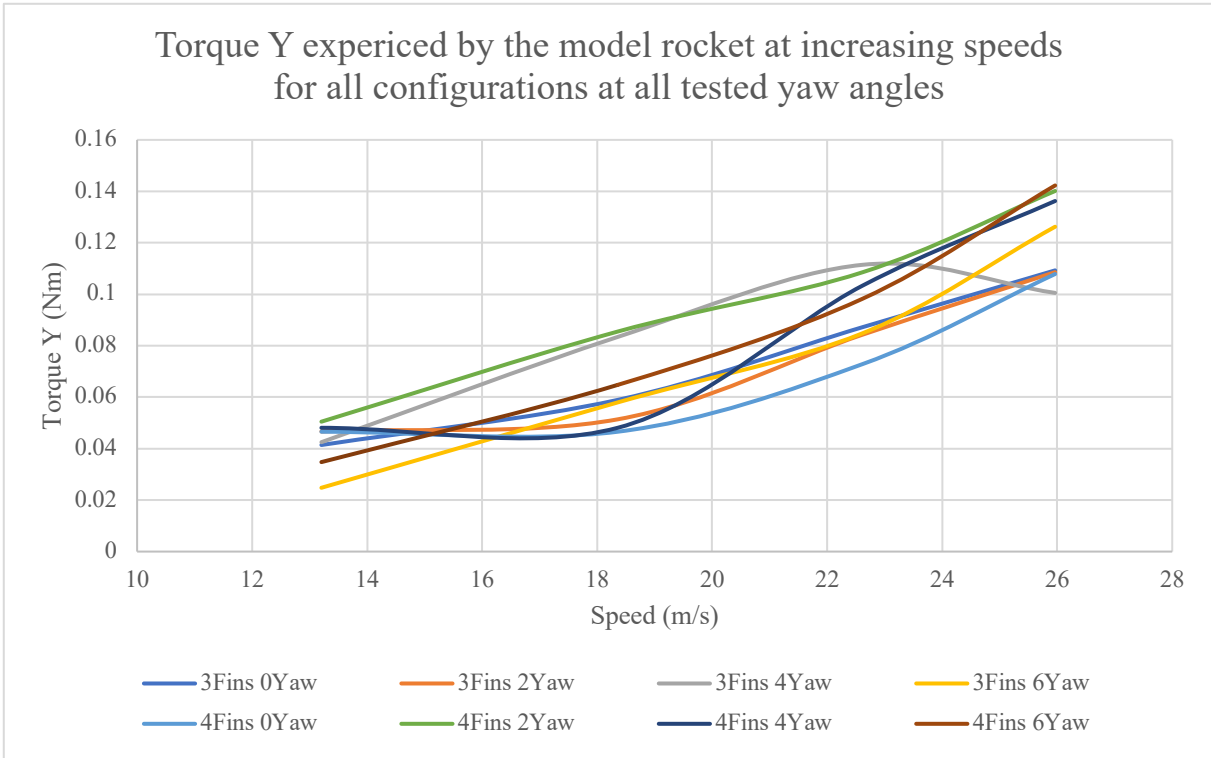


Figure 68 - Plotted data of the torque Y experienced by the rocket

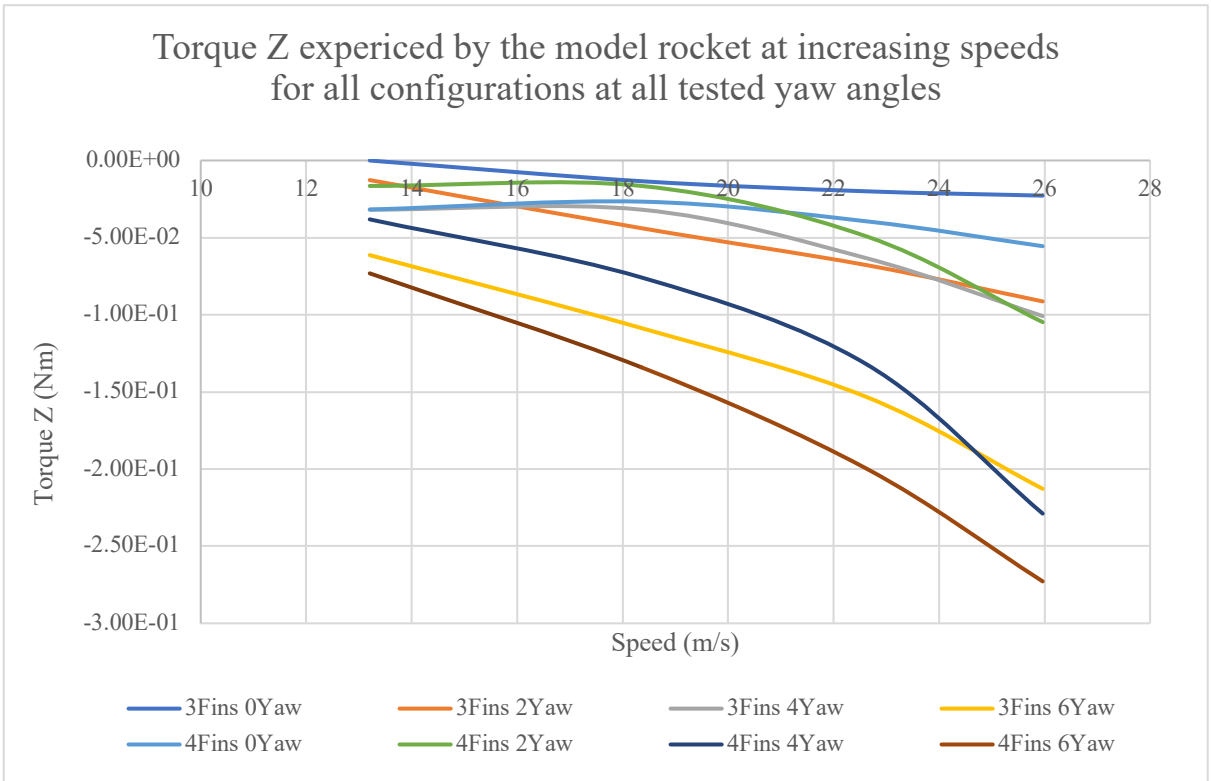
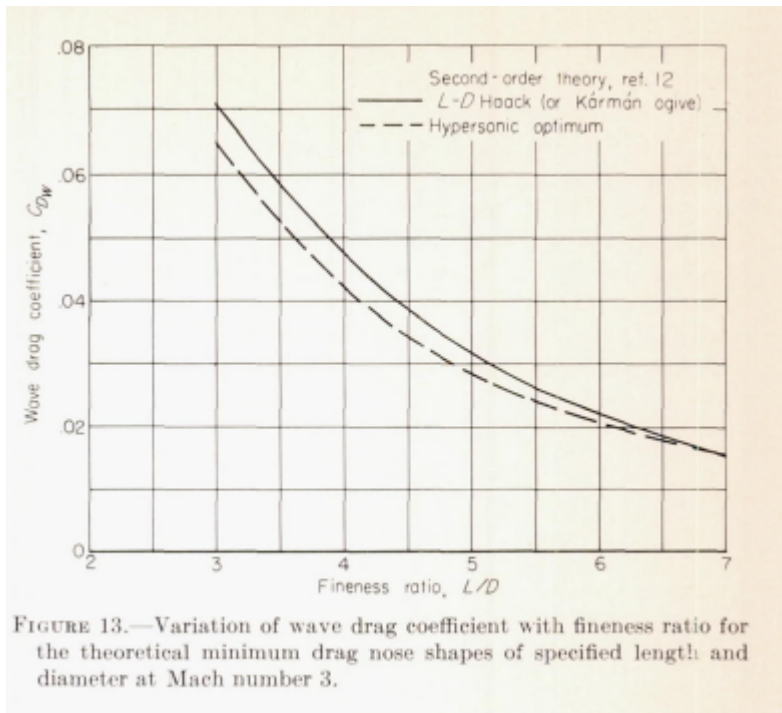


Figure 69 - Plotted data of the torque Z experienced by the rocket

## Appendix B



(Perkins, Jorgensen, & Sommer, 1958)

# Appendix C

TABLE II

Comparison of  $C_D$  values obtained using the modified ogive of curvature method, with those given by the method of characteristics and Van Dyke's second order theory.

Profile	Method (and Ref. No.)	F	M	$C_D$ By Given Method	$C_D$ By Modified Ogive of Curvature	% Error
Von Karman	Van Dyke (Ref. 7)	6	2.0	0.0226	0.0230	+ 2
Linear	Character- istics (Ref. 9)	4.17	2.0	0.0511	0.0500	- 2
		2.84	1.5	0.1062	0.105	- 1
Cubic	'	4.17	1.5	0.0494	0.0497	+ $\frac{1}{2}$
		4.17	2.0	0.0460	0.0470	+ 2

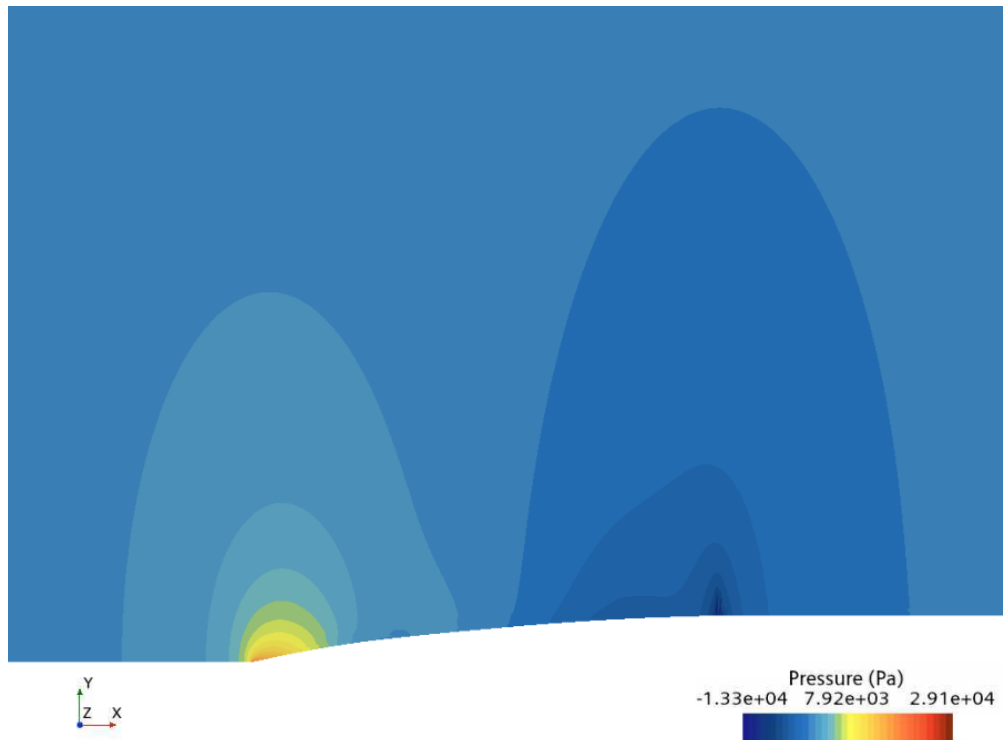
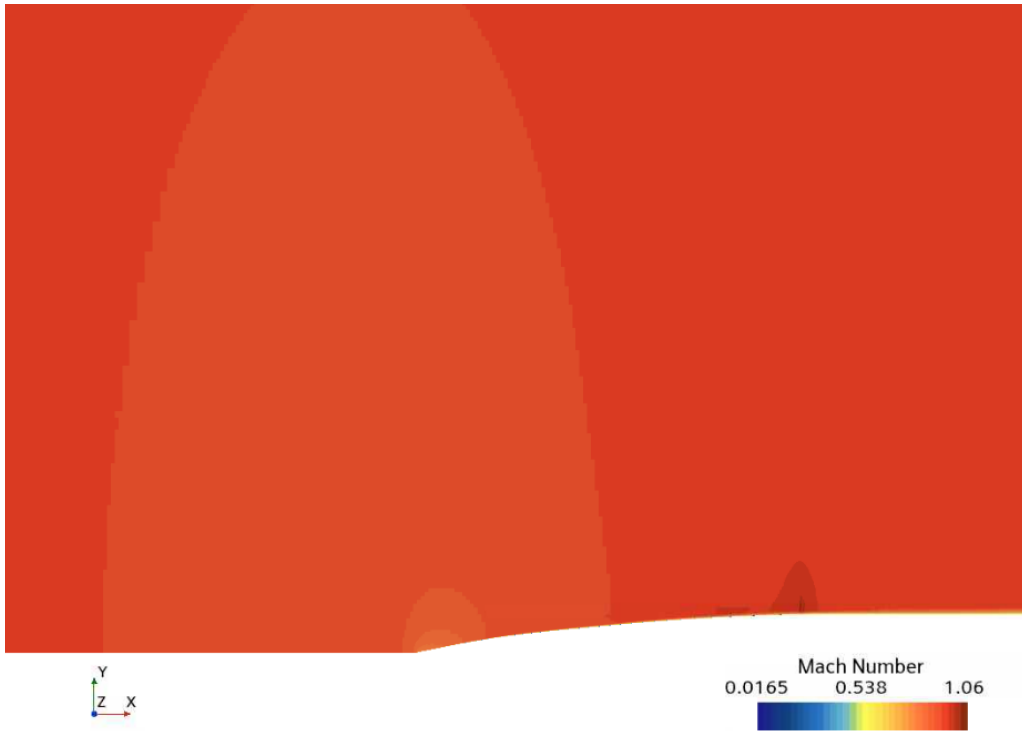
(Maarson, 1954)

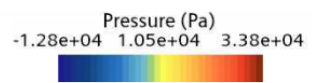
# Appendix D

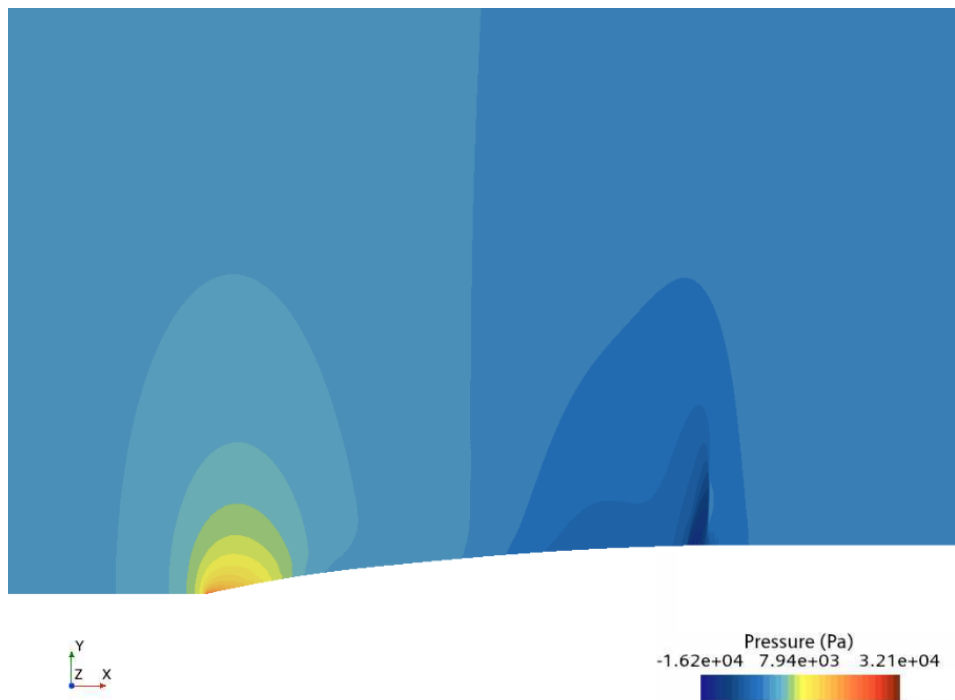
Pressure and Velocity contour plots for  $M = 0.8 - 1.4$

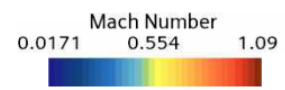




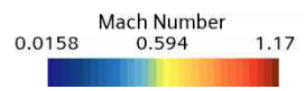


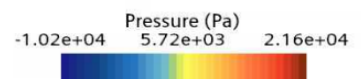
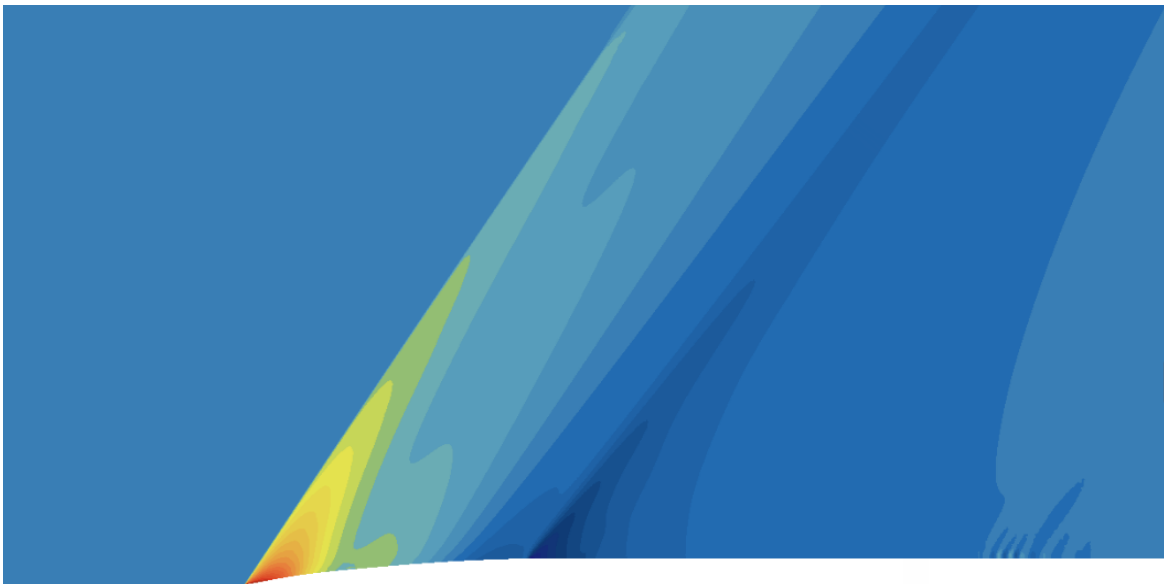


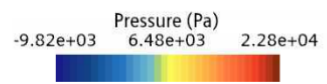












# Appendix E

Mach 0.2 Contours

